Pack Cementation Cr-Al Coating of Steels and Ge-Doped Silicide Coating of Cr-Nb Alloy

Y. R. He, M. H. Zheng and R. A. Rapp

Department of Materials Science and Engineering
The Ohio State University
2041 College Road
Columbus, OH 43210-1179

ABSTRACT

Carbon steels or low-alloy steels used in utility boilers, heat exchangers, petrochemical plants and coal gasification systems are subjected to high temperature corrosion attack such as oxidation, sulfidation and hot corrosion. The pack cementation coating process has proven to be an economical and effective method to enhance the corrosion resistance by modifying the surface composition of steels. With the aid of a computer program, STEPSOL, pack cementation conditions to produce a ferrite Cr-Al diffusion coating on carbon-containing steels by using elemental Cr and Al powders have been calculated and experimentally verified. The cyclic oxidation kinetics for the Cr-Al coated steels are presented.

Chromium silicide can maintain high oxidation resistance up to 1100°C by forming a SiO_2 protective scale. Previous studies at Ohio State University have shown that the cyclic oxidation resistance of $MoSi_2$ and $TiSi_2$ can be further improved by Ge addition introduced during coating growth. The halide-activated pack cementation process was modified to produce a Ge-doped silicide diffusion coating in a single processing step for the ORNL-developed Cr-Nb advanced intermetallic alloy. The oxidation behavior of the silicide-coated Cr-Nb alloy was excellent: weight gain of about $1 mg/cm^2$ upon oxidation at 1100°C in air for 100 hours.

INTRODUCTION

For economic reasons, carbon steels or low alloy steels are still the principal materials used in utility boilers, heat exchangers, petrochemical plants and coal gasification systems. The corrosion of these materials by oxidation, sulfidation or hot corrosion at elevated temperatures is a major problem encountered in these systems. One of the approaches to improve the corrosion resistance of steels is to modify the surface composition. Extensive studies have shown that ternary iron-base alloys containing 15-25 wt.% Cr, 4-6 wt.% Al exhibits excellent oxidation resistance at high temperatures due to the synergistic interaction of the two oxidation-resistant elements[1-4]. When exposed to an oxidizing environment at high temperature, a continuous adherent Cr_2O_3 scale is initially formed on the surface of the alloys. The rapid oxidation of Fe and the internal oxidation of Al are prevented by the formation of this scale. The Al atoms diffuse eventually to the Cr_2O_3/alloy interface and form a slowly growing, more stable, Al_2O_3 scale. Therefore, a surface composition of Fe - (15-25)wt.% Cr - (4-6)wt.% Al (Kanthal- like composition) is desirable to enhance the corrosion resistance of low-alloy steels.

Pack cementation has the advantages of low cost, good adhesion and wide versatility, as compared with other surface modification methods, such as metalliding, hot dipping, ion implantation, laser surface alloying[5]. There has been considerable work to develop a chromized-aluminized coating on steels by pack cementation[6-11]. Kanthal-like surface compositions have been achieved on low-carbon steels by using Cr-Al masteralloys. To reduce the material cost and optimize the pack cementation process, the current research is intended to develop a Kanthal-like Cr-Al coating on carbon-containing steels by using Cr and Al elemental powders in a pack cementation process.

Cr-silicide can maintain reasonable oxidation resistance up to 1100°C[12]. Another goal for this work was to develop a Ge-doped silicide coating on Cr-Nb alloys developed by Oak Ridge National Laboratory (ORNL). The purpose of the Ge addition is to improve the protective SiO_2 film that forms on the silicide coating during high-temperature oxidation. Previous studies by Mueller, et al. show that Ge-doped $(Mo,W)Si_2$ improves the isothermal and cyclic oxidation resistance by increasing the thermal expansion coefficient of the vitreous silica film, and prevents pesting by decreasing the viscosity of the protective film[13, 14]. Cockeram and Rapp have also successfully developed a Ge-doped Ti-silicide diffusion coating on commercially pure Ti, Ti-22Al-27Nb and Ti-20Al-22Nb alloys in a single coating process[15].

PACK CEMENTATION

Halide-activated pack cementation is a high temperature in-situ chemical vapor deposition process. A pack consists of four components: substrate(s) to be coated, metal(s) or masteralloy(s) containing the element(s) to be deposited, halide activator salt(s), and an inert filler. The activator salt reacts with the masteralloy(s) and generates volatile metal halides. Driven by the chemical potential gradients for the elemental components between the pack and the substrate, these halide vapors diffuse through the porous filler material to the substrate surface, where the deposition of the element(s) occurs by one or more reactions[16].

Codeposition of two or more elements in a single processing step by the pack cementation method requires comparable partial pressures of the halide vapors containing these elements. If the partial pressure of one element dominates, the deposition of the other elements will be suppressed.

EXPERIMENTAL PROCEDURES

Nominally pure elemental powders of Al (99.9%, K-109, Transmet Corp.), Cr (99.22%, 100-325 mesh, Shieldalloy Metallurgical Corp.), Si (99%, -325 mesh, Alfa), Ge (99.999%, Eagle Picher Industries) were used. The halide salt activators were NH_4Cl (99.8%, J. T. Baker Inc.), $MgCl_2$, NaF (99.7%, J. T. Baker Chem. Co.). Alumina (98%, 60-325 mesh, Fisher Sci.) was used as an inert filler. The alumina crucible containing the pack was sealed with an alumina lid using high-temperature Ceramabond. The sealed crucible was then cured in an electric oven (90°C) for more than 2 hours, then positioned in the uniform heating zone of a horizontal resistance-heated tube furnace. Prepurified Ar gas flowed through the furnace tube to protect the pack from oxidation. A K-type thermocouple was used to measure the temperature. After holding at the desired temperature for a given time, the crucible was allowed to furnace cool. The coupon retrieved from the pack was cleaned in an ultrasonic cleaner.

A Nikon EPIPHOT-TME optical microscope was used for metallographic examination. X-ray analysis was carried out on a SCINTAG diffractometer. A Phillips XL-30 scanning electron microscope (SEM) with an Energy Dispersive X-ray Spectrometer (EDS) was utilized to analyze the cross-sections of the samples.

RESULTS AND DISCUSSION

Cr-Al Coating on T11 Alloy

A pack containing 18 Cr - 2 Al -2 $MgCl_2$ - 1 NH_4Cl - 77 Al_2O_3 (wt.%) was used to codeposit Cr and Al on T11 steel. The pack cementation cycle consisted of heating to 950°C, holding for 4 hours, then raising the temperature to 1150°C and holding for 3 hours before furnace cooling to room temperature.

Figure 1 shows the cross-section of a T11 steel Cr-Al coated at 950°C for 4 hours. A ferrite coating layer was formed; $Cr_{23}C_6$ was not detected by X-ray diffraction analysis. At this low temperature (950°C), the ferrite-stabilizing Al was transported to the surface, such that the carbon in the steel was again rejected into the austenite core, before the $CrCl_2$ vapor reached a sufficient vapor pressure to form $Cr_{23}C_6$. Once the ferrite case has been initiated, the inward rejection of carbon in front of the growing ferrite permits the addition of Cr to the ferrite layer without carbide formation. Figure 2 (a) displays the cross-section of Cr-Al coated T11 after the complete processing cycle. Pearlite formed beneath the ferrite coating layer due to the rejection of C from the ferrite layer to the austenite core at the processing temperature. The composition profile of Fig. 2 (a) is shown in Fig. 2 (b). Obviously, this composition range is not that desired, and future experimentation will seek to achieve the Fe-20Cr-5Al composition. The avoidance of Cr carbide formation at the external surface confirmed the applicability of the sequential deposition mode[11], as illustrated in Fig. 3.

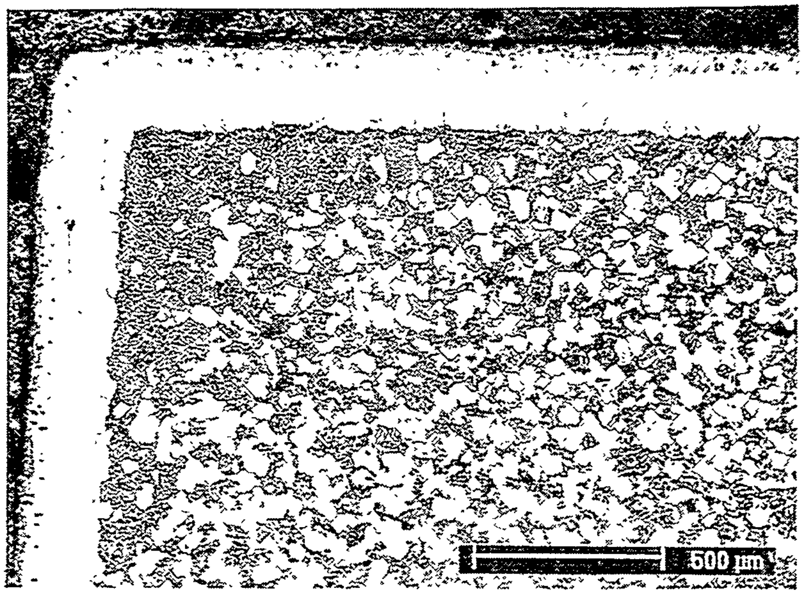

Fig. 1 Cross-section of T11 steel Cr-Al coated at 950°C for 4 hours

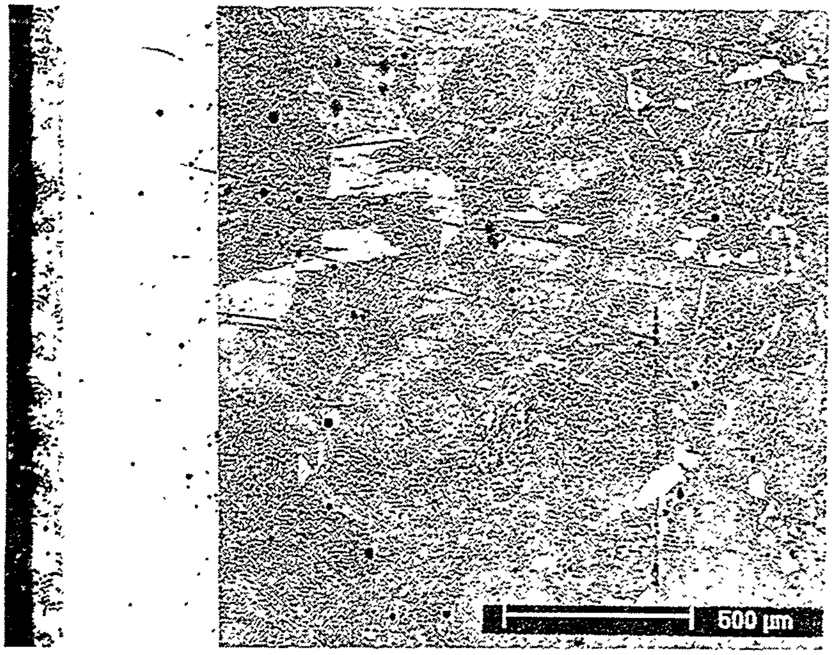

Fig. 2 (a) Cross-section of T11 steel Cr-Al coated at 950°C for 4 hour followed by another 3 hour holding at 1150°C

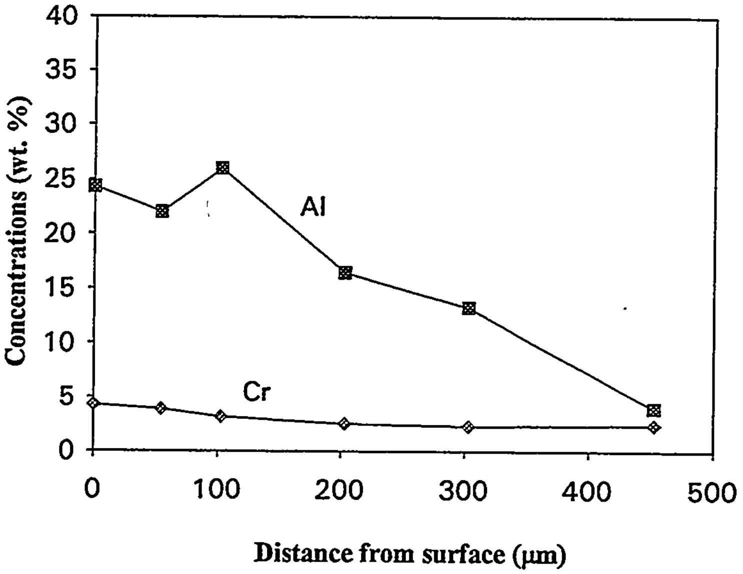

Fig. 2 (b) Composition profile of Cr-Al coated T11steel

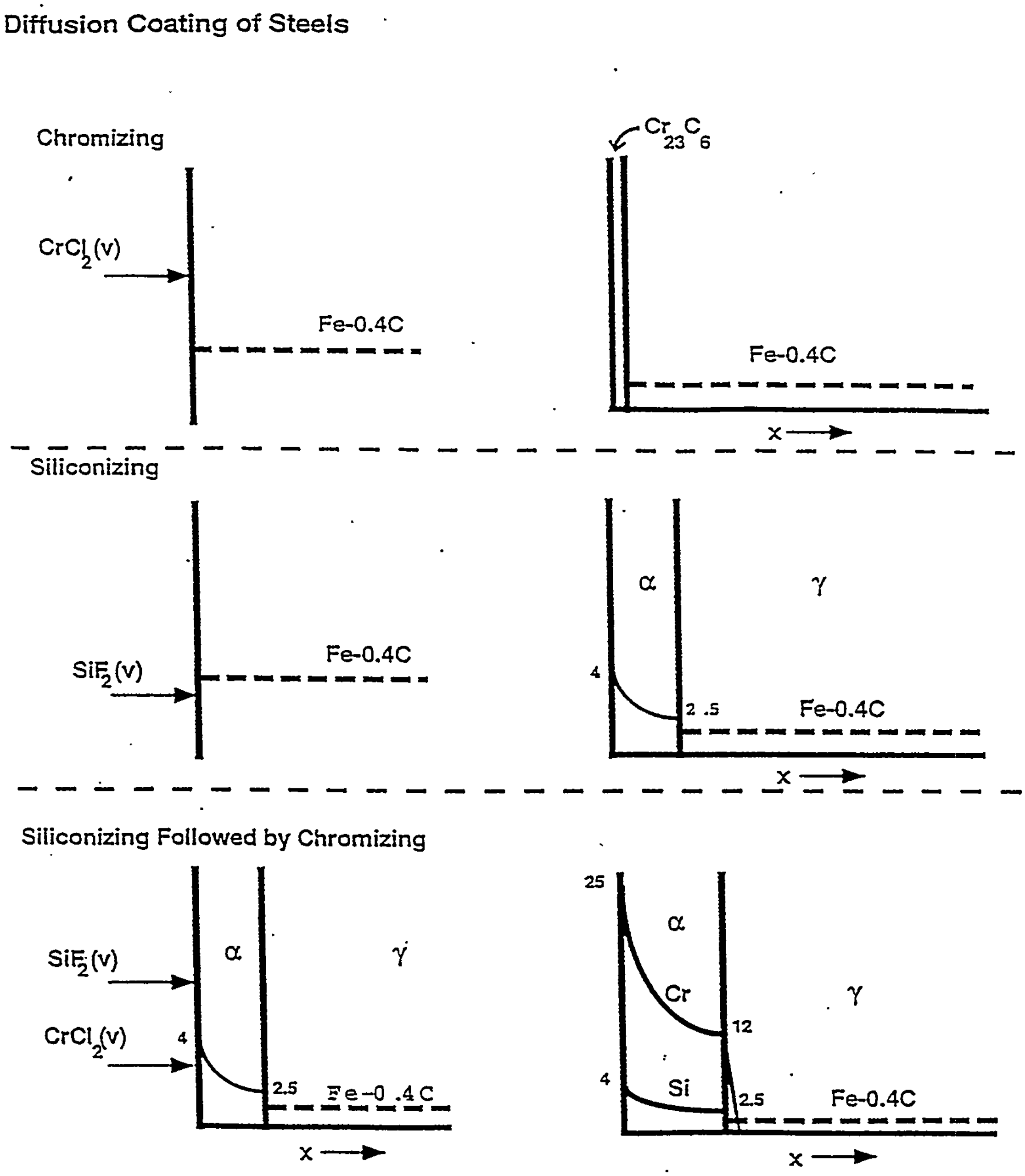

Fig. 3 Processing scheme illustrating mode for codeposition of Cr-Si or Cr-Al to form a ferrite case without a blocking Cr-carbide

Ge-Doped Silicide Coating on Cr-Nb Alloys

With the aid of a computer program, STEPSOL, the equilibrium vapor pressures in a NaF activated pack containing pure Si and pure Ge at 1000°C and 1 atm. total pressure were calculated and are listed in Table 1. Unit activity was used for Si and Ge in the calculation. During pack cementation, Si-Ge alloy is expected to form in the pack from the initial mixture of the pure elemental powders by melting of Ge (melting point 937°C). Therefore, the activities of both Si and Ge in the pack would be less than unity.

Table 1. The STEPSOL computed equilibrium vapor pressure in a NaF-activated pack containing pure Si -pure Ge and Al_2O_3 filler at 1000°C and 1 atm. total pressure

Species	Pressure (atm.)	Species	Pressure (atm.)
Ar	9.94×10^{-1}	GeF_2	1.86×10^{-6}
Na	3.95×10^{-3}	GeF	2.30×10^{-8}
SiF_4	9.17×10^{-4}	Ge	7.15×10^{-9}
NaF	3.66×10^{-4}	SiF	4.8×10^{-10}
SiF_3	7.98×10^{-5}	Si	1.69×10^{-11}
Na_2F_2	3.92×10^{-5}	GeF_3	2.76×10^{-18}
SiF_2	6.32×10^{-6}	GeF_4	8.77×10^{-21}

Four Cr-silicide compounds, Cr_3Si, Cr_5Si_3, CrSi and $CrSi_2$, exist in the Cr-Si system. Due to the lack of standard X-ray diffraction patterns for Cr_5Si_3 and CrSi, EDS data were used to identify the existing phases after pack cementation.

Figures 4 (a) and 4 (b) show the surface morphology and the cross-section of a CN-87 alloy coated at 1000°C for 12 hours in a pack containing 16Si-8Ge (wt.%), respectively. X-ray diffraction analysis on the coupon surface revealed the existence of Cr_3Si and $Cr(Si,Al)_2$. EDS data showed that the externally deposited phase in Fig. 4 (a) was composed of 57.0F, 34.9 Na and 8.1Al (at.%). Previous work found that a Na-Al-oxide byproduct layer formed on the surface of $MoSi_2$ coating resulted from the use of a NaF activator[17]. This Na-rich byproduct passivated the $MoSi_2$ coating by forming a faster growing Na-silicate scale and suppressing accelerated oxidation and pesting of $MoSi_2$ during low-temperature oxidation. Three phases were identified in the back-scattered electron (BSE) image in Fig. 4 (c), a high magnification image of the coating in Fig. 4 (b). EDS analysis shows that the gray phase is composed of 33.9Cr, 14.9Fe, 48.6Si plus 1.0Ge, suggesting the existence of (Cr,Fe)(Si,Ge); the bright phase has the composition 25.9Cr, 20.1 Nb, 5.9Mo, 5.7 Fe, 41.6Si with 0.86Ge; the dark phase consisted of 28.2Cr, 4.8Fe, 62.0Si plus 0.5 Ge, probably in a form of $(Cr,Fe)(Si,Ge)_2$.

A cross-section of CN-87 alloy coated in a pack containing 16Ge-8Si (wt.%) is displayed in Fig. 5. X-ray diffraction analysis detected the existence of Cr_3Si phase in the coating. The coating can be subdivided into three layers. The two phases in the outermost layer in Fig. 5 (b) are a dark phase containing 29.7Cr, 26.9Fe, 42.3Si plus 0.5Ge, and a heterogeneous gray phase containing 34.8Cr, 7.8Fe, 9.8Nb, 3.5Mo, 43.1Si with 0.9Ge. The second layer was mainly composed of a gray phase decorated with some bright and dark phases. EDS analysis indicated the highest Ge content in the gray phase with a composition of 45.6Cr, 12.6Fe, 33.7Si and 1.8Ge. The third layer was very irregular and composed of a dark phase (50.6Cr, 15.7Fe, 2.4Mo, 30.8 Si and 0.1 Ge) and partially transformed Cr_2Nb particles.

Figures 6 (a) and (b) present the surface and cross-section of the CN-87 alloy coated in a pack containing 20Ge-4Si (wt.%), respectively. The $Cr_3NbSi_{2.66}$ phase was identified using X-ray diffraction. The formation of nodules with 10.4Na, 18.8Al, 14.2Si, 48.4O and 8.1F on the surface of the coupon indicated again the existence of a liquid phase during pack cementation. EDS analysis suggested the formation of (Cr,Fe)(Si,Ge) in the outermost layer with the composition of 25.6Cr, 25.1Fe, 47.7Si plus 1.6Ge. The heterogeneous phase in the second layer was composed of 38.7Cr, 9.9Fe, 5.3Nb, 3.3Mo, 40.2Si and 2.7Ge. The major phase in the third layer adjacent to the substrate had the composition of 52.4Cr, 8.2Fe, 37.3Si plus 0.5Ge, which might indicate the presence of $(Cr,Fe)_5Si_3$.

The addition of Ge to Cr-silicide showed some effect on the coating morphology, and increasing the ratio of Ge to Si in the pack suppressed the formation of $CrSi_2$ on the CN-87 alloy, perhaps due to the decrease in Si-fluoride vapor pressures with decreasing ratio of Si to Ge. Higher levels of Ge tended to increase the Ge content in the coating and retard coating growth. Also, the Ge concentration is higher in the inner layer for each coating. A similar effect was also observed in the development of the $(Mo,W)(Si,Ge)_2$ coating[13] and the Ge-doped Ti-silicide coating[17].

Figure 7 shows the surface morphology of a CN-80 alloy coated in a NaF activated pack containing 16Si-8Ge. X-ray diffraction analysis detected the formation of $CrSi_2$. Oxidation tests were conducted at 950°C and 1100°C by P. Tortorelli at ORNL. As shown in Fig. 8, the Ge-doped Cr-disilicide coating prevented the CN-80 alloy from suffering significant oxidation at high temperatures. The weight gain was about $1 mg/cm^2$ upon oxidation at 1100°C in air for 100 hours.

CONCLUSIONS

Codeposition of Cr and Al in a pack cementation can be achieved using pure elemental powders, but the ideal surface composition has not been achieved. Cr-carbide formation has been prevented by first diffusing ferrite-stabilizing Al into the substrate at lower temperature.

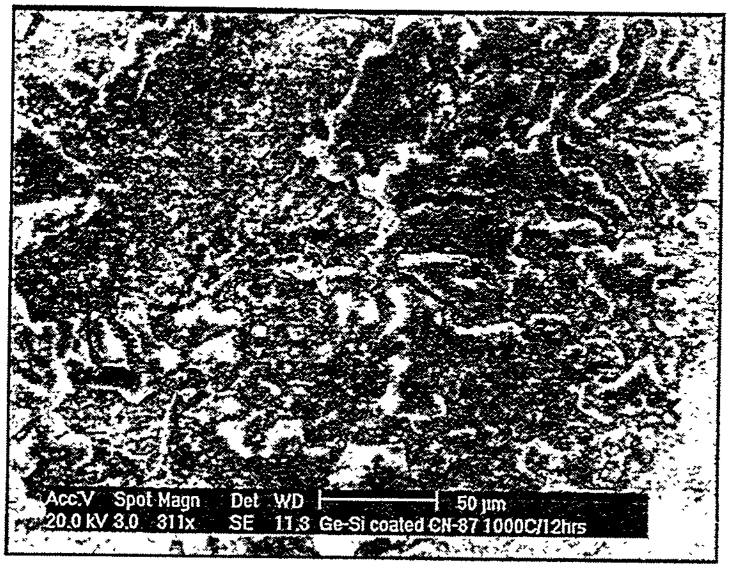

Fig. 4 (a) Surface morphology of CN-87 alloy coated at 1000°C for 12 hours in a NaF activated pack containing 16Si-8Ge.

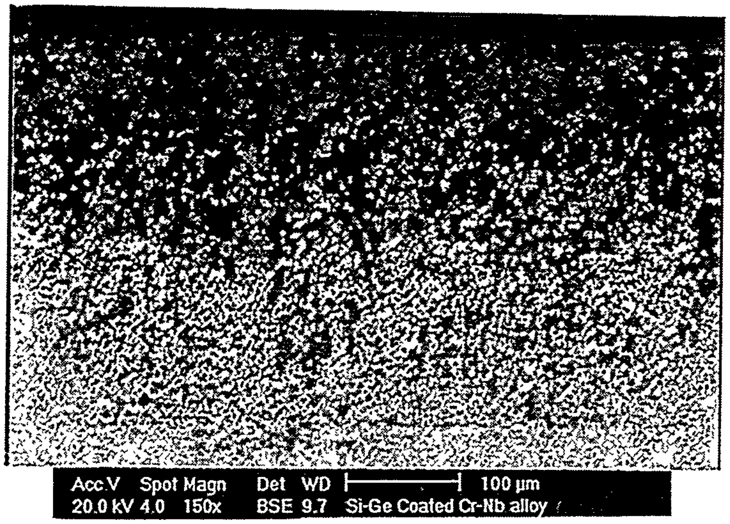

Fig. 4 (b) Cross-section of CN-87 alloy coated at 1000°C for 12 hours in a NaF activated pack containing 16Si-8Ge.

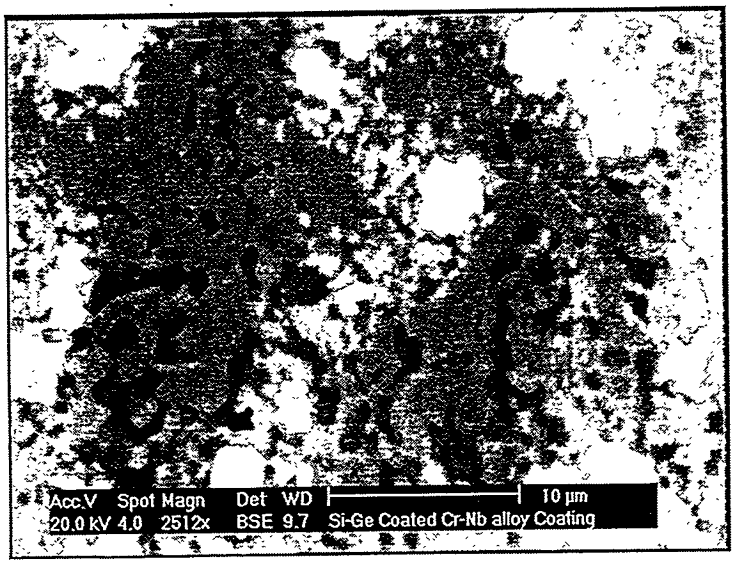

Fig. 4 (c) A high magnification image of the cross-section of Fig. 4 (b).

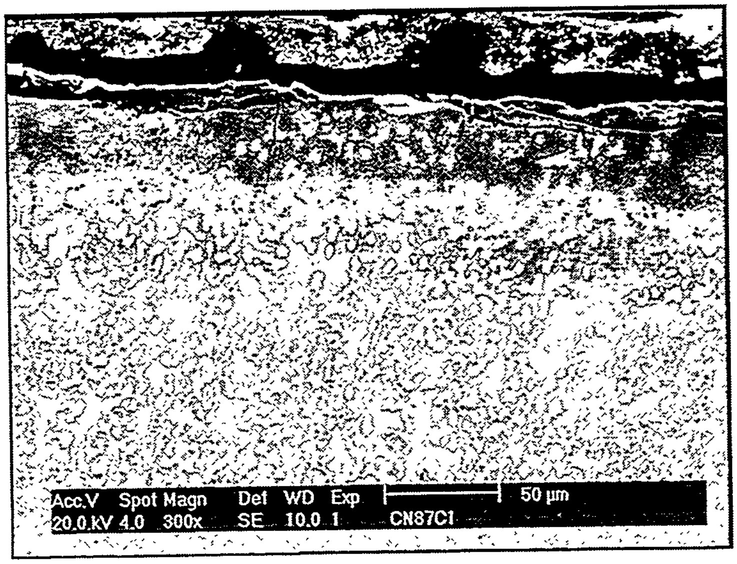

Fig.5 (a) Cross-section of CN-87 alloy coated at 1000°C for 12 hours in a NaF-activated pack containing 8Si-16Ge.

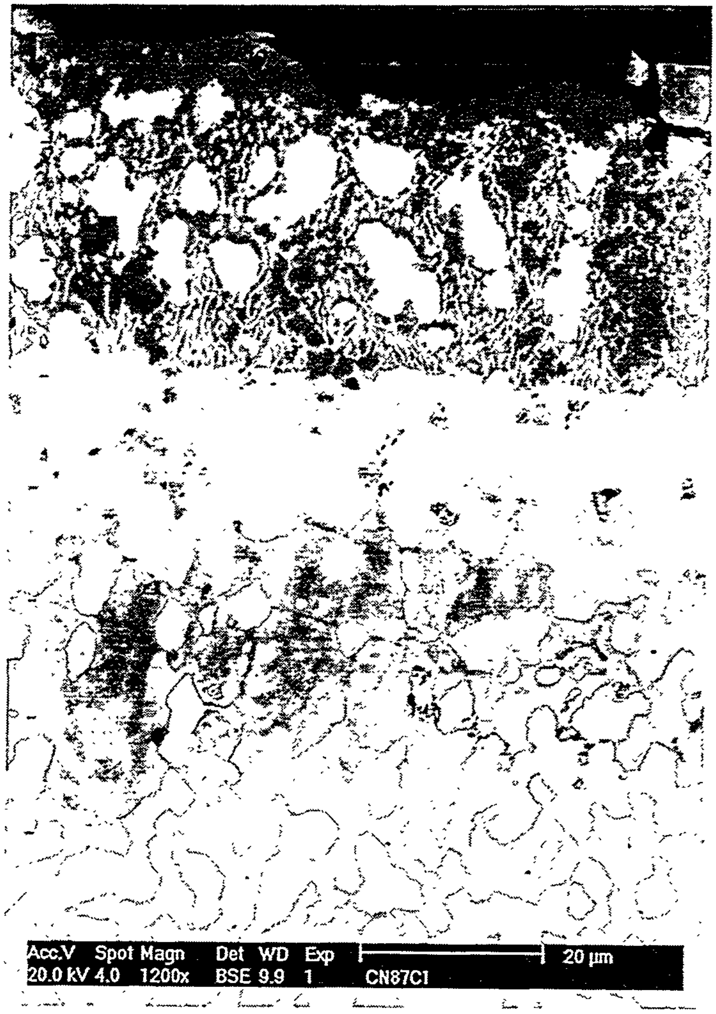

Fig. 5 (b) A high magnification image of Fig. 5 (a)

Ge-doped Cr-silicide diffusion coating was able to be developed on Cr-Nb alloys in a single pack cementation process. The morpology and composition of the coating depended not only on the composition of the pack, but also on the composition of the substrate alloy. Oxidation in air shows that the Ge-doped Cr-silicide coating prevented the Cr-Nb alloy from suffering significant oxidation.

REFERENCES

1. F. H. Stott, G. C. Wood and M. G. Hobby, "A Comparison of the Oxidation Behavior of Fe-Cr-Al, Ni-Cr-Al, and Co-Cr-Al Alloys", Oxid. Met., 3 (2), p. 103, 1971.
2. J. K. Tien and F. S. Pettit, "Mechanism of Oxide Adherence on Fe-25Cr-4Al (Y or Sc) Alloys", Met. Trans., 3 (6), p. 1587, 1972.
3. F. A. Golightly, F. H. Scott and G. C. Wood, "The Influence of Yttrium Addition on Oxide-scale Adhesion to an Iron-Chromium-Aluminum Alloy", Oxid. Met., 10 (3), p. 163, 1976.
4. V. K. Tolpygo and H. J. Grabke, "Microstructural Characterization and Adherence of α-Al_2O_3 Oxide Scales on Fe-Cr-Al and Fe-Cr-Al-Y Alloys", Oxid. Met., 41 (516), p. 343, 1994.
5. P. G. Cappelli, " Coating Processes", High Temperature Alloys for Gas Turbines, D. Coutsouradis, P. Felix, H. Fischmeister, L. Habraken, Y. Lindblom and M. O. Speidel (Eds), Applied Science Publishers, London, p. 177, 1978.
6. D. M. Miller, S. C. Kung, S. D. Scarberry and R. A. Rapp, "Simultaneous Chromizing-Aluminizing Coating of Austenitic Stainless Steels", Oxid. Met., 29, p. 239, 1988.
7. P. A. Choquet, E. R. Naylor and R. A. Rapp, "Simultaneous Chromizing and Aluminizing of Iron-base Alloys", Materials Science and Engineering, A 121, p. 413, 1989.
8. S. C. Kung and R. A. Rapp, "Analyses of the Gaseous Species in Halide-Activated Cementation Coating Packs", Oxid. Met., 32, p. 89, 1989.
9. R. Bianco, M. A. Harper and R. A. Rapp, "Codepositing Elements by Halide-Activated Pack Cementation", JOM, Nov., p. 68, 1991.
10. F. D. Geib and R. A. Rapp, "Simultaneous Chromizing-Aluminizing Coating of Low-Alloy Steels by a Halide-Activated, Pack-Cementation Process", Oxid. Met., p. 213, 1993.
11. N. He, G. Wang and R. A. Rapp, "The Common Component Effect in Multiphase, Multicomponent Equilibria ", High Temperature Science, submitted for publication, 1994.
12. G. H. Meier, "Fundamentals of the Oxidation of High-Temperature Intermetallics", Oxidation of High-Temperature Intermetallics, T. Grobstein and J. Doychak (Eds), TMS Publishers, Pennsylvania., p. 1, 1988.
13. A. Mueller, G. Wang and R. A. Rapp, "Deposition and Cyclic Oxidation Behavior of a Protective $(Mo, W)(Si,Ge)_2$ Coating on Nb-Base Alloys", J. Electrochem. Soc., 139(5), p. 1266, 1992.
14. A. Mueller, G. Wang and R. A. Rapp, "Oxidation Behavior of tungsten and Germanium--Alloyed Molybdenum Disilicide Coatings", Materials Science and Engineering, A155, p. 199, 1992.
15. B. V. Cockeram and R. A. Rapp, "Development and Growth of Boron-Modified and Germanium-Doped Titanium-Silicide Diffusion Coatings by the Halide-Activated Pack Cementation Method", Oxid. Met., submitted for publication, 1995
16. L. L. Seigle, "Thermodynamics and Kinetics of Pack Cementation Processes", Surface Engineering, R. Kossowsky and S. C. Singhal (Eds), Martinus Nijhoff Publishers, Boston, p. 345, 1984.
17. B. V. Cockeram, G. Wang and R. A. Rapp, "Preventing the Accelerated Low-Temperature Oxidation of $MoSi_2$ (Pesting) by the Application of Superficial Alkali Salt Layers", Oxid. Met., accepted for publication, 1995

MICROSTRUCTURE CHARACTERIZATION AND WELDABILITY EVALUATION OF THE WELD HEAT AFFECTED ZONE (HAZ) IN 310HCbN TUBING

C.D. Lundin and C.Y.P. Qiao

Materials Joining Research
Materials Science and Engineering
The University of Tennessee, Knoxville

ABSTRACT

Metallographic evaluation on the Gleeble simulated HAZ samples of 310HCbN tubing material was performed in order to reveal potential degradation in mechanical properties and corrosion resistance. The carbide evolutionary process in the HAZ samples was studied. It is indicated that 310HCbN material showed a weld HAZ sensitization tendency that is associated with the formation of $Cr_{23}C_6$.

INTRODUCTION

310HCbN tubing has been accepted for boiler applications under Code Case 2115. It has been employed by utilities in the United States for replacement of conventional stainless steels. Excellent high temperature mechanical properties, such as creep and high temperature tensile strength, have been reported [1]. However, need for the detailed information on aged base metal and weld HAZ microstructures and their relationship to material properties is apparent. In addition, weldability and welded fabrication associated property variations should be studied for optimum use of the material.

Weldability and microstructural evaluations of 310HCbN were conducted at Oak Ridge National Laboratory and the University of Tennessee [2-4]. The weldability assessment was conducted using the Varestraint hot cracking test and a newly developed tubing weld cracking (TWC) test. It is concluded that 310HCbN possesses an excellent hot cracking resistance. In addition, the TWC test is proven to be a viable tubing material weld hot cracking evaluation method.

The weld HAZ microstructural evaluation was conducted using Gleeble simulated HAZ samples and electric resistance spot welded samples. The metallographic evaluation was performed using OLM, SEM and STEM. The microstructural changes and secondary phase evolution processes as a function of the weld HAZ peak temperature were investigated. The results from this study were used to explain the HAZ hot cracking mechanism as well as the weld HAZ stress corrosion cracking sensitivity (ASTM 262 Practice A).

EXPERIMENTAL PROCEDURES

The material used in this study is a commercial heat of 310HCbN tubing. The composition of the 310HCbN heat is presented in Table 1. The 310HCbN tubing was in the annealed condition.

Table 1. Composition of the 310HCbN tubing.

C	Mn	P	S	Si	Ni	Cr	Mo	V	Nb
0.061	1.19	0.010	<0.001	0.36	19.92	24.06	0.07	0.04	0.45
Ti	Co	Cu	Al	B	W	Fe	N	O	Ta
<0.01	0.27	0.09	0.023	0.002	<0.01	53.3	0.26	0.005	<0.01

* The chemical composition was analyzed at ABB Combustion Engineering.

The microstructural evaluation was carried out on the base metal and Gleeble simulated HAZ samples. For the Gleeble simulated HAZ samples, seven different peak temperatures (900°C, 1000°C, 1100°C, 1200°C, 1250°C, 1300°C and 1320°C) were selected. Optical light, scanning electron and transmission electron microscopy was employed for the metallographic examinations. The ASTM 262 Practice A was conducted on the Gleeble simulated HAZ samples. Limited precipitate particle characterization was performed using EDS and x-ray diffraction techniques.

RESULTS AND DISCUSSIONS

The previous investigations [3] at the University of Tennessee revealed that 310HCbN tubing possesses an excellent weld hot cracking resistance (using both Varestraint and TWC tests). Thus, the emphasis in this tubing evaluation of 310HCbN was concentrated on the HAZ microstructural evolution and aging. One of the major microstructural concerns is the carbide evolution behavior and its relationship to the mechanical properties and metallurgical and corrosion behavior.

Optical Microstructural Evaluation

Figure 1 shows the optical microstructural morphology of base metal and the simulated HAZ samples (etched with aqua regia). Clearly, the carbides and nitrides are uniformly distributed

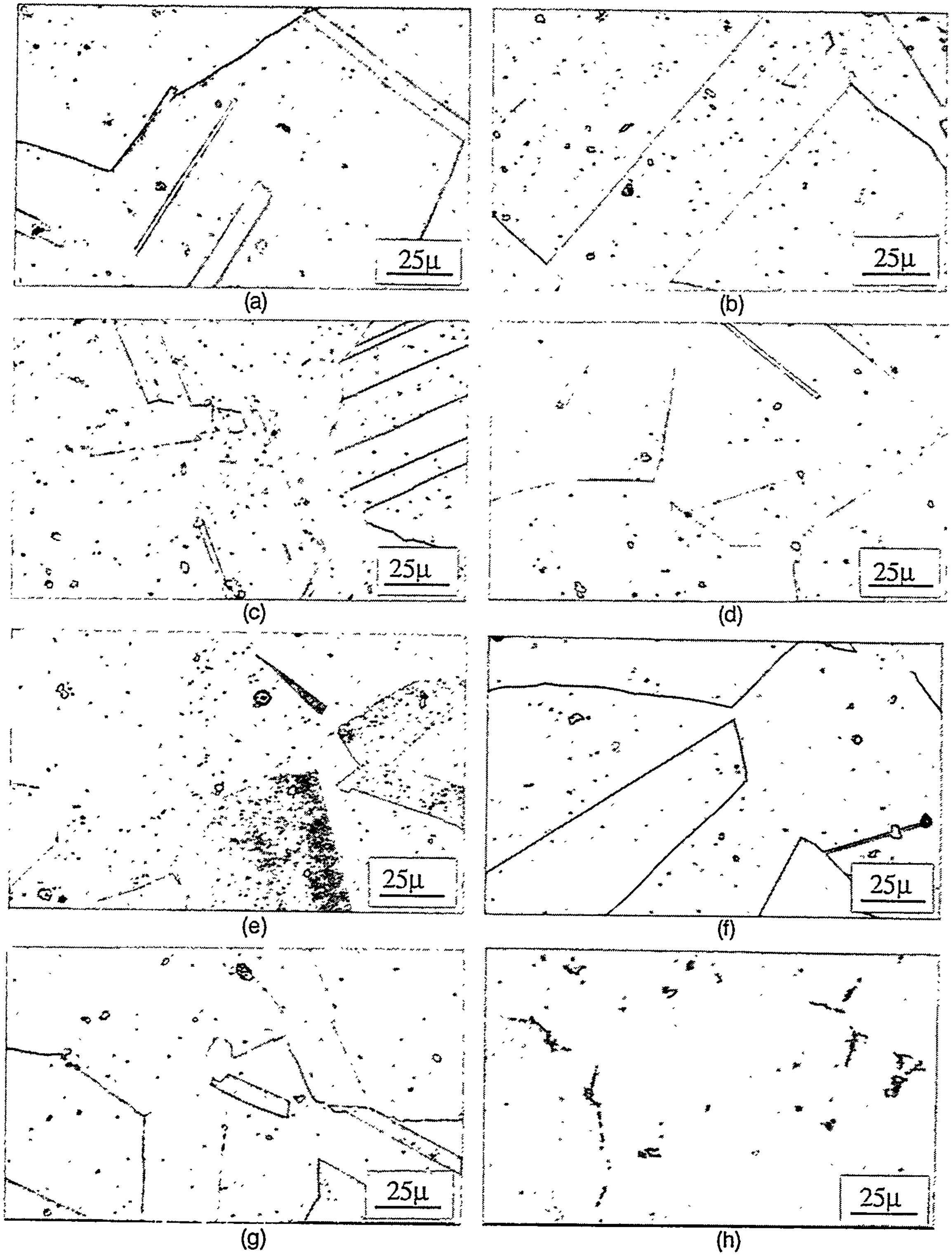

Figure 1. Optical microstructural morphology of base metal and the simulated HAZ samples. (a) Base Metal, (b) HAZ (PT: 900°C), (c) HAZ (PT: 1000°C), (d) HAZ (PT: 1100°C), (e) HAZ (PT: 1200°C), (f) HAZ (PT: 1250°C), (g) HAZ (PT: 1300°C), and (h) HAZ (1320°C).

in the base material matrix in the annealed condition. In the samples with the simulated peak temperatures of 900°C and 1000°C, a greater amount of precipitate was observed compared to the base metal, especially for the small size particles. The precipitate is slightly reduced in the sample with a simulated peak temperature of 1100°C compared to base metal. This may reflect the initiation of precipitate dissolution for certain precipitate particles (e.g. $M_{23}C_6$). In addition, fine precipitates were observed and it is believed that MC type carbides start to form under this HAZ thermal expose. When the simulated peak temperature is in excess of to 1200°C, the fine precipitates increase and it is expected that the newly formed precipitates are dominantly NbC and/or NbN carbides. A similar microstructural morphology was found in sample with the simulated peak temperatures of 1250°C and 1300°C. Additionally, evidence of a reaction between carbides and matrix was observable although it appears that the reaction is in the initial stages. In the simulated HAZ sample with a peak temperature of 1320°C (ZDT), significant evidence of a liquation reaction is apparent. It is noticed that the liquated areas are distributed both intergranularly and intragranularly.

HAZ Sensitization Evaluation

Figure 2 presents the microstructural morphologies of the Gleeble simulated HAZ samples after electrolytic etching with oxalic solution (ASTM A262 Practice A). It is evident that the base metal is not sensitized. It is also shows that the precipitates are uniformly distributed in the base material. In the simulated HAZ samples with the peak temperatures of 900°C and 1000°C, a ditched type grain boundary morphology is present with grains completely surrounded. This is an indication of sensitization. This temperature range (900°C-1000°C) reflects the lower boundary of the HAZ. Therefore, intergranular type localized corrosion may take place in the as welded HAZ if aqueous conditions prevail. The cause of the sensitization is the formation of $Cr_{23}C_6$ type carbides along the grain boundaries and a Cr depleted zone adjacent to the grain boundaries.

It should be noticed that for the HAZ sample with the peak temperature of 1100°C, the grain boundaries were not ditched. Further, the amount of precipitates shown in the sample with the peak temperature 1100°C is significantly reduced compared to that in the simulated HAZ with peak temperatures of 900°C and 1000°C. This observation indicates that dissolution of $Cr_{23}C_6$ occurred for the 1100°C thermal history. Evidence of grain boundary ditching begins to be seen in the sample with a peak temperature of 1200°C and more evidence of grain boundaries is found in the sample with a peak temperature of 1250°C. However, this is step structure in the simulated

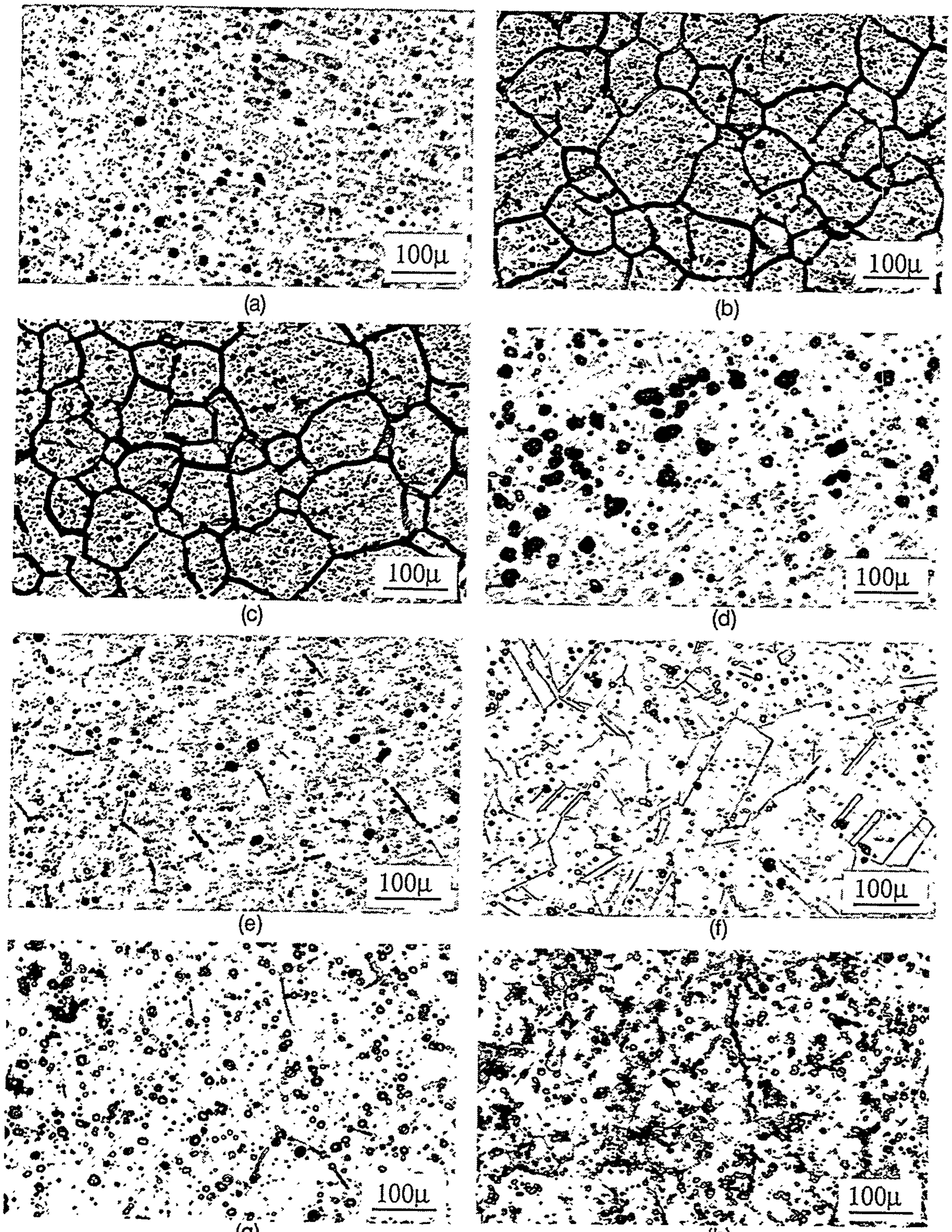

(a) (b) (c) (d) (e) (f) (g) (h)

Figure 2. Microstructures in the base metal and the simulated HAZs after A262 Practice A test. (a) Base Metal, (b) HAZ (PT: 900°C), (c) HAZ (PT: 1000°C), (d) HAZ (PT: 1100°C), (e) HAZ (PT: 1200°C), (f) HAZ (PT: 1250°C), (g) HAZ (PT: 1300°C), and (h) HAZ (1320°C).

HAZ sample with a peak temperature of 1250°C. A dual structure is evident in the simulated HAZ sample with a peak temperature of 1300°C and this becomes aggravated when the peak temperature is increased to 1320°C (ZDT). The explanation of the higher temperature range sensitization is due to the dissolution of MC and/or MN type precipitates and followed by relatively fast cooling. In this case, reformation of MC and/or MN type precipitates upon cooling is limited and during cooling in the lower temperature portion of welding thermal cycle, $Cr_{23}C_6$ is formed. This discussion indicates that "knife line" type attack may occur in the weld HAZ of as-welded 310HCbN.

TEM Microstructural Evaluation

In order to confirm the above observations and postulation, carbides and/or nitrides particles were extracted from the base material and EDS checked. Figure 3 shows the SEM morphology of particles extracted from the 310HCbN base material. The dominant particles are within the size range of 1μ to 10μ. The EDS examination results revealed that most of the particles are Nb rich carbides or nitrides. A small amount of Ti and Cr may be contained in the NbC and NbN. A typical EDS spectrum for particle "a" in Figure 3 is exhibited in Figure 4.

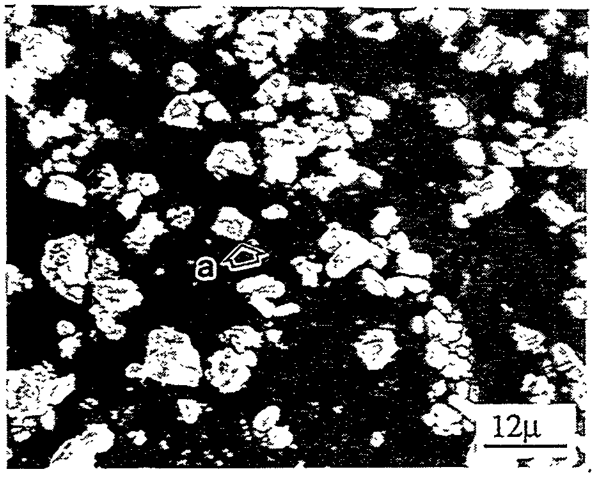

Figure 3. SEM morphologies of carbides extracted from base metal.

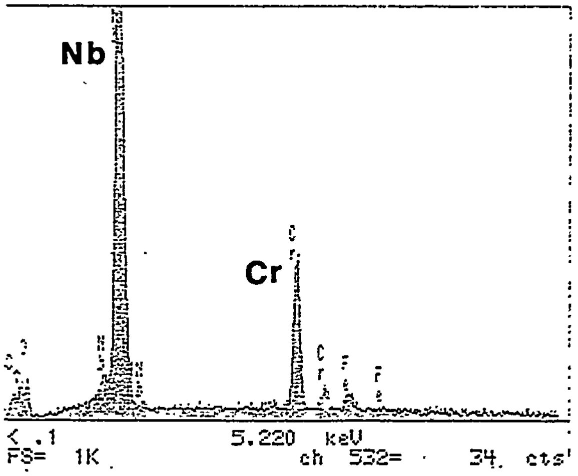

Figure 4. EDS spectrum for particle "a" in Figure 3.

Figure 5 shows the typical TEM microstructural morphologies of the base metal in which intragranular carbides are predominantly present. The dislocation density in the matrix of base material is low.

Typical TEM microstructural morphologies in the simulated HAZ samples with the peak temperatures of 900°C and 1000°C are presented in Figures 6 and 7, respectively. Evidence of an increased amount of precipitates and the appearance of intergranular precipitates are clearly indicated. The increase in carbides is due to the formation of $Cr_{23}C_6$ (preferentially along the grain boundaries). A typical EDS spectrum for these carbides is exhibited in Figure 8.

Typical TEM microstructural morphology of the simulated HAZ samples with a peak temperature of 1100°C is shown in Figure 9. Amount of precipitates (both intergranular and intragranular) in this sample is apparently reduced. Fine particles that are rich in Cr and Nb were present. A typical EDS spectrum of these particles is exhibited in Figure 10.

When the peak temperature increases to 1200°C, Nb rich type carbides become predominant and the size of Nb rich carbides increased compared to those observed in Figure 9 (1100°C) (see Figure 11). Figure 12 shows a typical TEM microstructural morphology in a sample with a peak temperature of 1250°C. More fine, rectangular, bar shaped carbides were formed at this temperature. A typical TEM microstructural morphology of the simulated HAZ sample with a peak temperature of 1300°C is shown in Figure 13. Clearly, the intergranular precipitates are dominant. A typical EDS spectrum of the particles in Figure 12 is shown in Figure 14. It is noticed that Nb content in carbides is increased in the simulated HAZ sample with a peak temperature of 1300°C compared to that in the simulated HAZ sample with a peak temperature of 1100°C. A typical TEM microstructural morphology of the simulated HAZ sample with a peak temperature of 1320°C is shown in Figure 15. The quantity of precipitate is further increased in this sample both intergranularly and intragranularly compared to that in the simulated HAZ sample with a peak temperature of 1300°C.

The HAZ hardness as a function of HAZ peak temperature in 310HCbN material is presented in Figure 16. In general, the variation of hardness in the HAZ is relatively small. Compared to base metal (190 HV), the entire HAZ region showed a lower hardness. As indicated in Figure 16, the maximum hardness was reached with a peak temperature of 1100°C, in which the fine Nb rich particles started to form according to the above metallographic evaluation results. It should be noted that hardness in weld HAZ is not only affected by the precipitate distribution but also associated by grain size, thus, the combined information should be considered in order to interpret the HAZ hardness behavior. Nevertheless, the microhardness measurements agree with the metallographic examination results.

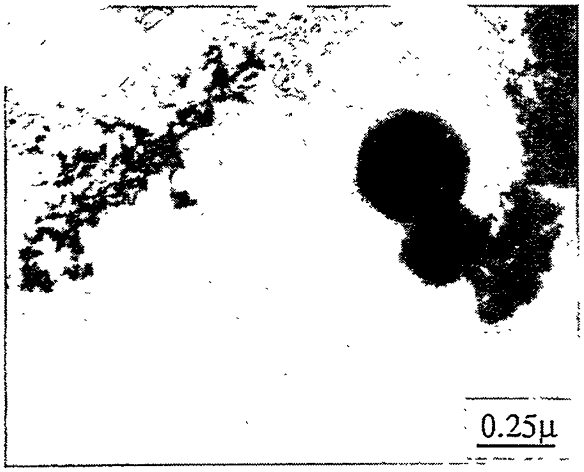

Figure 5. TEM microstructure of base metal.

Figure 6. TEM microstructure in the simulated HAZ with a peak temperature of 900°C.

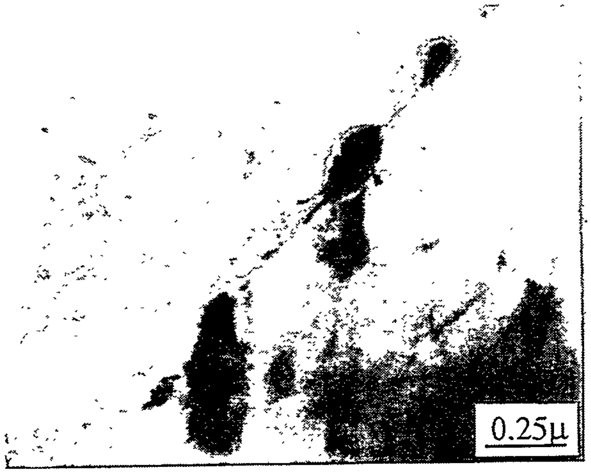

Figure 7. TEM microstructure in the simulated HAZ with a peak temperature of 1000°C.

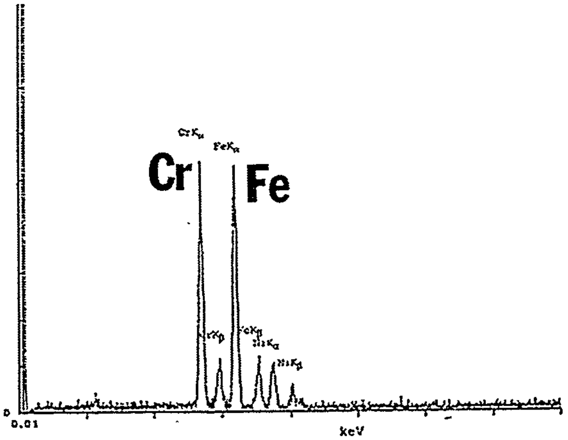

Figure 8. Typical EDS spectrum for the carbides in Figures 6 and 7.

Figure 9. TEM microstructure in the simulated HAZ with a peak temperature of 1100°C.

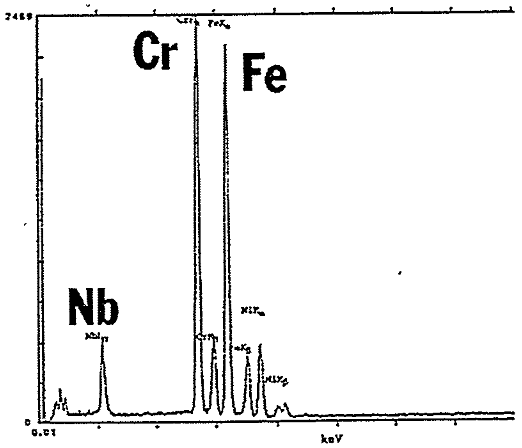

Figure 10. Typical EDS spectrum of the particles in Figure 9.

Figure 11. TEM microstructure in the simulated HAZ with a peak temperature of 1200°C.

Figure 12. TEM microstructure in the simulated HAZ with a peak temperature of 1250°C.

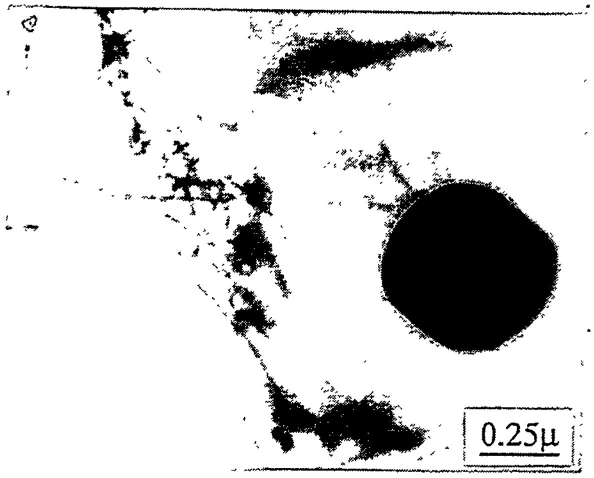

Figure 13. TEM microstructure in the simulated HAZ with a peak temperature of 1300°C.

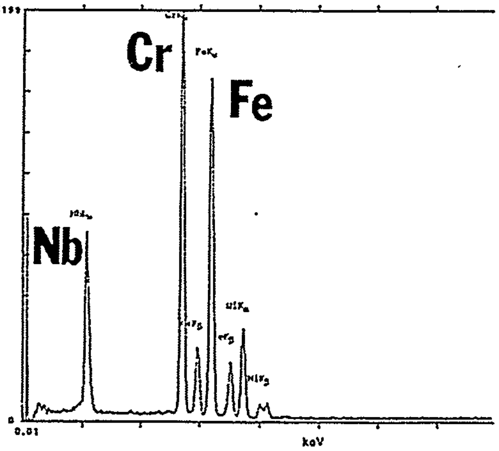

Figure 14. Typical EDS spectrum of the particles in Figure 13.

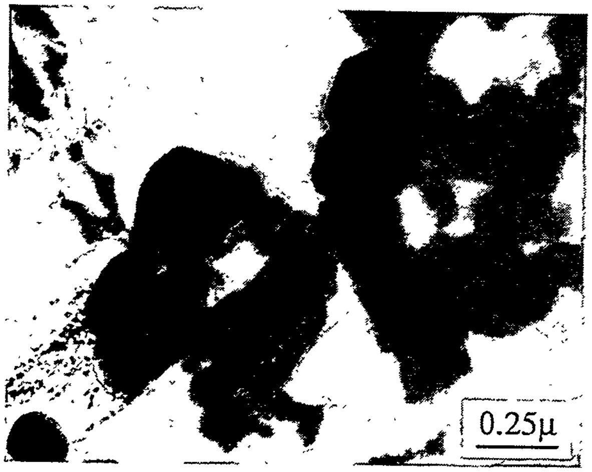

Figure 15. TEM microstructure in the simulated HAZ with a peak temperature of 1320°C.

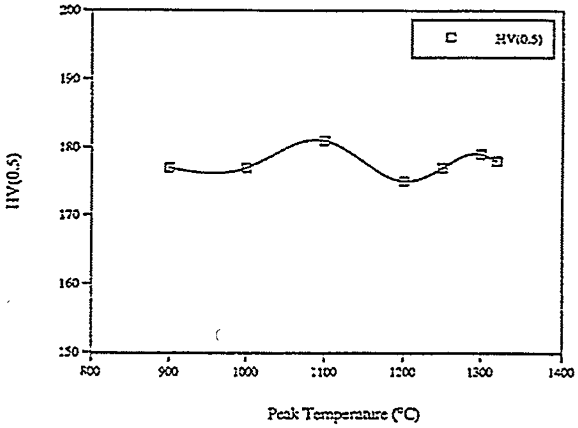

Figure 16. HAZ microhardness in the simulated HAZs.

SUMMARY

1. Metallographic examination indicated that carbide evaluation in the weld HAZ is the major factor causing the mechanical property and corrosion resistance changes in 310HCbN material.
2. A sensitized HAZ microstructure was found in the simulated HAZ samples of 310HCbN with peak temperatures of 900°C and 1000°C. The formation of $M_{23}C_6$ type carbides along the grain boundaries is directly responsible for this sensitization.
3. A dual type structure was observed in the simulated HAZ sample with peak temperature of 1320°C in A262 Practice A. This may imply that a "knife line" attack tendency may be present for 310HCbN.
4. This investigation also showed that carbides (both Nb rich MC type or Cr rich $M_{23}C_6$) evolution processes can occur in the weld HAZ of 310HCbN. The formation of MC type precipitates in the weld HAZ may enhance the reheat cracking tendency because fine MC type carbides preferentially form intragranularly at the dislocation and/or stack faulting sites.

ACKNOWLEDGMENTS

This study was financially supported by the U.S. Department of Energy, through Fossil Energy Materials Program operated at Oak Ridge National Laboratory. Advice from program/technical managers of ORNL, N.C. Cole, R.R. Judkins, R.W. Swindeman, and P.T, Carlson during the study is greatly appreciated.

REFERENCES

1. Sumitomo Metal Industries, Ltd Report, "Characteristics of a New Steel Tube (HR3C) with High Elevated Temperature Strength and High Corrosion Resistance for Boiler," December 1987.

2. R.W. Swindeman, Private Conversation, March 1995.

3. C.D. Lundin and C.Y.P. Qiao, "Investigation on the Weldability of High Temperature Alloy Tubing Materials," pp. 365-375, Proceedings of the Eighth Annual Conference on Fossil Energy Materials," CONF-9405143, ORNL/FMP-94-1, 1994.

4. C.D. Lundin and C.Y.P. Qiao, "Preliminary Metallographic Examination of Service Exposed SA 213 (Grade HR3C) Hot Reheat Tubing at TVA Gallatin Unit 2," Technical Report, The University of Tennessee, March 1995.

THE EFFECTS OF MICROSTRUCTURAL CONTROL ON THE MECHANICAL BEHAVIOR OF Cr_2Nb-BASED ALLOYS

J.A. Cook[1], P.K. Liaw[1], and C.T. Liu[2]

1. Department of Materials Science and Engineering
434 Dougherty Eng. Bldg.
University of Tennessee
Knoxville, TN 37996-2200

2. Oak Ridge National Laboratory
Metals and Ceramics Division
P.O. Box 2008
Oak Ridge, TN 37831-6115

ABSTRACT

Microstructural evaluations and mechanical testing of Laves-phase alloys based on Cr_2Nb were examined in order to optimize microstructural and mechanical properties by thermomechanical treatment at temperatures up to 1600°C. At ambient temperatures, single-phase Cr_2Nb alloys are very hard and brittle due to the complicated crystal structure (C-15). The following results were revealed through examination of the Cr-Cr_2Nb two-phase region: (a) with increasing amounts of the soft chromium-rich phase, the compression strength and hardness decrease; (b) the annealing treatments studied thus far provided the best break-up of the coarse/brittle Laves-containing eutectic phase in the 94 at.% Cr - 6 at.% Nb (CN-7) alloy; (c) two different anneals, 1 hour at 1600°C + 4 hours at 1200°C and 4 hours at 1550°C + 2 days at 1200°C, lead to a substantial improvement in the room temperature strength and compressive ductility over previous annealing treatments. Hot Isostatic Pressing has led to only a marginal reduction in casting defects and refinement of the eutectic structure. A combination of hot forging and annealing has been initially promising in refining the brittle eutectic structure.

INTRODUCTION

The necessity for very high-temperature applications of structural materials with the desired properties of low density, good mechanical properties and environmental resistance has directed research efforts beyond titanium, nickel, and iron aluminides. Chromides, such as Cr_2Nb-based alloys, are a strong candidate for use at very high temperatures. However, after a careful review of the literature, little work appears to have been conducted in developing a good understanding of the effect of microstructural control on the mechanical behavior of Cr_2Nb-based alloys.

Development of this alloy is being carried out for use as critical hot components, such as in advanced fossil energy conversion systems. Cr_2Nb has a C15 (Laves phase) structure which is a relatively complicated crystal structure when compared with the more widely studied B2, $L1_2$, and $D0_{19}$ structures [1]. The crystal structure is so complex that dislocation motion is difficult at ambient temperatures. With regard to the Von Mises criteria, Cr_2Nb does not have a sufficient number of independent slip systems for uniform, extensive plastic deformation [2]. Since it has been shown [2] that the single-phase Cr_2Nb Laves alloys are extremely brittle at ambient temperatures, work has been concentrated on the Cr-Cr_2Nb two-phase compositions. The introduction of a soft Cr-rich phase has been shown [2] to have promising effects on improving the mechanical properties of Cr_2Nb intermetallics.

The objective of this research is to improve the ambient-temperature strength and ductility of a two-phase Cr-Cr_2Nb Laves phase alloy via thermomechanical treatments as well as the study of the effect of microstructural control on the mechanical behavior of this material. In addition, secondary processing techniques, such as hot forging and Hot Isostatic Pressing (HIPping), will be used to suppress casting defects and further refine the brittle eutectic structure. Theoretical modeling will be developed to relate microstructural features with the mechanical properties. Moreover, the results of this research can provide invaluable information for the development and selection of reliable intermetallics for high-temperature structural applications.

EXPERIMENTAL PROCEDURE

The materials which have been studied in this research are four compositions of the Cr-Cr_2Nb two-phase intermetallic system. The four alloy compositions are reported in Table 1. As shown in Table 1, the CN-45 composition contains 17 at.% Nb. It was once believed that the eutectic composition of this two-phase alloy was that of the CN-4 alloy (12 at.% Nb). However, work by Takeyama and Liu [2] has since shown that the eutectic composition is more like that of the CN-45 composition (17 at.% Nb). The recent work done by Thoma and Perepesko [3] has indicated that the actual eutectic composition is closer to 18.5 at.% Nb, which is the composition of the CN-84 alloy investigated in this study.

Chromium-niobium alloys weighing 350 g were prepared by arc melting and drop casting into pre-heated copper molds. High-purity niobium and chromium metal chips were used as charge materials in order to reduce the interstitial impurity (i.e. oxygen), and the alloys were melted in a high-vacuum (10^{-5} Pa) furnace. The preheating of the copper mold to 100°C before drop casting was done in order to control alloy solidification and reduce thermal shock and microporosity formation during drop casting [4,5].

Table 1. Alloy Compositions for the Cr_2Nb-based Alloys

Alloy	Atomic percent	Weight percent
CN-7	Cr - 94 % Nb - 6 %	Cr - 89.76 % Nb - 10.24 %
CN-4	Cr - 88 % Nb - 12 %	Cr - 80.41 % Nb - 19.59 %
CN-45	Cr - 83 % Nb - 17 %	Cr - 73.21 % Nb - 26.79 %
CN-84	Cr - 81.5 % Nb - 18.5 %	Cr - 71.14 % Nb - 28.86 %

Table 1 lists the composition (at.%) of CN (Cr-Nb) alloys investigated in this work. The alloys used in this study have nominal compositions of chromium with a variation of 6 to 18.5 at.% Nb. The alloys were placed in a covered alumina crucible and annealed under vacuum at 1600°C for 1 hour (h) + 4 h at 1200°C.

Optical micrographs for CN-7 and CN-4 at this annealing treatment are shown in Figs. 2 and 3, respectively. An additional annealing treatment of 2 days (d) at 1580°C + 2 d at 1200°C was performed on two (CN-4 and CN-7) of the four alloy compositions listed in Table 1 and shown by the optical micrographs in Figs. 4 and 5. Other annealing treatments which have been performed [6] include 1 h at 1400°C, 1 h at 1500°C, 1h at 1550°C, 4 h at 1550°C + 2 d at 1200°C, 1h at 1580°C, and 2 d at 1580°C. The effects of annealing on the microstructures and mechanical properties of these alloys were emphasized in this investigation. Microstructures of these alloys were examined by optical microscopy. The metallographic specimens were polished through 1 µm using conventional techniques. Samples were then etched in a solution of 15 gm KOH, 15 gm $K_3Fe(CN)_6$, and 90 ml H_2O for approximately 5 seconds.

Microhardness readings were taken for each specimen using a LECO M-400 Hardness Tester using an indenter load of 1 kg. An average of three to five readings taken randomly across the sample gives the reported hardness values. Compression specimens having a diameter of 6 mm and a length of 9 mm were cut by electro-discharged machining (EDM) from the annealed ingots. The specimens were tested under compression on an Instron testing machine at room temperature and 1000°C at a nominal strain rate of 3.3×10^{-3} s^{-1}. The elevated-temperature tests were carried out in vacuum (less than 7×10^{-4} Pa).

Coarsening studies were performed on the CN-4 and CN-7 compositions at 1200°C for the following times: 3h, 6h, 1d, 3d, 7d, 14d, and 30d. The microstructures were then examined in the scanning electron microscope in order to evaluate the volume fraction of precipitates within the Cr-rich phase. Image analysis techniques will be used to determine the average particle size and distribution due to different annealing times. Hot Isostatic Pressing (HIPping) to suppress and/or remove casting defects was carried out by Dr. Sarit Bhaduri of the Department of Mines, University of Idaho. HIPping was performed at 1610°C at a pressure of roughly 193 MPa. Hot forging was performed at 1200°C in vacuum to roughly 20% deformation at a strain rate of 3×10^{-4} s^{-1}.

RESULTS AND DISCUSSION

Microstructure and Phase Composition

The CN alloys contain two phases, the Cr_2Nb intermetallic phase and the chromium-rich solid solution which can contain as much as 5 at.% Nb at the eutectic temperature of 1620°C. Recent work by Liu et.al., [5] however, has revealed that the eutectic temperature may actually be closer to 1670°C, which agrees well with the results reported by Thoma and Perepesko [3].

The compositions of the phases in the alloys CN-7, CN-4, and CN-45 were determined by electron microprobe analyses for an average of three points in each respective phase, as reported in Table 2. From the phase diagram in Fig. 1, we see that the intermetallic phase in the eutectic structure has an average composition of 70 at.% Cr - 30 at.% Nb, which, according to the results in Table 2, reveals that the phase identified by microprobe analyses in the eutectic structure is in fact the Cr_2Nb Laves-type intermetallic phase. Figure 2 shows the optical micrograph of CN-7 annealed for 1 h at 1600°C + 4 h at 1200°C. In this alloy, the Cr-rich patches cover most areas, and a small amount of the Laves-containing eutectic phase can be seen along the Cr-rich boundaries. At lower annealing temperatures, such as 1100°C-1300°C, which have been studied [2,4,5], this brittle eutectic phase exists as an interconnected skeleton along the Cr-rich regions as seen in Fig. 6, but in the case of the microstructure seen in Fig. 2, the anneal has broken up the eutectic phase that was once interconnected along the Cr-rich regions. The 88 at.% Cr - 12 at.% Nb (CN-4) alloy is shown in Fig. 3 with the same annealing history as CN-7 in Fig. 2. As seen in Figure 3, the lighter patches in the CN-4 composition are the chromium-rich phase which is surrounded by the Laves-containing brittle eutectic phase. Some very fine dark spots can be seen within the Cr-rich patches in both Figures 2 and 3, and these are the Cr_2Nb precipitates that precipitate out of the supersaturated Cr-rich matrix upon annealing. In each of these alloy compositions, the Cr-rich phase is the matrix, thus indicating from the phase diagram that these are hypoeutectic compositions.

It has been shown [4] that the precipitation of the Cr_2Nb Laves-phase particles from the Cr-rich phase is sluggish. These precipitates are extremely fine, with a size of less than 1 μm for an alloy annealed for 3 d at 1100°C [2,4]. Annealing at temperatures of 1500°C to 1600°C did

Table 2. Electron Microprobe Analysis of the Cr_2Nb Alloys

Alloy	Anneal Condition	Cr_2Nb phase in Eutectic structure (at.%)	Cr-rich phase (at.%)
CN-7	1h/1600°C + 4h/1200°C	Cr = 68.8 % Nb = 31.2 %	Cr = 96.2 % Nb = 3.8 %
CN-4	1h/1600°C + 4h/1200°C	Cr = 69.3 % Nb = 30.7 %	Cr = 96.6 % Nb = 3.4 %
CN-45	1h/1600°C + 4h/1200°C	Cr = 68.6 % Nb = 31.4 %	Cr = 97.2 % Nb = 2.8 %

* analysis of the Cr-rich phase also includes the fine Cr_2Nb precipitates

not reveal the fine Cr_2Nb particles within the Cr-rich phase. These precipitates were partially dissolved due to an increase in the solubility of Nb in Cr at these temperatures and the remainder of the particles migrated to the Laves-containing eutectic phase, thereby coarsening it. Thus, we see that there are two competing mechanisms occurring during the annealing treatment; (1) break-up of the eutectic phase and (2) coarsening of the Laves-containing eutectic phase due to Cr_2Nb particles migrating from the Cr-rich phase at high temperatures. Upon furnace cooling from 1580°C and/or 1600°C, very fine particles once again precipitate out in the Cr-rich phase. Additional annealing at 1200°C causes a coarsening of these fine particles. This result can especially be seen in the micrographs shown in Figs. 4 and 5 for CN-7 and CN-4 annealed 2 d at 1580°C + 2 d at 1200°C.

Hardness

Microhardness results are presented in Table 3 for the CN-7, CN-4, and CN-45 alloys under different annealing conditions. The effects of annealing temperature on hardness are shown in Fig. 7 for the CN-4 alloy. No microcracking was observed at the tips of the microhardness indents as was previously reported for alloys in the as-cast condition [2]. The hardness decreases with decreasing niobium concentration and increasing amount of the soft Cr-rich phase. Previous work by Liu [7] has indicated that the hardness tends to decrease as the coarsening of the fine Cr_2Nb particles within the Cr-rich phase occurs for temperatures ranging from 950°C to 1200°C, as shown in Fig. 7. In the present investigation, it was found that annealing at high temperatures near the eutectic temperature (1550°C to 1600°C) leads to an increase in hardness, as reported in Table 3.

Table 3. Microhardness Values (DPH) for the Cr_2Nb-based Alloys

Annealing Treatment	CN-4	CN-7	CN-45
6 h/1200°C	476	373	
24h/1200°C	453	339	
3d/1200°C	454	327	
7d/1200°C	423	324	
14d/1200°C	416	319	
30d/1200°C	405	308	
1h/1400°C	465	367	616
1h/1500°C	494	393	618
1h/1550°C	502	424	618
1h/1580°C	513	406	613
2d/1580°C	508	445	–
2d/1580°C + 2d/1200°C	418	341	–
1h/1600°C + 4h/1200°C	479	429	–

* all anneals shown are performed on as-cast material, unless otherwise noted

Annealing at these high temperatures has the following effects: (a) dissolution of the fine Cr_2Nb precipitates in the Cr-rich phase due to an increase in the solubility limit of Nb in Cr; (b) coarsening of the Laves-containing eutectic phase due to migration of the Cr_2Nb particles from the Cr-rich phase, (c) break-up of the eutectic phase, and; (d) re-precipitation of extremely fine Cr_2Nb particles in the Cr-rich phase upon cooling from the high-temperature anneals. It is this fine re-precipitation that is believed to lead to the increase in hardness. Upon additional annealing of the sample at 1200°C after annealing for 1 h at 1600°C or 2 d at 1580°C, we see that the hardness once again decreases due to the coarsening of the Cr_2Nb precipitates within the Cr-rich region as discussed in the work by Liu [7] and seen by the results presented in Table 3 and Fig. 7. In addition, we see that the hardness also decreases when the material is annealed for prolonged periods at a fixed temperature, such as the drop in hardness values from the coarsening studies reported in Table 3 for the CN-4 and CN-7 compositions that were annealed at 1200°C over a period ranging from 6 hours to 30 days. Once again, this drop in hardness is attributed to the particle coarsening behavior of the Cr_2Nb precipitates within the Cr-rich regions. These coarsening studies at 1200°C were done in order to further understand the precipitation and growth kinetics of the Cr_2Nb particles in the supersaturated Cr-rich regions.

Compression Testing

The 0.2 % yield strength and compressive ductility of 94 at.% Cr-6 at.% Nb (CN-7) and 88 at.% Cr-12 at.% Nb (CN-4) alloys at room temperature are reported in Table 4. At room temperature, the yield strengths of CN-7 and CN-4 are higher than 700 and 900 MPa, respectively, for an annealing condition of 3 d at 1100°C. A substantial improvement in room-temperature yield strength and compressive ductility was seen for the CN-7 and CN-4 alloys annealed for 1 h at 1600°C + 4 h at 1200°C. The CN-45 alloy tested for this annealed condition showed reasonable ductility with very high strength at room temperature, as reported in Table 4. Some improvement in strength, together with a significant increase in room temperature compressive ductility was seen for the alloys annealed for 4 h at 1550°C + 2 d at 1200°C. The improvement in ductility in all cases can be attributed to the break-up of the coarse/brittle eutectic structure due to these high temperature anneals (1 h at 1600°C and 4 h at 1550°C).

Table 4. Compressive Properties of CN Alloys Tested at Room Temperature in Air

Alloy No.	Heat Treatment	Composition (at.%)	Strength, MPa (ksi)		Ductility (%)
			Yield	Ultimate	
CN-7	3d/1100°C	94 Cr-6 Nb	702(102)	1261(183)	9.5
CN-7	1h/1600°C +4h/1200°C	94 Cr-6 Nb	1029(149)	1733(251)	20.7
CN-7	4h/1550°C +2d/1200°C	94 Cr-6 Nb	668(97)	1477(215)	23
CN-4	3d/1100°C	88 Cr-12 Nb	960(139)	1760(255)	5.4
CN-4	1h/1600°C +4h/1200°C	88 Cr-12 Nb	1327(192)	1546(224)	8.8
CN-4	4h/1550°C +2d/1200°C	88 Cr-12 Nb	1247(181)	1345(195)	10.1
CN-4	HIP @ 1610°C +3d/1200°C	88 Cr-12 Nb	1077(157)	1562(227)	10
CN-45	1h/1600°C +4h/1200°C	83 Cr-17 Nb	1763(256)	1824(265)	12.2
CN-45	4h/1550°C +2d/1200°C	83 Cr-17 Nb	1698(246)	1840(267)	8.9

Hot Isostatic Pressing (HIPping) at 1610°C + annealing 3 d at 1200°C of the CN-4 composition showed only a marginal break-up of the brittle eutectic phase and negligible improvement in room temperature strength and compressive ductility over other anneals that have been performed as reported in Table 4.

As shown in Table 5, samples annealed for 1 h at 1600°C + 4 h at 1200°C showed some improvement in strength at 1000°C over similar tests performed on samples annealed for 3 d at 1100°C. However, there was little change in compressive ductility from the previous tests performed for samples annealed 3 d at 1100°C. As the test temperature increased, the strength decreased and the ductility increased for all tests. The CN-45 alloy showed very limited ductility when compared with the CN-4 and CN-7 results at 1000°C. For the CN-4 alloy annealed 1 h at 1600°C + 4 h at 1200°C, the yield strength at 1000°C is approximately 780 MPa, which is substantially stronger than conventional nickel-base superalloys; for example, the yield strength of IN713C at 1000°C is about 300 MPa [8]. At 1000°C, both CN-7 and CN-4 can be deformed with compressive ductilities larger than roughly 20 %. These results reveal that the two-phase intermetallic alloys based on Cr_2Nb have high strength with decent ductility at all test temperatures. In addition, we can see that the break-up of the Laves-containing eutectic phase via annealing at higher temperatures (1550° to 1600°C) results in a considerable increase in strength and compressive ductility at room temperature and a slight increase in strength with good ductility at 1000°C in vacuum.

FUTURE WORK

Despite the improvements seen as a result of annealing at temperatures above 1580°C, there is the disadvantage of Cr vaporization from the surface of the material and in extreme cases, partial melting of the material, thus providing less usable material for testing as one must remove and/or avoid these areas when machining specimens for mechanical testing. In an attempt to alleviate this problem, a combination of hot forging and annealing at lower temperatures (1500°C and below) has shown to be promising in effectively refining the brittle eutectic structure. Continued work will be undertaken to further explore this method of microstructural refinement and ductility enhancement. It is hoped that a theoretical model, such as finite-element modeling of compression tests, can be developed which will correlate the effects of changes in the microstructure via thermomechanical treatment with the mechanical behavior of these two-phase alloys based on Cr_2Nb. These studies will lead to a mechanistic understanding of the effects of microstructural control via thermomechanical treatment on the fracture behavior of these alloys. Other image analysis techniques will be used to determine average particle size and distribution due to different annealing times studied in the coarsening experiments. It is hoped that these studies will help to shed some light on the precipitation kinetics of the Cr_2Nb phase within these alloys. In addition, tensile tests will be performed on the alloys at different temperatures and anneal conditions in order to study the effect of microstructural refinement of the brittle eutectic structure on the strength and ductility of the material in tension.

Table 5. Compressive Properties of CN Alloys Tested at 1000°C in Vacuum

Alloy No.	Heat Treatment	Composition (at.%)	Strength, MPa (ksi)		Ductility (%)
			Yield	Ultimate	
CN-7	3d/1100°C	94 Cr-6 Nb	436(63)	738(107)	32.7
CN-7	1h/1600°C +4h/1200°C	94 Cr-6 Nb	580(84)	1069(155)	27.9
CN-7	4h/1550°C +2d/1200°C	94 Cr-6 Nb	405(59)	790(115)	31.4
CN-4	3d/1100°C	88 Cr-12 Nb	685(99)	856(124)	22.8
CN-4	1h/1600°C +4h/1200°C	88 Cr-12 Nb	778(113)	1079(157)	19.8
CN-4	4h/1550°C +2d/1200°C	88 Cr-12 Nb	711(103)	845(123)	17.1
CN-4	HIP @ 1610°C +3d/1200°C	88 Cr-12 Nb	658(96)	711(112)	16.6
CN-45	1h/1600°C +4h/1200°C	83 Cr-17 Nb	994(144)	1076(156)	8.1
CN-45	4h/1550°C +2d/1200°C	83 Cr-17 Nb	1698(246)	1840(267)	10.3

ACKNOWLEDGMENTS

The authors wish to give thanks to Nancy Cole and Rod Judkins of the Oak Ridge National Laboratory for financial support of this program. Thanks are due to C.A. Carmichael, D.H. Pierce, J. Wright, T. Henson, and M. Williams for their technical assistance. This work is sponsored by the Fossil Energy AR & TD Materials Program, U.S. Department of Energy, under subcontract 11X-SP173V to the University of Tennessee with Martin Marietta Energy Systems, Inc.

REFERENCES

1. T. Takasugi, S. Hanada, and K. Miyamoto, *J. Mater. Res.*, vol. 8, no. 12, (Dec. 1993), pp. 3069-3077.

2. M. Takeyama and C.T. Liu, *Materials Science and Engineering*, A132, (1991), pp. 61-66.

3. D.J. Thoma and J.H. Perepesko, *Materials Science and Engineering*, vol. A156, (1992), pp. 97-108.

4. C.T. Liu, J.A. Horton and C.A. Carmichael, pp. 297-307 in *Proc. 7th Annual Conf. on Fossil Energy Materials*, ORNL/FMP-93/1, Oak Ridge National Laboratory, July 1993.

5. C.T. Liu, J.A. Horton and C.A. Carmichael, pp. 377-390 in *Proc. 8th Annual Conf. on Fossil Energy Materials*, ORNL/FMP-94/1, Oak Ridge National Laboratory, August 1994.

6. J.A. Cook, P.K. Liaw and C.T. Liu, pp. 401-412 in *Proc. 8th Annual Conf. on Fossil Energy Materials*, ORNL/FMP-94/1, Oak Ridge National Laboratory, August 1994.

7. J.A. Cook, P.K. Liaw, and C.T. Liu, Fracture Behavior of Cr_2Nb-based Intermetallics, in *Fatigue and Fracture of Ordered Intermetallic Materials II*, TMS (the Minerals, Metals and Materials Society) Proceedings of the 1994 Materials Week in Rosemont, Ill (in press).

8. C.T. Liu, pp. 375-383 in *Proc. 6th Annual Conf. on Fossil Energy Materials*, ORNL/FMP-92/1, Oak Ridge National Laboratory, July 1992.

9. *Engineering Properties of Alloy 713C*, International Nickel, New York, 1968.

10. H.J. Goldschmidt and J.A. Brand, *J. Less-Common Met.*, 3 (1961) p. 44.

11. T.B. Massalski, J.L. Murray, L.H. Bennett and H. Baker (eds.) *Binary Alloy Phase Diagram*, American Society for Metals, Metals Park, OH, 1986.

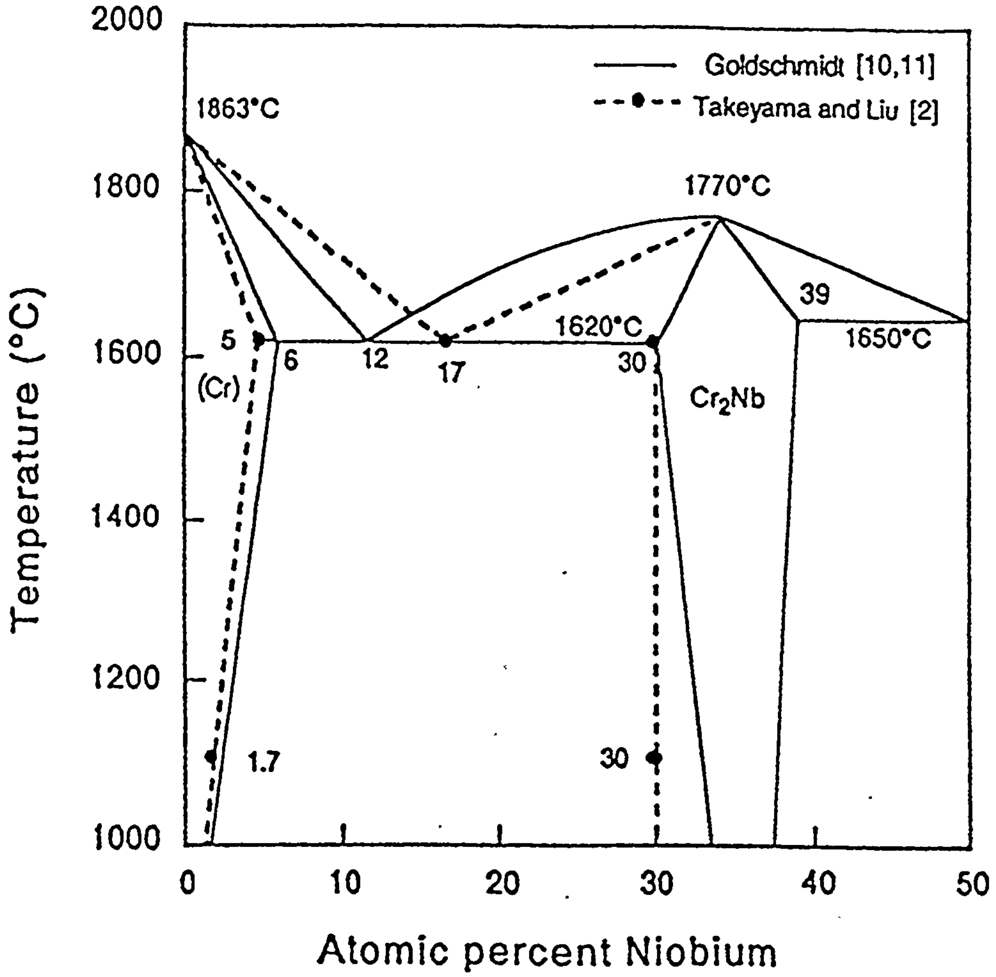

Figure 1. The Chromium-Niobium Binary Phase Diagram.

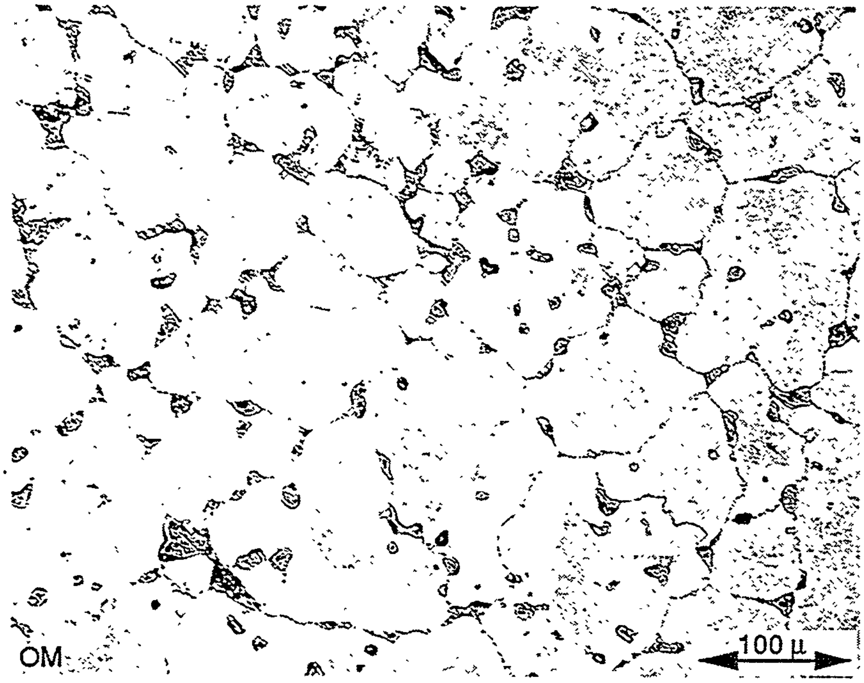

Figure 2. Sample CN-7 (94 at.% Cr-6 at.% Nb) annealed 1 hour at 1600°C plus 4 hours at 1200°C in vacuum. Cr-rich regions (light) surrounded by Laves-containing eutectic phase (dark).

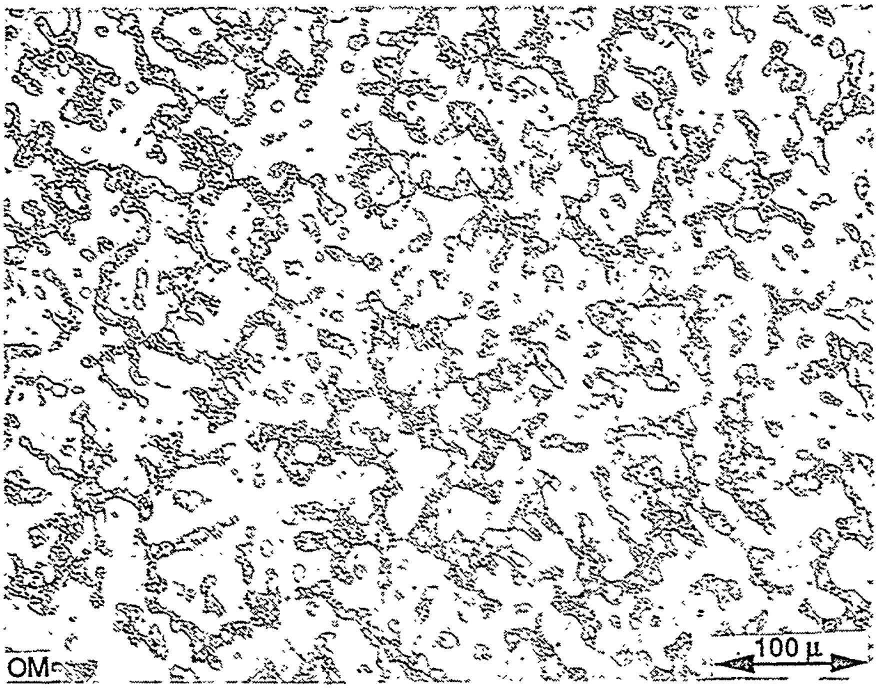

Figure 3. Sample CN-4 (88 at.% Cr-12 at.% Nb) annealed for 1 hour at 1600°C plus 4 hours at 1200°C in vacuum. Cr-rich regions (light) surrounded by Laves-containing eutectic phase (dark).

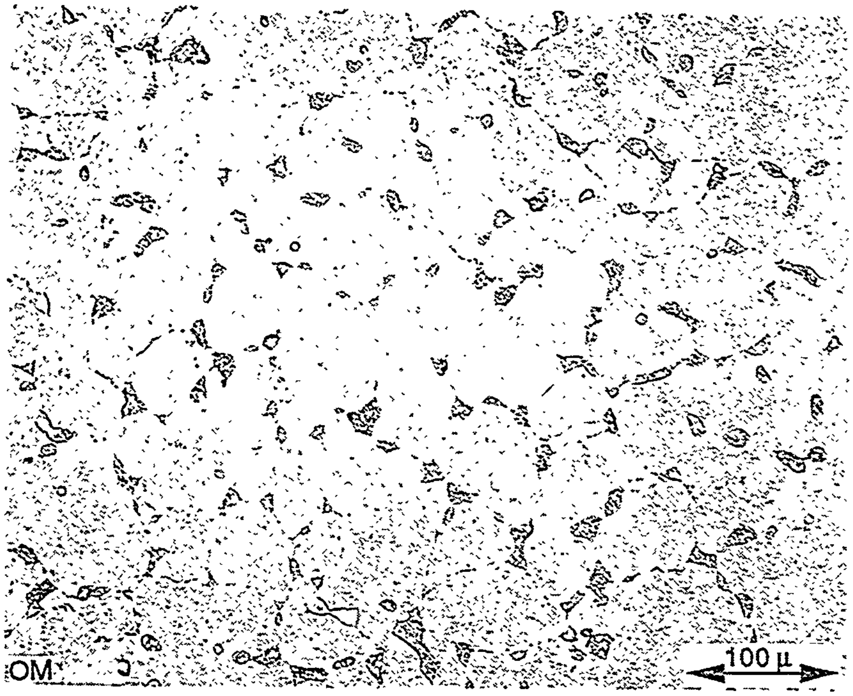

Figure 4. CN-7 - annealed for 2 days at 1580°C plus 2 days at 1200°C in vacuum.

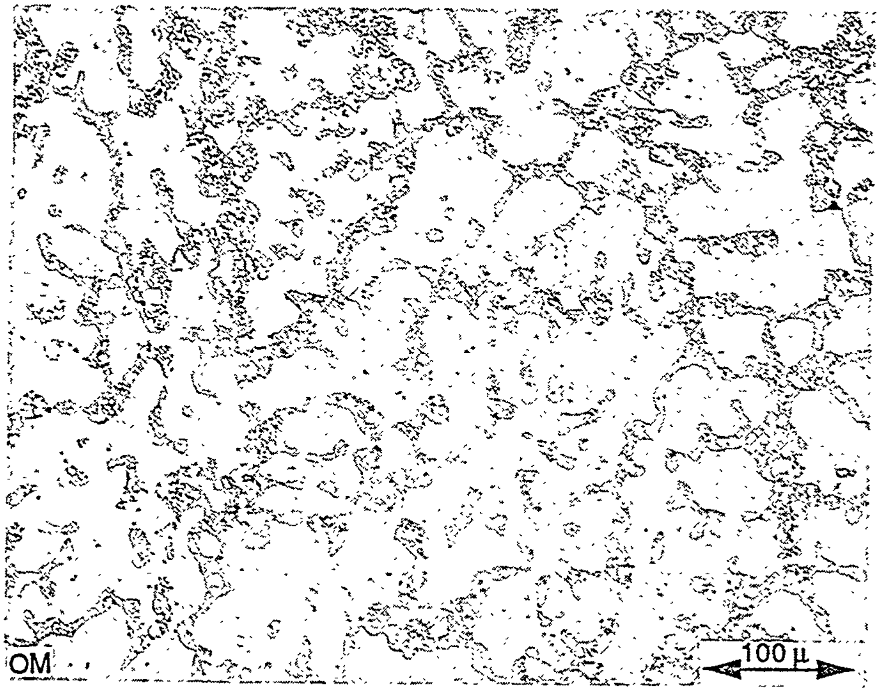

Figure 5. CN-4 - annealed for 2 days at 1580°C plus 2 days at 1200°C in vacuum.

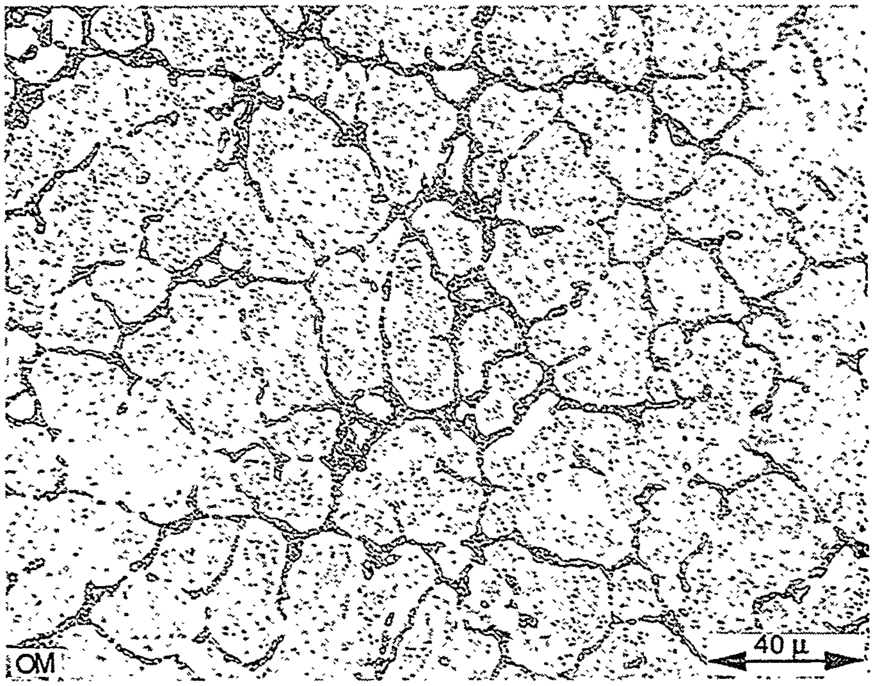

Figure 6. Sample CN-7 (94 at.% Cr-6 at.% Nb) annealed 1 day at 1300°C in vacuum. Cr-rich regions (light) surrounded by Laves-containing eutectic phase (dark).

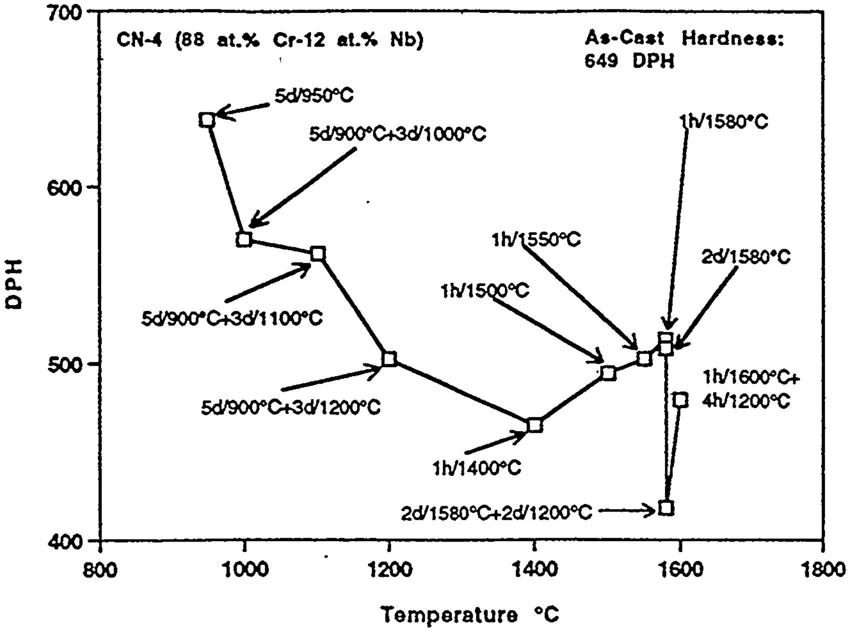

Figure 7. Hardness profile for CN-4 for a variety of annealing treatments illustrating how precipitate coarsening at lower annealing temperatures (950-1200°C) can reduce the hardness of the material.

SESSION III - WORKSHOP ON MATERIALS CHALLENGES IN ADVANCED FOSSIL FUELED POWER SYSTEMS

SUMMARY

WORKSHOP ON NEW MATERIALS DEVELOPMENT AND APPLICATIONS

A *Workshop on Materials Challenges in Advanced Fossil Fueled Power Systems* was held as part of the Ninth Annual Conference on Fossil Energy Materials. The workshop opened with a plenary session that included several brief overviews from a panel of sponsors, system designers, manufacturers, producers, and users who presented different perspectives on issues for their particular systems. Systems discussed included integrated gasification combined cycle (IGCC), pressurized fluidized bed combustion (PFBC), hot gas filters, and indirectly fired combined cycles. A question and answer session followed the presentations.

Workshop panelists and the primary emphasis areas of their presentations were:

Dan Seery	Senior Program Manager; United Technologies Research Center; East Hartford, Connecticut	Combustion 2000, HIPPS system design
Gerry Bruck	Program Manager, Advanced Fossil Energy Systems; Westinghouse Electric Corporation; Pittsburgh, Pennsylvania	Materials selections for advanced coal-fueled power systems
Larry Ruth	Division Director/DOE Pittsburgh Energy Technology Center; Pittsburgh, Pennsylvania	Combustion 2000, HIPPS, and LEBS
Ted McMahon	Project Manager/Coal Gasification and Hot-Gas Cleanup Division; DOE Morgantown Energy Technology Center; Morgantown, West Virginia	Hot-gas cleanup materials
John Mundy	DOE-Basic Energy Sciences; Division of Materials Sciences, Washington, DC	BES Materials R&D and its relationship to Fossil Energy
Tom Gibbons	Director, Materials and Water Chemistry, Power Plant Laboratories; ABB Combustion Engineering; Windsor, Connecticut	Materials selections for pulverized coal power plants
Juhani Isaksson	Ahlstrom Pyropower; Karhula, Finland and San Diego, California	Circulating pressurized fluidized bed combustion systems and hot-gas filtration
Nguyen Minh	Space Systems Engineering, Aerospace Systems and Equipment; AlliedSignal Inc.; Torrance, California	HIPPS design and ceramic heat exchangers
Mo Bary	Program Manager, Black & Veatch, Overland Park, Kansas	Warren Station EFCC Repowering Project

Following the plenary session, four separate working group sessions were conducted. The working groups addressed issues related to:

Session A - Hot Gas Filters
Session B - Metallic Heat Exchangers
Session C - Ceramic Heat Exchangers
Session D - Metallic Components

The conference and workshop are part of the overall AR&TD Materials Program strategic planning. This workshop provided the opportunity to have major materials issues discussed from a systems point of view by the expert panelists followed by detailed discussions in the working groups on how best to address these issues in the context of the AR&TD Materials Program. Results of the workshop will be incorporated into program planning activities.

SESSION IV - NEW ALLOYS AND FUNCTIONAL MATERIALS

ODS IRON ALUMINIDES

I. G. Wright, C. G. McKamey, and B. A. Pint

Oak Ridge National Laboratory
P. O. Box 2008
Oak Ridge, TN37831-6156

ABSTRACT

Since oxide dispersion-strengthened (ODS) FeCrAl-based alloys have sufficient creep strength and good oxidation resistance at the very high temperatures of interest for the primary heat exchanger in advanced, closed-cycle gas turbine systems, they constitute viable alternative candidates to ceramics. A major life-limiting factor of these alloys is the ability to continue to form a protective scale of aluminum oxide, a factor proportional to the total amount of aluminum contained in the alloy. Fe_3Al has oxidation resistance comparable to that of the FeCrAl-based alloys, and significantly superior sulfidation resistance. Also, because of its larger reservoir of aluminum, Fe_3Al would be expected to exhibit longer lifetimes at the temperatures of interest. Since the strengthening effects of ODS processing are expected to confer similar high-temperature creep properties to those found for the FeCrAl-based alloys, ODS-Fe_3Al is considered to have excellent potential for the very high-temperature heat exchanger application. The program effort on ODS Fe_3Al includes examination of the properties of available ODS-FeCrAl alloys; development of mechanical alloying parameters for ODS-Fe_3Al; determination of the effects of a dispersion of reactive element oxides on the high-temperature oxidation behavior of Fe_3Al; and evaluation of methods for joining them.

INTRODUCTION

There has been a recent increase of interest in advanced cycles that involve indirectly-fired gas turbines, in which coal- or gas-fired high-temperature heat exchangers are used to heat a working fluid in a closed system[1]. In a program conducted as part of the European COST-501 Concerted Action Project (Round 2, Work Package 4), available alloys based on FeCrAl-Y_2O_3 (listed in Table 1) were evaluated for use in the main heat exchanger in a similar closed-cycle gas turbine application[2,3,4,5,6,7,8,9,10,11,12]. One of the currently available ODS FeCrAl alloys was found to meet the strength requirements for this application, in which the working fluid at 0.9 MPa (131 psi) flowing at 5,889 kg/hr (12,955 lb/hr) was to be heated from 800 to 1100°C (1472 to 2012°F) over a tube length of 4 m (13 ft).

FeCrAl-based alloys have long been regarded as having excellent resistance to high-temperature oxidation, with reactive metal or reactive metal oxide additions playing some beneficial role[13,14,15]. However, much of the information on oxidation behavior was generated from relatively short-term exposures. In the very high-temperature heat exchanger application, an area of unexpected but major concern with these alloys is their ability to maintain a protective oxide scale for the extended times necessary for commercial application. After extended exposure times, these alloys suffer increasing loss of scale through spallation, as indicated by the trend to weight losses as shown in Fig. 1. The oxidation life of these alloys is determined by their ability to form or reform a protective alumina scale, and can be related to the time for the aluminum content of the alloy to be depleted to some minimum level; this, in turn, is a function of the total aluminum content of the alloy. This dependence on total available aluminum content is illustrated by results[8] from the COST-501 project as summarized in Fig. 2, which relates the effective life of the alloy tube (represented as 'time to breakaway') to its wall thickness.

Table 1. Nominal Compositions of Available Ferritic ODS Alloys (weight percent)

Alloy	Fe	Cr	Al	Mo	Ti	Y_2O_3
MA 956	Bal	20.0	4.5	—	0.5	0.5
PM 2000	Bal	20.0	5.5	—	0.5	0.5
ODM 751	Bal	16.5	4.5	1.5	0.6	0.5
ODM 331	Bal	13.0	3.0	1.5	0.6	0.5

The major factors that result in depletion of the reservoir of aluminum in the alloy are the inherent growth rate of the oxide, a process that consumes aluminum, and the tendency for the scale to spall, which also results in a net loss of aluminum from the alloy together with a (temporary) increase in oxide growth rate in the area affected by spallation. When the alloy aluminum reservoir falls below the minimum level at which an alumina layer can be reformed, less-protective oxides of the other alloy

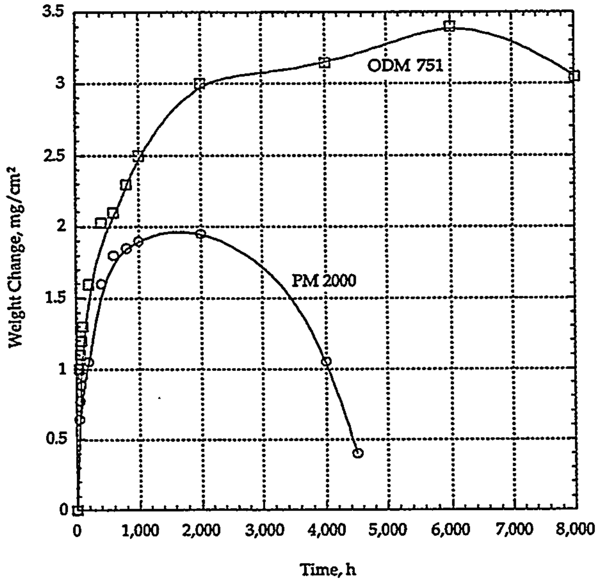

Figure 1. Oxidation kinetics for ODS-FeCrAl-Y_2O_3 alloys in air at 1200°C cycled to room temperature every 48 hr (after ref. 8).

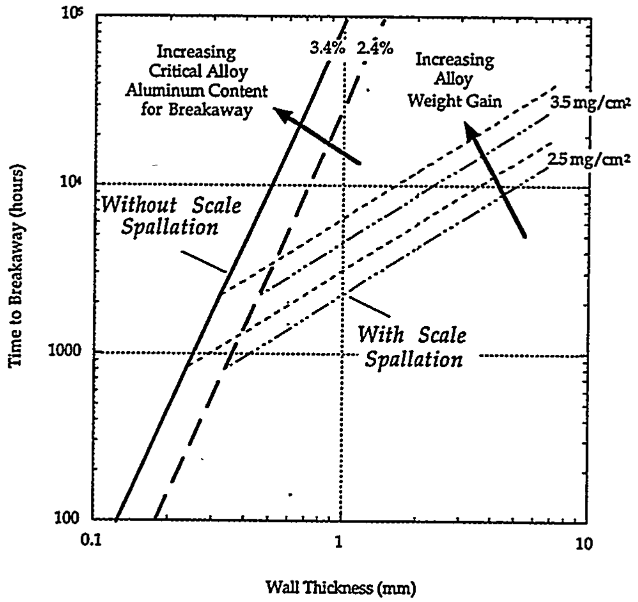

Figure 2. Effects of alloy oxidation rate, oxide spallation, and tube wall thickness on lifetime (time to onset of breakaway oxidation) of ODS-FeCrAl alloys (after ref. 8).

constituents will form in areas where the initial scale spalls, and the rate of oxidation may rapidly increase as the alloy undergoes breakaway oxidation. A further complication is that, according to results from the COST-501 project, differences among alloys that are insignificant for oxidation growth rate and tendency to spall can dramatically affect the time to breakaway. Hence, similar components manufactured from alloys of nominally similar compositions may fail at quite different times.

Iron-aluminum alloys have the obvious potential to provide longer service lives because of their inherently larger aluminum reservoirs (15.8 vs 3 to 5.5 wt.% Al), provided that their oxidation and mechanical properties are similar to the FeCrAl-based alloys. Iron-aluminum alloys have been regarded for many years as having excellent resistance to high-temperature oxidation[16,17,18,19], and this has been confirmed by the recent work at ORNL on Fe_3Al alloys[20]. However, until this recent work , the development of usable ferritic alloys was restricted by their poor mechanical properties, especially the lack of ambient-temperature ductility which impaired fabricability. The lack of strength at temperatures above about 600°C is still a problem for the conventionally-cast alloys. The potential for increasing the creep rupture strength of iron aluminides by ODS processing was demonstrated in the 1960's[21]: the incorporation of 12 volume percent of approximately 1 μm Al_2O_3 to Fe-40 at. percent Al improved the high-temperature (732°C) creep strength by a factor of 4, compared to the dispersion-free, cast alloy.

Overall, there appears to be a niche application for an ODS version of Fe_3Al in components such as heat exchanger tubes that must operate at very high temperatures and for which the obvious competition is from ceramic materials. The work in this program is aimed at evaluating this potential.

PRELIMINARY EXAMINATION OF AVAILABLE FERRITIC ODS ALLOYS

A sample of an ODS FeCrAl alloy in the form of a round bar approximately 13 mm (0.5 in.) diameter was obtained from Dour Metal for characterization. Chemical analysis of the alloy showed that it was probably Dour Metal alloy ODM 331, rather than ODM 751 (see Table 1). The grain size of the as-received alloy was determined by metallographic techniques to be approximately 2 µm , as shown in Fig. 3. Round specimens with a gage diameter of approximately 3 mm (0.12 in.) and a gage length of 12.7 mm (0.50 in.) were machined from the as-received bar, and subjected to creep-rupture testing in air. The first creep test at 1000°C (1832°F) and 55 MPa (8 ksi) failed in only a few minutes, before sufficient data could be recorded. A subsequent test at 816°C (1500°F) with a stress of 34.5 MPa (5 ksi) produced the data plotted in Fig. 4; the rupture-life was less than 5 hours, with a final elongation of 119.3 percent, and the minimum creep rate (MCR) was approximately 7.75%/h. This unexpectedly-low creep-rupture resistance was attributed to the small grain size of the as-received material.

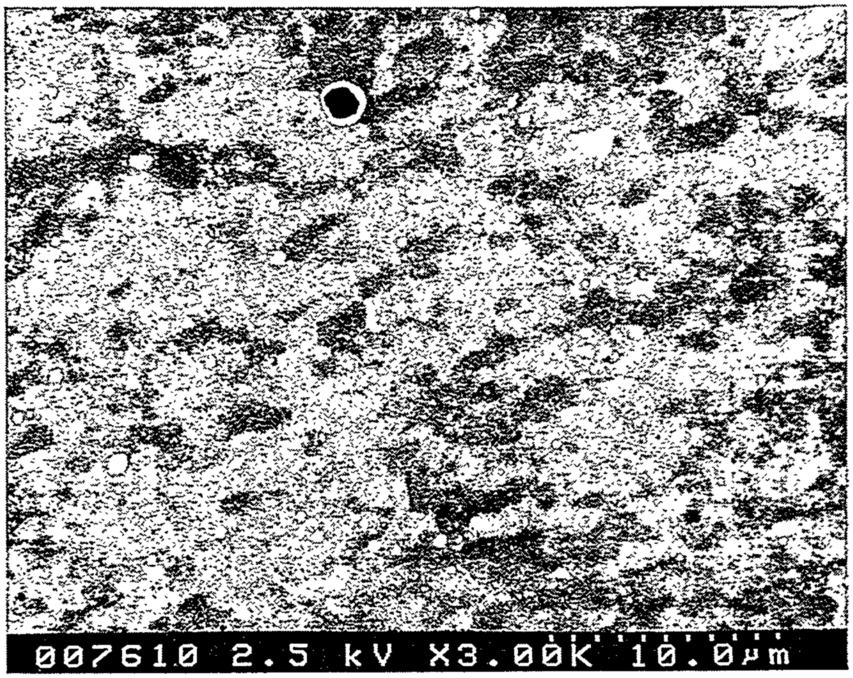

Figure 3. Secondary scanning electron image of a transverse cross section of ODM-331 showing the small grain size and the presence of cavities and oxide particles.

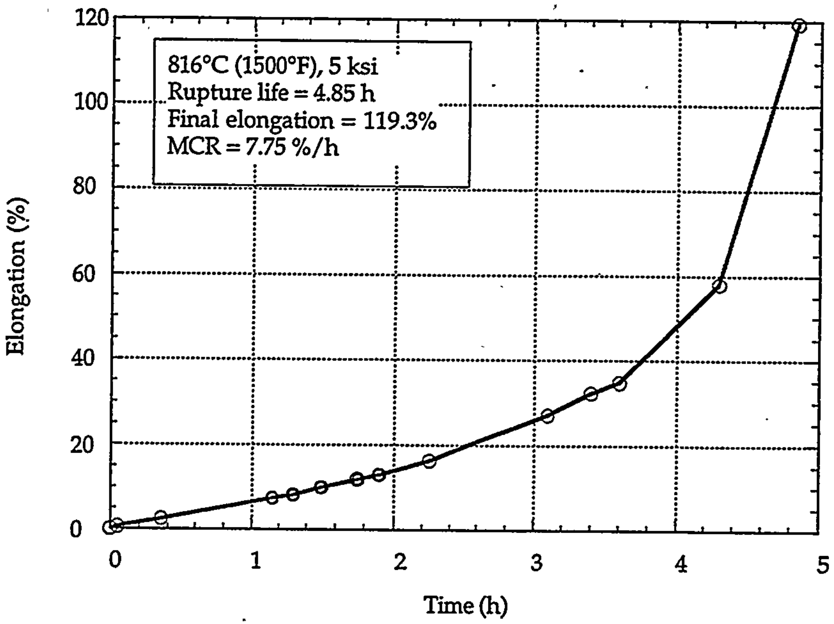

Figure 4. Creep-rupture curve for ODM-331 in the as-received and machined condition, tested at 816°C at a stress of 34.5 MPa (5 ksi).

In an attempt to produce larger, elongated grains to increase the creep strength, a heat treatment of 25 hours at 1350°C (2462°F) in vacuum was performed on a small sample of the alloy. However, no etchant could be found that would satisfactorily reveal the grain structure resulting from the heat treatment. A drawback of this heat treatment was obvious evaporation of chromium from the outer surface of the specimen, and an observed increase in the size of some of the oxide particles in the matrix. In the absence of a means of measuring the alloy grain size, further testing of this alloy was postponed.

A second series of tests was conducted on a sample of an ODS Fe_3Al-based alloy produced at ORNL (designated FAS-3Y). The nominal composition of this alloy was Fe-28Al-2Cr-0.05B (at.%), to which 0.2 cation% Y_2O_3 was added by mechanical alloying (see following section). Tensile specimens with gage dimensions of 12.7 x 0.75 x 3.2 mm (0.50 x 0.030 x 0.126 in.) were punched from the as-rolled sheet and heat treated for 8 h at 1275°C (2327°F) in argon to produce the large-grained banded grain structure shown in Fig. 5. The results of tensile tests conducted in air at room temperature, 800, and 1000°C (1472 and 1832°F) using a strain rate of 3.3×10^{-3} s^{-1} are shown in Table 2. Typical data for monolithic FAS, two other monolithic ORNL-developed iron aluminide alloys, and the Dour Metal alloy ODM-331, are included for comparison. At room temperature, the FAS-3Y alloy had a similar tensile strength but a lower ductility compared to the FA-180 alloy, as

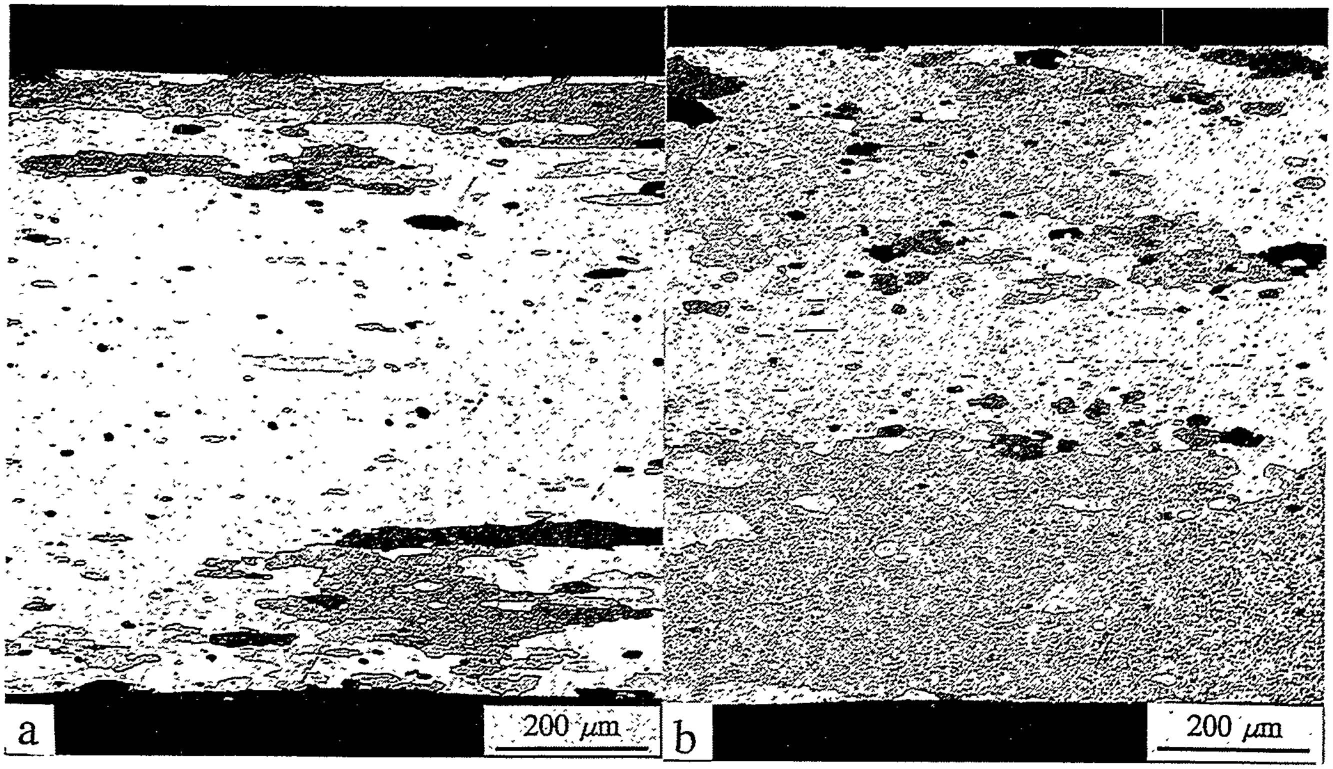

Figure 5. Optical micrographs of FAS-3Y after a heat treatment of 8 h at 1275°C in air; shown is the through-thickness direction (a) parallel to and (b) perpendicular to the rolling direction.

Table 2. Comparison of Tensile Properties of Alloy FAS-3Y With Other Iron-Based Alloys

Property	FAS-3Y	FAS	FA-129	FA-180	ODM-331
20°C					
YS (MPa)	643	394	380	620	
UTS (MPa)	959	679	900	900	
Elongation (%)	2	9	15	8	
800°C					
YS (MPa)	110			140	
UTS (MPa)	120			148	
Elongation (%)	36			79	
900°C					
YS (MPa)					160
UTS (MPa)					170
Elongation (%)					10
1000°C					
YS (MPa)	43			27	
UTS (MPa)	49			27	
Elongation (%)	12			137	

FA-129 = Fe-28Al-5Cr-0.5Nb-0.2C (at.%)
FA-180 = Fe-28Al-5Cr-0.5Nb-0.8Mo-0.025Zr-0.05C-0.005B (at.%)

expected for an oxide-dispersion-strengthened alloy. The FAS-3Y specimen failed in a ductile-dimple manner, with particles at the base of the dimples. Since tensile properties are usually better in iron aluminides with finer-grained microstructures, it is anticipated that the strength of this alloy will improve with heat treatment at a lower temperature.

A creep-rupture test of this alloy was initiated at 800°C (1472°F) with an initial stress of 34.5 MPa (5 ksi). At this stress, the minimum creep rate appeared to be almost zero. After approximately 240 hours, the stress was increased to 48.3 MPa (7 ksi) and the test was allowed to proceed to rupture. As shown in Fig. 6, rupture occurred suddenly after 383.45 hours, at a specimen elongation of about 3 percent. Another test at 1000°C (1832°F) started at 13.8 MPa (2 ksi). Since there was no discernible creep after 240 hours, the stress was increased to 20.7 MPa (3 ksi), and then to 27.6 MPa (4 ksi) before failure occurred after 477 hours, with a final elongation of 6.9 percent. Further creep tests on FAS-3Y will be initiated following the fabrication of a new sample of FAS-3Y material and the development of thermomechanical processing to produce the desired large, elongated grain structure.

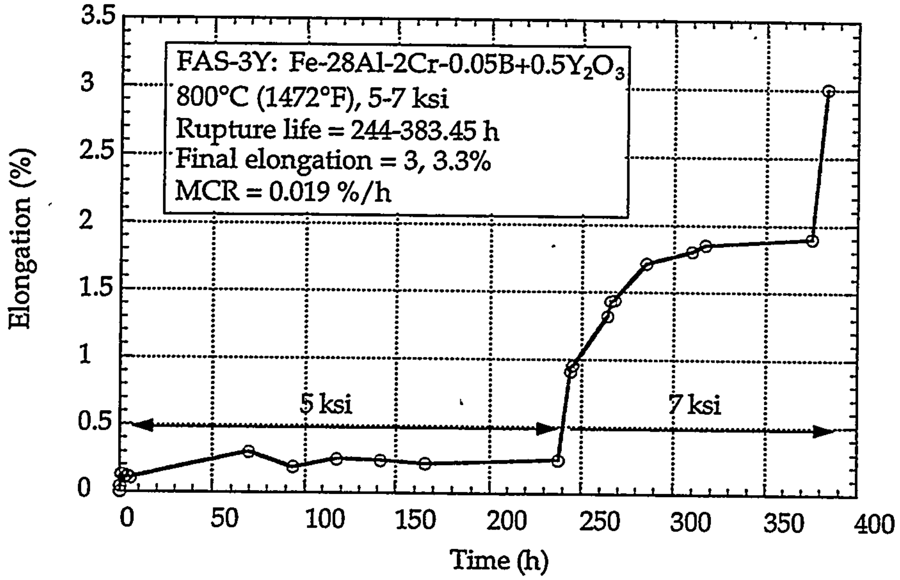

Figure 6. Creep-rupture curve of FAS-3Y heat treated 8 h at 1275°C and tested at 800°C.

The limited creep-rupture data generated so far on the FAS-3Y material suggests a lower creep resistance than the ODM alloys produced by Dour Metal. However, with the limited number of samples available, the best fabrication and heat treating conditions to produce the desired microstructure for maximum strength have not been determined. Plans have been made to obtain a larger sample of this alloy from a commercial vendor.

DEVELOPMENT OF MECHANICAL ALLOYING PARAMETERS FOR ODS Fe_3Al

Initial investigation of mechanical alloying parameters used a Svegvari Type 01STD attritor mill (purchased from Union Process Inc., Akron, Ohio), which has a capacity of 0.75 litres (0.26 ft^3). This mill was top-loaded (and unloaded) and was fitted with a water-cooled lid and paddle bearing. A typical charge consisted of 150 g (0.33 lb) of powder, and 1500 g (3.3 lb) of stainless steel balls (powder:ball ratio of 1:10). Prealloyed Fe_3Al (FAS) powder was used, together with reactive metal oxide powder which was obtained with an average particle size of less than 1μm. The FAS powder was obtained from Ametek, and consisted of spherical particles having a particle size range of 150 μm to 45 μm, (mesh size -100/+325). In use, the loaded and assembled mill was purged with argon for 5 min. prior to the start of milling; a continuous flow of argon was maintained during milling. At the end of a run, the lid was removed and the cooled powder exposed to the ambient laboratory air. The effect of increasing milling time was evaluated through examination of the powder size and shape by scanning electron microscopy; the extent of mechanical alloying was assessed by light microscopy of metallographically-prepared samples of the powder. The mechanical alloying process incorporates the oxide dispersoid into the alloy structure by a repetitive process of welding and smearing of the alloy powder particles onto the mill walls and the balls, followed by detachment of fragments of the powder. A layered structure is developed which contains entrapped particles of the dispersoid; with time, the layers become sufficiently fine that the alloy powder particles attain a homogeneous composition, with a uniform distribution of the dispersoid particles. Figure 7 shows the change in powder particle size as a function of milling time. The most obvious initial effect of milling is flattening of the original spherical particles into discs, which assume irregular shapes with increased milling time. Further milling results in the transformation from flattened plates to agglomerates of much smaller particles. Once the powder structure observed after 50 hours of milling is attained, further milling produces little alteration in alloy structure or actual particle size.

The milling parameters chosen for the processing of powder intended for subsequent consolidation and preparation of test specimens were 500 rpm for 48 hours. A larger Svegvari attritor mill, Type 01HD with a capacity of 1.4 litres (0.49 ft^3), was used to prepare these materials. The milling conditions were the same as those used in the smaller mill. The amount of powder per batch was increased to 300g (0.66 lb) and the larger mill is capable of running 24 hours per day.

A search was made for facilities capable of producing larger batches of mechanically-alloyed powder, of the order of several kilograms to commercial alloy-production sizes. The following possible sources were identified: INCO, Dour Metal of Belgium; PM Hochtemperatur-Metall of Germany; AEA Technology of Risley, U. K.; and CRM of Italy. INCO (Huntington, West Virginia) uses ball milling to produce Ni-based ODS-alloys only and has no current capability that could address the needs of the iron aluminide program; there was also concern about contamination of any mill that was used. INCO International (Hereford, U.K.) produces only Fe-based ODS alloys, but it also has no available mill capacity. Dour Metal has produced tubes of ODS-FeCrAl-Y_2O_3 using in-house processing that starts with ball milling. They also have made an ODS version of Fe-40 at.% Al using alumina as the dispersoid. PM Hochtemperatur-Metall uses ball milling to produce ODS-FeCrAl-Y_2O_3 on a commercial basis, but has not made tubing. AEA, Risley, U.K. has a small-capacity centrifugal mill of new design; this equipment has the potential for better processing control than conventional attritor or ball milling, but is as yet not available in a commercial size. CRM has a small-capacity ball mill, and has been involved with ODS-Fe-40Al. Arrangements currently are being made to work with both Dour Metal and PM Hochtemperatur-Metall to produce several 20 kg (44 lb) batches of ODS-Fe_3Al powder from prealloyed FAS powder made by Ametek corp. The mechanically-alloyed powder will be used by ORNL to optimize the thermomechanical processing required to produce the required grain size and structure and to measure the properties relevant to the envisioned application.

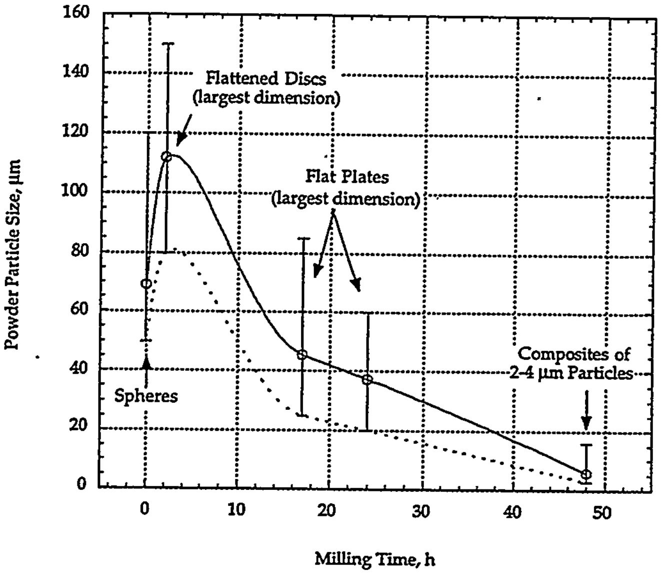

Figure 7. Plot of the average particle size of FAS-3Y alloy powder as a function of milling time.

EFFECTS OF A DISPERSION OF OXIDES ON THE HIGH-TEMPERATURE OXIDATION BEHAVIOR OF Fe_3Al

Mechanically-alloyed powders of Fe_3Al containing additions of the following reactive element oxides: Y_2O_3 (0.05, 0.1, 0.2, 0.3, 0.5 cation %), ZrO_2 (0.2 cat.%), La_2O_3 (0.05, 0.2 cat.%), Al_2O_3 (0.2 cat.%), CeO_2 (0.2 cat.%), Nd_2O_3 (0.2 cat. %), and Yb_2O_3 (0.2 cat. %) were made at ORNL using nitrogen-atomized prealloyed FAS powder in the Svegvari 01HD mill. These powders were canned in mild steel, and extruded at 1050°C (1922°F) with a reduction ratio of 12:1 to produce rods approximately 25 mm (1.0 in.) in diameter. After decanning, disc-shaped specimens were cut from these rods and subjected to oxidation testing with no further heat treatment, that is, with a relatively small alloy grain size. The specimen surfaces were polished with 0.3 µm (12 x 10^{-6} in.) alumina and washed before exposure. The details of the test procedures and some of the cyclic oxidation results are presented elsewhere [22]. Figures 8 and 9 summarize the kinetics of isothermal oxidation in air, and cyclic oxidation in oxygen, respectively, both at 1200°C (2192°F), for the FAS alloy with and without a dispersion of Y_2O_3. Ignoring the initial rapid oxidation of the undoped alloy during the first 4 hours of isothermal exposure, the oxidation rates of the two alloys at longer times appear quite similar; both alloys exhibited oxidation rates that are slightly slower than parabolic, suggesting that the oxide scales become more protective with time. In the cyclic oxidation test, the weight gain of the ODS alloy was very similar to that in the isothermal test up to approximately 16 hours (and obviously slower than that of the undoped alloy), after which it

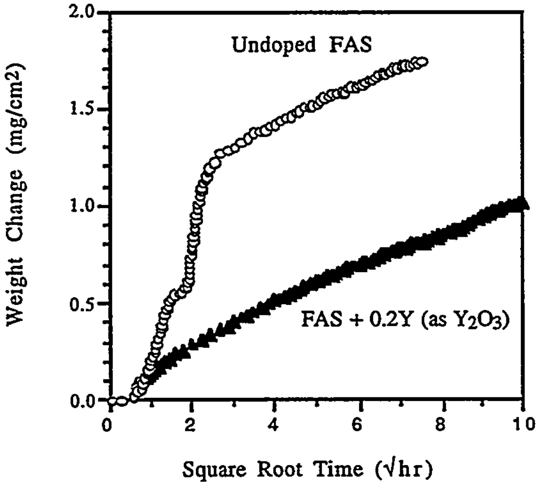

Figure 8. Comparison of the isothermal oxidation kinetics of conventionally-produced and and ODS-FAS (FAS-3Y); 1200°C in oxygen.

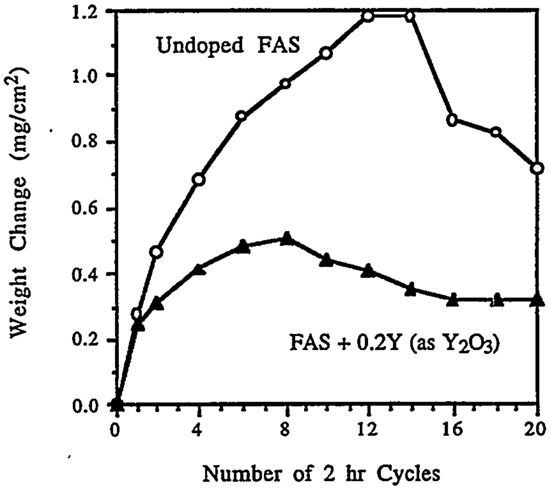

Figure 9. Comparison of the cyclic oxidation kinetics of conventionally-produced ODS-versions of Alloy FAS (FAS-3Y); 1200°C in air.

apparently suffered some degree of scale spallation. The reason for the increased weight gain of the undoped alloy in this test was because it suffered from scale spallation at the end of each cycle. The areas over which spallation occurred were extremely small and, since the spalled scale did not fully detach, a net increase in weight was measured up to the 14th cycle, or 28 hours, after which actual scale loss apparently occurred.

Figures 10 and 11 compare the isothermal and cyclic oxidation behavior of the FAS-3Y alloy with a commercially-available ODS-FeCrAl-Y_2O_3 alloy, MA956 (see Table 1) at 1200°C (2192°F) in air, and in oxygen, respectively. The kinetics of isothermal oxidation to 100 hours appear essentially the same, as might be expected for alloys that are intended to form a protective alumina scale. Under isothermal conditions, the rate of consumption of aluminum to form the protective scale would be very similar for the two alloys. In the cyclic oxidation test, the weight gain of the MA956 after 40 hours was almost the same as that measured in the isothermal test, indicating no scale spallation. As noted above, the weight gains measured for the FAS-3Y indicated some scale spallation. This is a surprising result, since a dispersion of a reactive element oxide with the appropriate particle size and distribution generally has been found to improve the overall scale adherence on alumina-forming alloys. Such spallation would obviously increase the rate of depletion of the aluminum reservoir of the FAS-3Y alloy. Although this reservoir is much larger than that in alloy MA956, the rate of spallation must be minimized to maintain the potential service lifetime advantage of FAS-3Y[22].

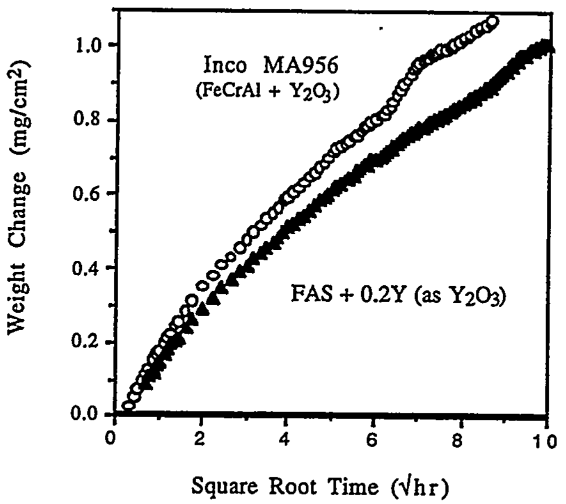

Figure 10. Comparison of the isothermal oxidation kinetics of ODS-FAS (FAS-3Y) with a commercial ODS-FeCrAl-Y_2O_3; 1200°C in air.

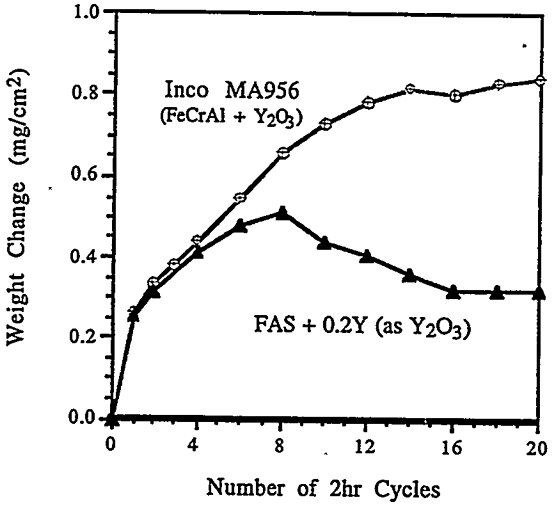

Figure 11. Comparison of cyclic oxidation kinetics of ODS-FAS (FAS-3Y) with a commercial ODS-FeCrAl-Y_2O_3; 1200°C in oxygen.

There are several possible reasons for the difference in scale spallation behavior between the two alloy types, ranging from inhomogeneity in FAS-3Y to a fundamental difference in the functioning of the reactive element effect in Fe_3Al compared to FeCrAl-Y_2O_3. The possibility that there are inherent differences in scale spallation behavior between FeCrAl-based and iron aluminide-based alloys[20] and the effects of different types and levels of reactive element oxides on the oxidation behavior of Fe_3Al are the subject of ongoing research.

SUMMARY AND CONCLUSIONS

Heat exchangers for cycles which require a working fluid to be heated to temperatures of 1100-1200°C (2012-2192°F) provide a potential application in which the exceptional high-temperature oxidation and sulfidation resistance of iron aluminides can be exploited. The alternative materials choices for such an application are ODS-FeCrAl-based alloys and ceramics. An ODS-version of Fe_3Al has the obvious advantage over ceramics that it has metallic characteristics, and is expected to exhibit a significantly longer service life than ODS-FeCrAl alloys. Creep tests with a non-optimized ODS-Fe_3Al indicated significantly improved strength compared to non-ODS iron aluminides, but lower creep resistance compared to a commercial ODS-FeCrAl alloy. The isothermal oxidation rate of the ODS-Fe_3Al was essentially the same as that of a commercial ODS-FeCrAl alloy at 1200°C (2192°F), but there was evidence of inferior resistance to cyclic oxidation. The main issues to be resolved are the ability of optimized ODS processing of Fe_3Al to achieve an equivalent improvement in high-temperature creep strength to that found with ODS-FeCrAl alloys and a method for improving the resistance to scale spallation of Fe_3Al.

ACKNOWLEDGMENTS

The authors thank colleagues at ORNL: V. K. Sikka, K. S. Blakely, J. L. Wright, M. Howell, J. R. DiSteffano, and P. F. Tortorelli for their contributions and invaluable discussions. This research was sponsored by the Fossil Energy Advanced Research and Technology Development (AR&TD) Materials Program, U. S. Department of Energy, under contract DE-AC05-84OR21400 with Martin Marietta Energy Systems, Inc. B. A. Pint is supported by the U. S. Department of Energy's Distinguished Postdoctoral Research Program administered by the Oak Ridge Institute for Science and Education.

REFERENCES

1. F. Starr, A. R. White, and B. Kazimierzak, pp. 1393-1412 in *Materials for Advanced Power Engineering*, Proc. 5th COST 501 Conf., Liege, Belgium, D. Coutsouradis, et al., eds., Kluwer Academic Pub., Dordrecht (1994).
2. D. Sporer, and O. Lange, ibid, pp. 1469-1488.
3. J. Beckers-Lecomte, D. Coutsouradis, and B. Kazimierzak, ibid, pp. 1489-1498.

4. H. Cama, and T. A. Hughes, ibid, pp. 1497-1506.
5. D. M. Jaeger, and A. R. Jones, ibid, pp. 1507-1514.
6. D. M. Jaeger, and A. R. Jones, ibid, pp. 1515-1522.
7. B. Dubiel, W, Osuch, M. Wrobel, A. Czyrska-Filemonowicz, and P. J. Ennis, ibid, pp. 1523-1532.
8. W. J. Quadakkers, K. Bongartz, F. Stubbier, and H. Schuster, ibid, pp. 1533-1542.
9. J. P. Banks, D. D. Gohil, H. E. Evans, D. J. Hall, and S. R. J. Saunders, ibid, pp. 1543-1552.
10. J. Bennett, R. Perkins, J. B. Price, and F. Starr, pp. 1553-1562.
11. G. P. De Gaudenzi, F. Umberti, F. Bregani, and G. P. Toledo, ibid, pp. 1563-1572.
12. R. C. Hurst, M. Rees, and J. D. Parker, ibid, pp. 1573-1582.
13. W. Hessenbruch, *Metals and Alloys for Use at High Temperatures, Part 1, Non-Scaling Alloys*, J. Springer, Berlin (1940).
14. I. I. Kornilov, Profigrafkniga, Moscow (1945), cited by Setterlund and Prescott, 1961.
15. C. S. Wukusic, *The Physical Metallurgy and Oxidation Behavior of Fe-Cr-Al-Y Alloys*, Report No. GEMP-414 by General Electric Nuclear Energy Div. on USAEC Contract No. AT (40-1)-2847 (1966).
16. C. Sykes and J. W. Bampfylde, JISI, 130 (II), 389 (1934).
17. R. B. Setterlund and G. R. Prescott, Corrosion 17, 277t-282t (1961).
18. J. F. Nachman and W. J. Buehler, *The Fabrication and Properties of 16-ALFENOL (Fe_3Al)—A Non-Strategic Aluminum-Iron Alloy*, U. S. Naval Ordnance Lab. Report No. 2819, (April, 1953).
19. J. F. Nachman and W. J. Buehler, *Thermenol (Fe_3Al-3Mo), A Non-Strategic Aluminum-Base Alloy for High-Temperature Service*, U. S. Naval Ordnance Lab. Report No. 3700, (June 1954).
20. See, for example, J. H. DeVan, P. F. Tortorelli, and M. J. Bennett, pp. 309-320 in *Eighth Annual Conf. on Fossil Energy Materials*, N. C. Cole and R. R. Judkins (comp.), CONF-9405143, U. S. Department of Energy, August 1994.
21. A. U. Seybolt, Trans. ASM, 59, 861-875 (1966).
22. P. F. Tortorelli, J. H. DeVan, B. A. Pint, and I. G. Wright, paper presented at the *Ninth Annual Conference on Fossil Materials*, Oak Ridge, TN, May 1995.

EFFECTS OF COMPOSITION AND HEAT TREATMENT AT 1150°C ON CREEP-RUPTURE PROPERTIES OF Fe_3Al-BASED ALLOYS

C. G. McKamey, P. J. Maziasz, and Y. Marrero-Santos

Metals and Ceramics Division
Oak Ridge National Laboratory
Oak Ridge, TN 37831-6115

ABSTRACT

The effects of composition and heat treatment at 1150°C on the creep-rupture properties of Fe_3Al-based alloys were studied. Tests of alloy FA-180 (Fe-28Al-5Cr-0.5Nb-0.8Mo-0.025Zr-0.05C-0.005B, at.%) with this heat treatment were performed in air using various test temperatures and stresses in order to obtain creep activation energies and constants. An activation energy for creep of approximately 150 kcal/mole was determined, a value which is approximately twice that obtained earlier for the binary alloy heat treated at 750°C. Tests were also conducted on alloys containing various combinations of Cr, Mo, Nb, Zr, C, and B in order to better understand the effect of composition on the improved creep resistance with heat treating at 1150°C. The results suggest an interaction of Mo with Zr and Nb to produce increased creep life.

INTRODUCTION

Past studies have shown that binary Fe_3Al possesses low creep-rupture strength compared to many other alloys, with creep-rupture lives of less than 5 h being reported for tests conducted at 593°C and 207 MPa (ref. 1). The combination of poor creep resistance and low room-temperature tensile ductility due to a susceptibility to environmentally-induced dynamic hydrogen embrittlement[2,3] has limited use of these alloys for structural applications, despite their excellent corrosion properties.[4] Improvements in room temperature tensile ductility have been realized mainly through alloying effects, changes in thermomechanical processing to control microstructure, and by control of the specimen's surface condition.[3,5] Ductilities of 10-20% and tensile yield strengths as high as 500 MPa have been reported.[6,7] In terms of creep-rupture strength, small additions of Mo, Nb, and Zr have produced significant improvements, but at the expense of weldability and room-temperature tensile ductility.[1,8-11] Recently an alloy containing these additions, designated FA-180, was shown to exhibit a creep-rupture life of over 2000 h at 593°C and 207 MPa after a heat treatment of 1 h at 1150°C.[12,13] The increased strength was attributed to the dissolution of coarse particles and reprecipitation of finer Nb-, Mo-, and Zr-based precipitates which strengthened grain boundaries and pinned dislocations.[12-15] This study presents the results of creep-rupture tests at various test temperatures and stresses and discusses the results as part of our effort to understand the strengthening mechanisms involved with heat treatment at 1150°C. Creep-rupture tests of several different compositions of Fe_3Al-based alloys were also conducted in order to better understand the composition dependence of the 1150°C heat treatment.

EXPERIMENTAL PROCEDURES

Alloys used in this study were prepared by arc-melting and drop-casting into a chilled copper mold. Fabrication to 0.8-mm-thick sheet was accomplished by hot-rolling, beginning at 1000°C and finishing at 600-650°C. After a stress relief anneal of 1 h at 700°C, flat tensile specimens (0.8 x 3.18 x 12.7 mm) were mechanically punched from the rolled sheet. Before testing, the specimens were further annealed in air for 1 h at 1150°C and air cooled. Creep-rupture tests were performed in air at temperatures between 500 and 775°C and at stresses of 69-434 MPa (10-63 ksi). Minimum creep rates (MCR) were measured as the slope of the linear portion of the test curve. The data were plotted to a power-law equation in order to obtain creep exponents and activation energies. Optical metallography and scanning electron microscopy (SEM) were used to study the microstructures and fracture modes.

RESULTS AND DISCUSSION

Effect of Heat Treatment at 1150°C on Creep of Alloy FA-180

Tables I and II list the results of creep-rupture tests conducted as a function of test temperature and stress, respectively. The results of tests at temperatures between 593 and 700°C showed that, under a stress of 207 MPa, this alloy had good creep resistance to a temperature of 650°C, but the creep-rupture life decreased dramatically at 675°C. Other data in Tables I and II indicate that with a lower applied stress this alloy could be used at temperatures higher than 650°C. For example, using a stress of 69 MPa, a creep-rupture life of over 500 h was attained at 675°C and almost 200 h at 700°C (Table I). All of the fractured specimens showed a ductile failure mode in which creep voids were observed to have coalesced at grain boundaries and triple points.

Table I. Creep-rupture test results for tests conducted at constant stress

Test #	Stress (MPa)	Temperature (°C)	Rupture Life (h)	Elongation (%)	MCR[a] (%/h)
404/405	207	700	0.6	26.2	13.6
407/431		675	0.8	27.0	20.8
410		650	1059.0	11.0	0.002
411		593	1959.2	9.7	0.003
418/420	69	775	5.1	72.6	4.0
417/419		750	12.5	72.2	1.6
421/422		725	54.5	52.2	0.4
415/416		700	192.1	60.4	0.03
412		675	591.0	45.0	0.002

[a]MCR = minimum creep rate measured in the linear portion of the creep curve.

Table II. Creep-rupture test results for tests conducted at constant temperature

Test #	Temperature (°C)	Stress (MPa)	Rupture Life (h)	Elongation (%)	MCR[a] (%/h)
407/431	675	207	0.8	27.0	20.8
425/430		172	14.2	27.0	1.4
408/413/414		138	52.2	29.0	0.1
427		103	252.4	24.8	0.01
412		69	591.0	45.0	0.002
484	500	434	8.4	29.6	2.0
483		414	14.8	30.8	1.9
429		379	28.2		0.2
476		365			0.2
426		345	54.0	25.1	0.3
484		328			0.02
428		310	27.9		0.05

[a]MCR = minimum creep rate measured in the linear portion of the creep curve.

If one assumes that the mechanisms of dislocation creep in intermetallic alloys do not differ from those in conventional alloys,[16-19] then the creep data can be fitted to a power-law creep equation of the form

$$\dot{\varepsilon}=A\sigma^{n}(e^{-Q/RT}) ,$$

where $\dot{\varepsilon}$ is the minimum creep rate (MCR) , A is a constant, σ is the test stress, n is the creep exponent, Q is the activation energy for creep, T is the temperature in Kelvin (K) and R is the universal gas constant with a value of 1.987 cal/mol/°C. By rearranging this equation and inserting the data for constant stress or constant temperature tests, the activation energy for creep (Q) and the creep exponent (n) were obtained (see Figs. 1 and 2). The average activation energy was determined to be approximately 150 kcal/mole which indicates a much stronger temperature dependence of the creep rate for this alloy compared to binary Fe-28Al or the ternary alloys containing additions of only Mo or Nb/Zr (~80 kcal/mol).[1,20] The binary alloy has been shown to have very poor creep resistance under the test conditions used in the current study[1] and a heat treatment at 1150°C produced absolutely no improvement,[21] as was expected for a binary alloy with no precipitate formers. A creep exponent of 7-12 was determined from constant-temperature tests at 500 and 675°C, numbers which suggest that

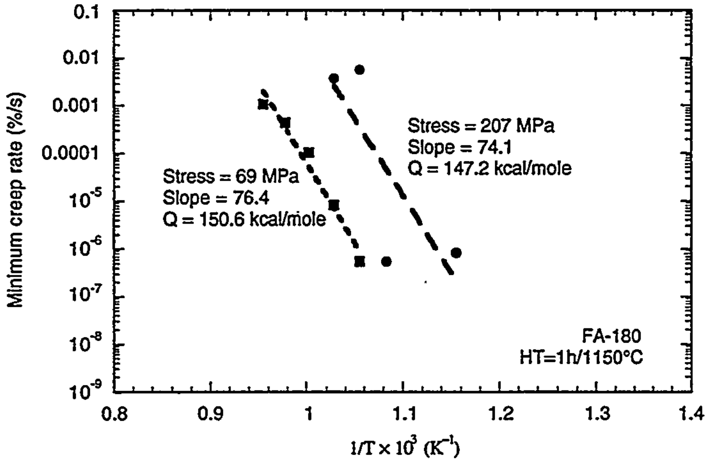

Fig. 1. Minimum creep rate versus temperature for FA-180. The slope represents the activation energy for creep.

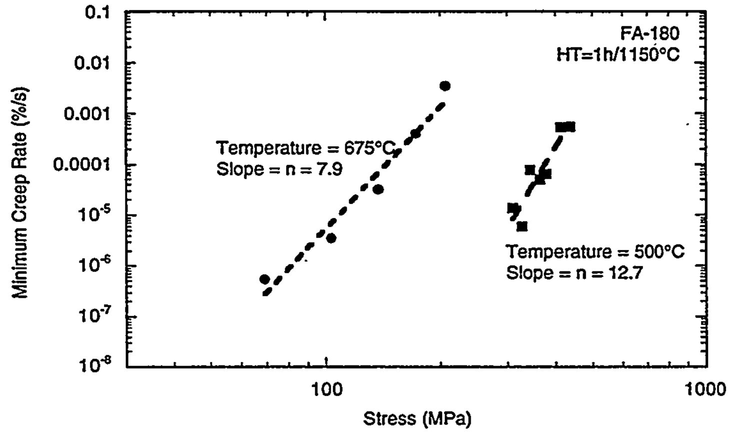

Fig. 2. Minimum creep rate versus stress for FA-180. The slope equals the creep exponent n.

the increased creep strength with the 1150°C heat treatment probably involves particle strengthening.[16-18] This was substantiated by the analytical electron microscopy (AEM) results reported earlier.[12,13] In this study, no dependence of the creep exponent on the test stress, as was reported earlier for binary and ternary alloys,[1] was observed.

Creep-Rupture of Various Fe_3Al Compositions Heat Treated at 1150°C

In order to gain an understanding of the relationship between composition and the improvement in creep-rupture life with a 1-h heat treatment at 1150°C, several alloys containing various amounts and combinations of Cr, Nb, Mo, Zr, B, and C were included in this study. Some of those compositions and the results of creep tests conducted at 593°C with a stress of 207 MPa are listed in Table III. The general conclusion from these results is that, while the addition of Nb, Zr, or Mo, alone or in combination with Cr, B, or C, do not provide significant strengthening, the proper combination of Nb, Zr, and Mo does result in creep-rupture lives of over 2000 h. Figures 3 and 4 show that the best creep properties were attained in alloys containing at least 0.5 at. % Nb and 0.8 at.% Mo, with a small amount of zirconium. The particular level of zirconium needed is difficult to ascertain from these results, but appears to be low (on the order of 0.1 at.% or less). Other studies have shown that approximately 0.1% Zr will be required to promote scale adhesion for protection against corrosion in harsh environments.[4] But the more zirconium added, the more embrittle will be the alloy.[14] Therefore, the level of zirconium will have to be carefully controlled. Indications are that the zirconium interacts with molybdenum to produce its contribution to the strengthening. These results support previous analytical electron microscopy results which indicated that Zr, Mo, and Nb-based precipitates, formed during cooling from 1150°C, are the strengthening agents in these alloys.[12,13,21] These are also the same additives which were shown to produce some improvement in creep life after a heat treatment at 750°C.[9,14]

The results shown in Table III for alloys FA-92, FA-88, FA-128, and FA-129 indicate that the presence of large amounts of carbon should be avoided if creep resistance is important for the intended application. The effect of boron on creep strength is less obvious, but suggestions are that large amounts of boron (on the order of 0.2 at.%; see results for FA-122 versus FA-126 in Table III) can result in reduced creep life. The amount of reduction may actually depend on which other elements are present.

CONCLUSIONS

In an earlier study, the creep-rupture strength of Fe_3Al-based alloy FA-180 (Fe-28Al-5Cr-0.5Nb-0.8Mo-0.025Zr-0.05C-0.005B, at.%) was shown to be improved significantly by heat treating for 1 h at 1150°C. This strengthening was attributed to the formation of fine

Table III. Creep-rupture test results versus composition after heat treatment for 1 h at 1150°C (all tests were conducted at 593°C and 207 MPa)

Alloy	Composition (at.%)	Life (h)	Elongation (%)	MCR (%/h)
FA-61C	Fe-28Al	0.2	6	45
FA-124	-5Cr-.05B	3	24	4.2
FA-128B	-5Cr-.5Nb-.05B	35	47	0.6
FA-129	-5Cr-.5Nb-.2C	8	45	1.2
FA-122B	-5Cr-.1Zr-.05B	149	17	0.0045
FA-126	-5Cr-.1Zr-.2B	4	54	5.8
FA-62B	-2Mo	91	19	0.1
FA-73	-2Mo-.05B	19	25	0.5
FA-74	-2Mo-.1B	24	16	0.4
FA-75	-2Mo-.2B	77	26	0.1
FA-114	-2Mo-.05Zr-.05B	2541	9.5	0.0005
FA-92	-2Mo-.1Zr-.2B	1022	25	0.0015
FA-88	-2Mo-.1Zr-.2C	194	52	0.05
FA-166	-5Cr-1Mo-.5Nb-.02Zr	696	12	0.002
FA-130	-5Cr-.5Mo-.5Nb-.1Zr-.05B	2203	16	0.0009
FA-133L	-5Cr-.5Mo-.5Nb-.1Zr-.2B	1534	28	0.002
FA-169	-5Cr-.25Mo-.5Nb-.025Zr-.05C	34	49	0.6
FA-174	-5Cr-.4Mo-.2Nb-.025Zr-.05C	8	28	1.8
FA-175	-5Cr-.4Mo-.025Zr-.05C	15	27	1.3
FA-178	-5Cr-.4Mo-.025Zr-.05C-.005B	17	34	0.9
FA-176	-5Cr-.4Mo-.025Zr-.5Nb-.05C-.005B	56	26	0.1
FA-170	-5Cr-.4Mo-.025Zr-.5Nb-.05C	51	41	0.5
FA-177	-5Cr-.4Mo-.025Zr-.2Nb-.05C-.005B	21	41	1.0
FA-179	-5Cr-.6Mo-.025Zr-.5Nb-.05C-.005B	48	31	0.3
FA-180	-5Cr-.8Mo-.025Zr-.5Nb-.05C-.005B	1924	11	0.0006
FA-183	-5Cr-.8Mo-.025Zr-.3Nb-.05C-.005B	2	22	5.9
FA-184	-5Cr-.8Mo-.025Zr-.1Nb-.05C-.005B	24	30	0.7

matrix and grain boundary precipitates. In this study, the activation energy for creep in alloy FA-180 was determined to be approximately 150 kcal/mole which is twice that determined earlier for binary Fe_3Al. Creep exponents of 7-12 were determined, consistent with a precipitation-strengthening mechanism.

Creep-rupture tests of many alloys containing different compositions of Mo, Zr, Nb, Cr, B, and C support the earlier results of analytical electron microscopy that indicated that the strengthening in these alloys is produced by the presence of fine Zr(Nb,Mo)-based precipitates. The role of boron is still unclear, but the presence of carbon in amounts of 0.1 at.% or more was found to decrease creep strength significantly.

ACKNOWLEDGEMENTS

This research was sponsored by the U.S. Department of Energy, Office of Fossil Energy, Advanced Research and Technology Development Materials Program and by the

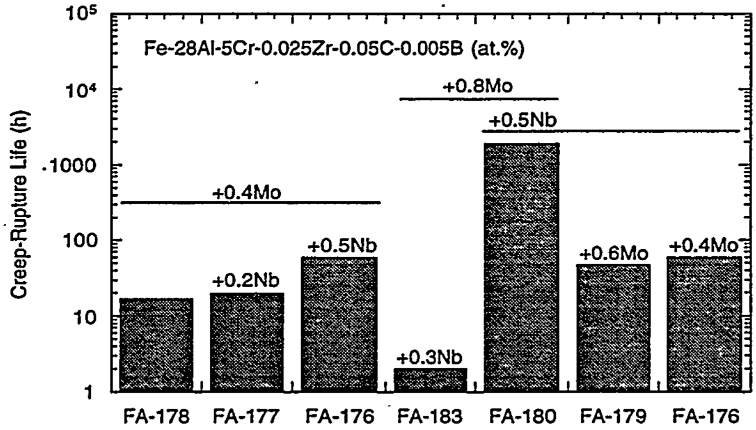

Fig. 3. Effect of addition of niobium and molybenum on creep-rupture life of a Fe_3Al-based alloy tested at 593°C and 207 MPa.

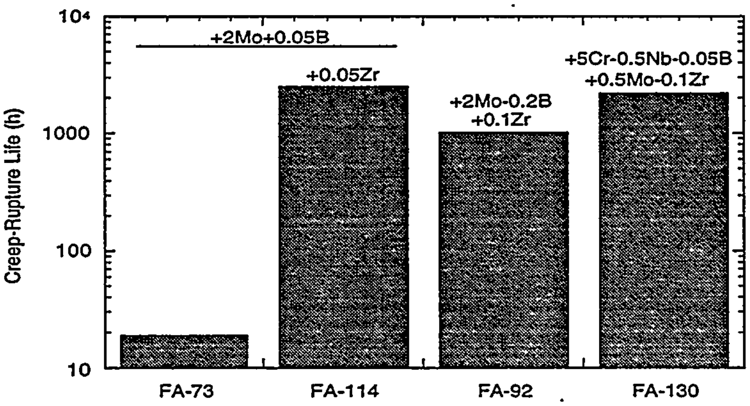

Fig. 4. Effect of addition of zirconium on creep-rupture life of molybdenum-containing Fe_3Al alloys tested at 593°C and 207 MPa.

Assistant Secretary for Energy Efficiency and Renewable Energy, Office for Industrial Technologies, Advanced Industrial Materials Program, under contract DE-AC05-84OR21400 with Martin Marietta Energy Systems, Inc., and by the American Chemical Society's Project SEED (Summer Educational Experience for the Disadvantaged) program at the Oak Ridge National Laboratory managed by the Martin Marietta Energy Systems, Inc.

REFERENCES

1. C. G. McKamey, P. J. Maziasz, and J. W. Jones, J. Mater. Res. **7**(8), 2089 (1992).
2. C. T. Liu, C. G. McKamey, and E. H. Lee, Scripta Metall. Mater. **24**(2), 385 (1990).
3. C. T. Liu and C. G. McKamey, in High Temperature Aluminides and Intermetallics, edited by S. H. Whang, C. T. Liu, D. P. Pope, and J. 0. Stiegler, The Metallurgical Society, Warrendale, PA: 1990, pp. 133-151.
4. P. F. Tortorelli and J. H. DeVan, in Processing, Properties, and Applications of Iron Aluminides, edited by J. H. Schneibel and M. A. Crimp, TMS, Warrendale, PA, 1994, pp. 257-70.
5. C. G. McKamey and C. T. Liu, in Proceedings of ADVMAT/91, First International Symposium on Environmental Effects on Advanced Materials, edited by R. D. Kane, NACE, Houston, TX, 1992, paper no. 17-1.
6. V. K. Sikka, SAMPE Quart. **22**(4), 2 (1991).
7. V. K. Sikka, S. Viswanathan, and C. G. McKamey, Structural Intermetallics, edited by R. Darolia, J. J. Lewandowski, C. T. Liu, P. L. Martin, D. B. Miracle, and M. V. Nathal, The Metallurgical Society, Warrendale, PA, 1993, pp. 483-91.
8. C. G. McKamey, J. H. DeVan, P. F. Tortorelli, and V. K. Sikka, J. Mater. Res. **6**(8), 1779 (1991).
9. P. J. Maziasz and C. G. McKamey, Mater. Sci. & Eng., **A152**, 322 (1992).
10. D. M. Dimiduk, et al., Acta Metall. **36**, 2947 (1988).
11. D. G. Morris, M. Nazmy, and C. Noseda, Scripta Metall. Mater. **31**, 173 (1994).
12. C. G. McKamey and P. J. Maziasz, in Processing, Properties, and Applications of Iron Aluminides, edited by J. H. Schneibel and M. A. Crimp, TMS, Warrendale, PA, 1994, pp. 147-58.
13. C. G. McKamey and P. J. Maziasz, Proceedings of Eighth Annual Conference on Fossil Energy Materials, ORNL/FMP-94/1, Oak Ridge National Laboratory, Oak Ridge, TN, August 1994, pp. 169-83.
14. C. G. McKamey, P. J. Maziasz, G. M. Goodwin, and T. Zacharia, Mater. Sci. & Eng. **A174**, 59 (1994).
15. C. G. McKamey, Y. Marrero-Santos, and P. J. Maziasz, in High Temperature Ordered Intermetallic Alloys VI, edited by J. A. Horton, I. Baker, S. Hanada, R. D. Noebe, and D. S. Schwartz, Mater. Res. Soc. Symp. Proc. **364**, Pittsburgh, PA, 1995, pp. 249-54.
16. F. Garofalo, Fundamentals of Creep and Creep-Rupture in Metals, The Macmillan Co., New York, 1965.
17. O. D. Sherby and P. M. Burke, Prog. Mater. Sci. **13**, 325 (1967).
18. N. S. Stoloff and R. G. Davies, Prog. Mater. Sci. **13**, 1 (1966).
19. I. Jung, M. Rudy, and G. Sauthoff, in High Temperature Ordered Intermetallic Alloys II, edited by N. S. Stoloff, C. C. Koch, C. T. Liu, and O. Izumi, Mater. Res. Soc. Symp. Proc. **81**, Pittsburgh, PA, 1987, pp. 263-274.
20. A. Lawley, J. A. Coll, and R. W. Cahn, TMS AIME **218**, 166 (1960).
21. C. G. McKamey, unpublished results, 1994.

ENVIRONMENTAL EMBRITTLEMENT OF IRON ALUMINIDES UNDER CYCLIC LOADING CONDITIONS

A. Castagna, D. A. Alven and N. S. Stoloff

Rensselaer Polytechnic Institute
Troy, NY 12180-3590

ABSTRACT

The tensile and fatigue crack growth behavior in air in hydrogen and in oxygen of an Fe-Al-Cr-Zr alloy is described. The results are compared to data for FA-129. A detailed analysis of frequency effects on fatigue crack growth rates of FA-129, tested in the B2 condition, shows that dislocation transport of hydrogen from the surface is the rate limiting step in fatigue crack growth.

INTRODUCTION

Iron aluminides are currently being studied for use in applications where low cost, relatively low weight, moderate strength at temperatures up to 500°C, and excellent corrosion resistance are desired. Binary iron aluminides do not possess high ductility at room temperature in air; however, iron aluminides have demonstrated ductility of 12%-16% when tested in vacuum or gaseous oxygen environments.[1-4] This indicates that Fe_3Al is an inherently ductile material and an environmental interaction causes the low ductility in air.

The purpose of this research was to examine the effects of environment on the mechanical properties of two Fe_3Al base intermetallics. In particular, fatigue crack growth resistance and tensile behavior were examined in various environments, and the resulting data used to gain insight into the role of hydrogen in embrittlement of the iron-aluminum alloys.

EXPERIMENTAL PROCEDURE

Alloy Composition and Heat Treatment

Two alloys were examined in this study, an Fe-28%Al alloy designated FA-129, and an Fe-Al-Cr-Zr-C alloy, see Table 1. The alloys can exist in the B2 or DO_3 ordered state, depending on the temperature from which each is quenched. Both alloys were fabricated at the Oak Ridge National Laboratory (ORNL) by vacuum induction melting, extrusion to a 2.54 cm thickness, and either hot or warm rolling to the final thickness of near 5mm.

The annealing parameters for both alloys consisted of a 700°C anneal for 1 hour with a mineral oil quench, which was then repeated. This resulted in a partially ordered B2 type superlattice.

Tensile tests on Fa-129 have previously been described (3,4). The strain rate for tensile tests on Fe-Al-Cr-Zr reported here was 3×10^{-4} s^{-1}. All specimens were cyclindrical; some were notched (1.0mm deep, 0.689mm radius). The stress concentration factor was 3.9. Tests were conducted in air, 1 atm O_2 and 1 atm H_2 gas.

TABLE 1

Compositions of Iron Aluminides

a%

	Fe	Al	Cr	Mo	Nb	Zr	C
FA-129	66.2	28.1	5.0	--	0.5	--	0.2
Fe-Al-Cr-Zr-C	bal	28	5.0	--	--	0.5	0.05

Compact tension specimens were used in all fatigue tests and were cut such that the crack propagation direction would be perpendicular to the rolling direction. The Zr-containing alloy was 34.9mm x 33.5mm x 4.3mm thick, while FA-129 specimens were 25mm x 24mm x 5.1mm thick. Crack length was monitored via the d.c. potential drop method. Calibration curves were created relating crack length to potential drop by optically measuring the crack length with a calibrated traveling microscope. Tests were conducted in the three environments used for tensile experiments. The R-ratio was 0.5 and the frequency was 20Hz unless otherwise noted.

EXPERIMENTAL RESULTS

Tensile Experiments

Tensile stress strain curves for the Fe-Al-Cr-Zr alloy are shown in Fig. 1 and data from these tests are summarized in Table 2. Note that elongations and % reduction in area are similar in air and in oxygen, but are much reduced in 1 atom H_2 gas. Notch sensitivity ratios of 0.74 were noted in both air and oxygen, but could not be measured in H_2 gas.

Fatigue Crack Growth Experiments

Fatigue crack growth behavior of the Fe-Al-Cr-Zr alloy is summarized in Fig. 2 and Table 3. Note that oxygen again provides the lowest crack growth rates. However, in all environments, the slope m in the Paris crack growth equation:

$$\left(\frac{da}{dN}\right)=C\Delta K^{m} \qquad \text{Eq. (1)}$$

is much lower than for FA-129, and thresholds are higher.(3,4) A comparison of the behavior of Fa-129, and the disordered alloy FAP-Y Fe-Al-Zr-C is shown in Fig. 3.

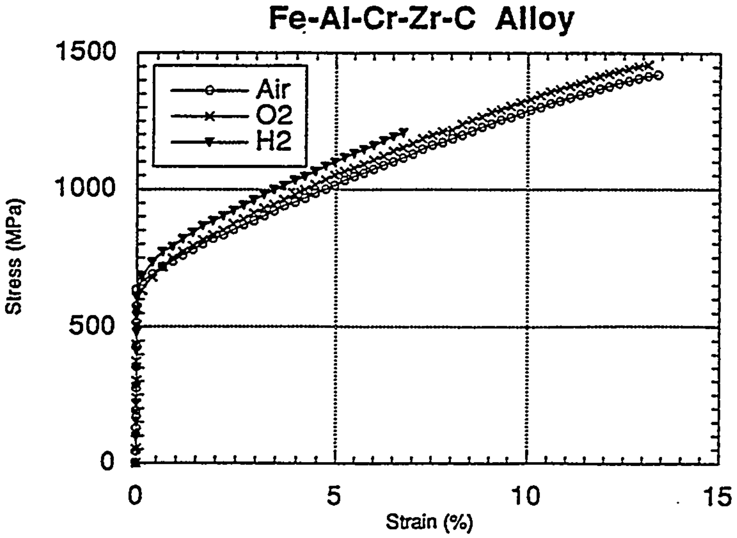

Fig. 1 Stress Strain Curves for Fe-Al-Cr-Zr, 25°C.

TABLE 2

Summary of Tensile Data for Fe-Al-Cr-Zr-C

	Ductility	RA	YS	UTS	UTS w/notch	NSR
	%	%	MPa	MPa	MPa	
Air	13.8	11.6	686	1460	1076	0.74
H_2	6.1	6.3	678	1197	-	-
O_2*	13.1	13.0	682	1456	1081	0.74

*Average of two tests

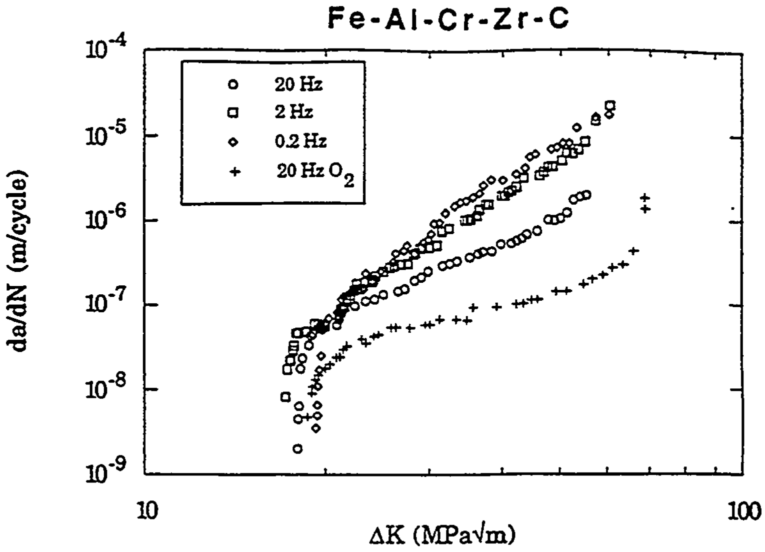

Fig.2 Effects of Environment on Fatigue Crack Growth Behavior of Fe-Al-Cr-Zr

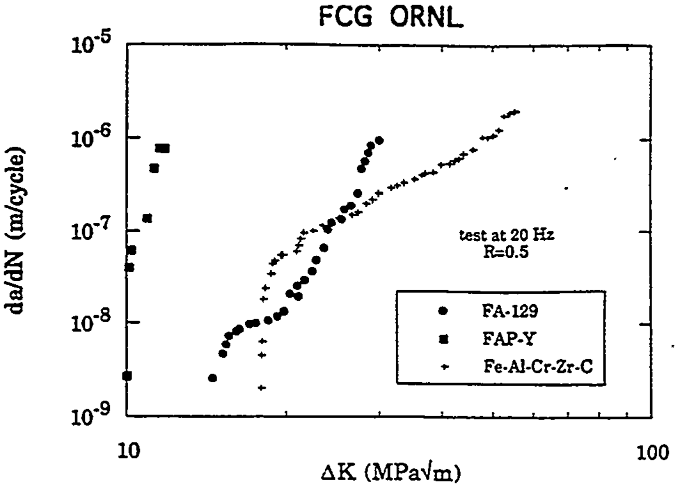

Fig. 3 Crack Growth Rates of Three Fe-Al Alloys

TABLE 3

Results of Fe-Al-Cr-Zr-C Crack Growth Experiments

Test	m	ΔK_{th} (MPa$\sqrt{m}$)	ΔK_c(MPa$\sqrt{m}$)
20 Hz in Air	3.0	18.0	55.0
2 Hz in Air	4.4	17.0	60.3
0.2 Hz in Air	5.6	19.2	64.3
20 Hz in O_2	2.5	18.6	68.7

Effect of Frequency on Fatigue Crack Growth of Fa-129

The da/dN vs. ΔK curves for B2 ordered FA-129 fatigued at frequencies of 20Hz, 2Hz, 0.2Hz, and 0.08Hz in air at 25°C are shown in Fig. 4. Also shown are data for the test at 20Hz in oxygen, which is considered to be inert. The effect of frequency on the FCG resistance was not examined in the oxygen environment. However, little or no effect is expected as oxygen has been shown to yield at least as high ductilities as a high-vacuum environment. As seen in Fig. 4, lower frequencies enhance crack growth rates at higher stress intensities. Frequency has a pronounced influence on the measured critical stress intensity. The highest K_c, 60MPa$\sqrt{m}$, is seen at the highest frequency of 20Hz. K_c steadily drops as frequency is decreased, to K_c = 50.4 MPa$\sqrt{m}$ at a frequency of 0.08Hz.

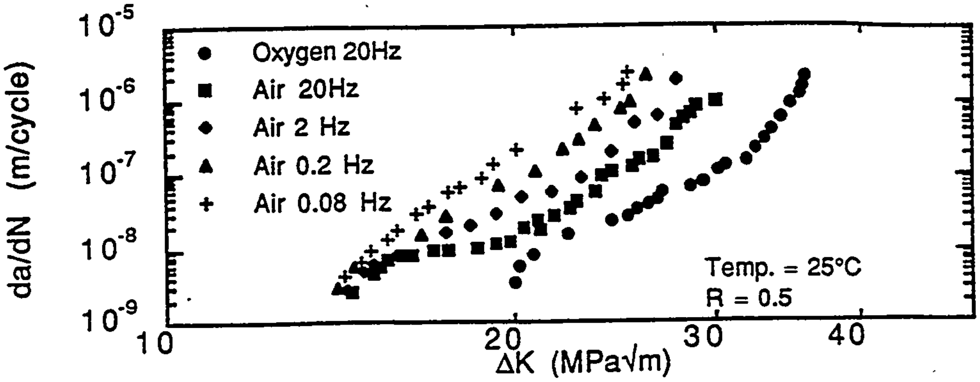

Fig. 4 Effect of Frequency on B2 Ordered FA-129 Fatigued in Air

Frequency has almost no effect on threshold stress intensity. In all tests in air ΔK_{TH} was measured between 14 and 14.5 MPa$\sqrt{m}$. The curves appear to diverge when the stress intensity range reaches about 15 MPa$\sqrt{m}$ and the growth rate reaches 5 x 10^{-9}-1 x 10^{-8} m/cycle.

Fractography

The fracture surface of B2 ordered FA-129 fatigued in hydrogen gas shows mostly cleavage facets, together with some fatigue striations.

Decreasing the test frequency of B2 ordered FA-129 tested in air made cleavage faceting more pronounced and introduced a small amount of intergranular fracture. The fracture surface at 2.0Hz showed mostly a transgranular tearing fracture mode, similar to that seen in air at 20Hz. At 0.2Hz, the fracture surface showed cleavage facets with well defined river patterns, as well as some intergranular facets. At 0.08Hz, the fracture surface displayed an even greater degree of transgranular cleavage faceting, and occasional intergranular facets.

DISCUSSION

Tensile and Fatigue Behavior of Fe-Al-Cr-Zr

The Fe-Al-Cr-Zr alloy behaves similarly to FAP-Y in that ductility is the same in air and oxygen, but is reduced in hydrogen gas(3,7). These results suggest that the small amount of Zr in this alloy inhibits moisture-induced embrittlement. In fatigue, however, oxygen clearly provides superior crack growth resistance.

Another characteristic of the Fe-Al-Cr-Zr alloy is the observation of higher threshold and critical values of stress intensity than in FA-129. This factor, combined with the low Paris exponent, shows that the crack growth resistance of the Zr-containing alloy is very high.

Frequency Dependence of Crack Growth in FA-129

The frequency effect on crack growth rate for B2 ordered FA-129 (see Fig. 4) has been analyzed following a model of McEvily and Wei (5). The crack growth rate can be expressed as a superposition of mechanical fatigue, $(da/dN)_r$, and a corrosion-fatigue interaction term $(da/dN)_{cf}$, as shown in Eq. 2.

$$\left(\frac{da}{dN}\right)=\left(\frac{da}{dN}\right)_r+\left(\frac{da}{dN}\right)_{cf} \qquad \text{Eq. (2)}$$

If the corrosion-fatigue crack growth rate $(da/dN)_{cf}$ truly reflects a synergistic combination of applied stress intensity and exposure to an embrittling environment, then this term should incorporate both a stress intensity term and some measure of the exposure to hydrogen. In the case of bulk-transport limited embrittlement the environmental term may involve the penetration depth of hydrogen ahead of the crack tip, r. Corrosion fatigue exhibiting this dependence may then be expressed by Eq. 3.

$$\left(\frac{da}{dN}\right)_{cf}=A\Delta K^m r^n \qquad \text{Eq. (3)}$$

Dislocation-assisted transport has been observed in a number of materials and is responsible for penetration of hydrogen much further than would be expected from bulk diffusion (6-9). A hydrogen atmosphere develops about a dislocation generated near the crack tip and as the dislocation travels away from the tip, it drags the hydrogen with it. The penetration distance of hydrogen ahead of the crack tip is equal to the dislocation velocity times the time available per cycle, or V/2f. One model, proposed by Tien and Richards(6), predicts the maximum possible dislocation velocity that can be achieved before the hydrogen atmosphere is stripped from the dislocation. This velocity can be used to determine the maximum penetration distance that can be accounted for by dislocation assisted transport. Tien and Richards expressed the maximum penetration, r_{max}, as

$$r_{\max}=V_{\max}t=\frac{D}{kT}\frac{E}{30b}\frac{1}{2f} \qquad \text{Eq. (4)}$$

where E is the binding energy of hydrogen to the dislocation and is approximately 0.3eV (10), k is the Boltzmann constant, t is time, and b is the Burgers vector (3Å for B2 ordered FA-129). The maximum penetration depth due to dislocation transport calculated from Eq. 4 for B2 ordered Fa-129 is tabulated in Table 4 for frequencies from 20 to 0.08 Hz. The values of r_{max} in Table 4 are several orders of magnitude larger than calculated penetration depths due to bulk diffusion, and range from 129Å to 3μm.

Eq. 3 can be rearranged to yield the following:

$$Log\left(\frac{da}{dN}\right)_{cf} = Log(A) + m\ Log(\Delta K) + n\ Log(r) \qquad \text{Eq. (5)}$$

If Eq. 3 is an accurate representation of $(da/dN)_{cf}$, then a plot of Eq. 5 at a constant ΔK should yield a straight line with the intercept given by Log(A)+m Log(ΔK) and a slope of n. These plots for ΔK=21, 23, 25, and 27 MPa√m are shown in Fig. 5. The correlation is excellent, and from a least squares curve fit the exponent n of Eq. 5 is found to be 0.52.

TABLE 4

Penetration Depth of Hydrogen Due to Dislocation Transport in B2 Ordered FA-129 at Room Temperature

Frequency (Hz)	20	2	0.2	0.08
r_{max}(m)	1.29×10^{-8}	1.29×10^{-7}	1.29×10^{-6}	3.24×10^{-6}

In order to find the values of A and m, Eq. 5 is rearranged into the following form:

$$Log\left[\frac{\left(\frac{da}{dN}\right)_{cf}}{r_{max}^{0.52}}\right] = Log(A) + m\ Log(\Delta K) \quad (6) \qquad \text{Eq. (6)}$$

Eq. 6 is plotted for all values of ΔK and frequencies in Fig. 6. The validity of Eq. 6 is clear as the $(da/dN)_{cf}$ vs. ΔK curves at various frequencies can be collapsed onto a single frequency-modified curve. A least-squares fit of the data in Fig. 6 shows that $A=3.78 \times 10^{-18}$ and m=10.31.

The excellent correlation of the fatigue data to Eqs. 3, 5 and 6 indicates that in B2 ordered FA-129 fatigued at room temperature, hydrogen moves into the lattice ahead of the crack tip by a dislocation-assisted transport mechanism.

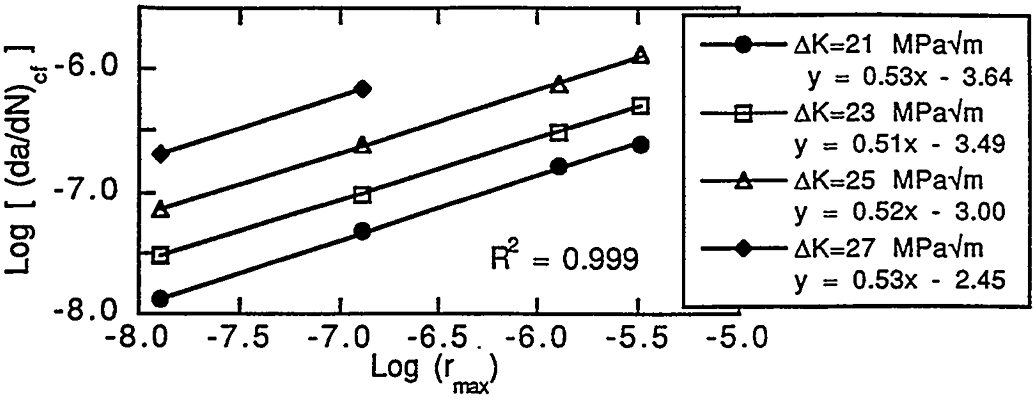

Fig. 5 Log-Log Plot of $(da/dN)_{cf}$ vs. Hydrogen Penetration Depth Due to Dislocation Transport in B2 Ordered Fa-129 Fatigued in Air at 25°C.

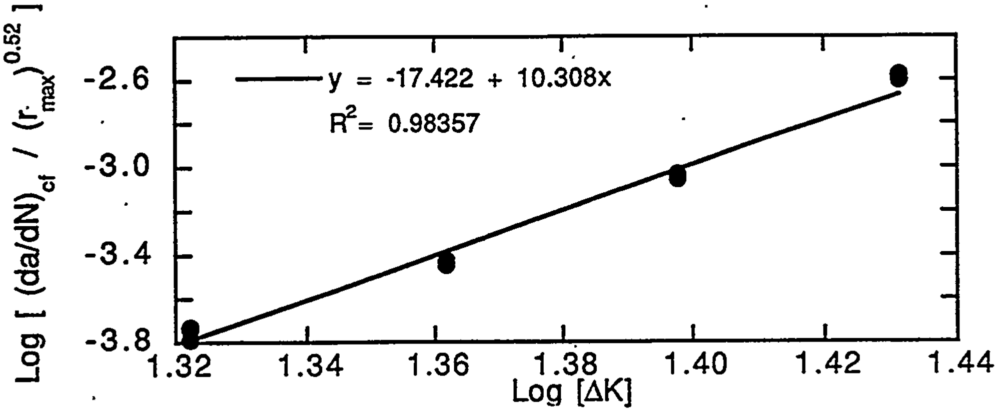

Fig. 6 Plot of Ratio of $(da/dN)_{cf}$ to Hydrogen Penetration Depth Due to Dislocation Transport vs. Applied Stress Intensity in B2 Ordered FA-129 Fatigued in Air at 25°C.

The physical meaning of the exponent n in Eq. 3 must be related to the quantity of hydrogen that dislocations carry into the plastic zone. For example, it is likely that the exponent n will scale with the quantity of hydrogen each dislocation is capable of dragging with it, or the density of dislocations capable of dragging hydrogen atoms, or both. It is, therefore, significant that the exponent n was found to be a constant with respect to frequency. Even though the degree of embrittlement increased dramatically with frequency, the exponent n was unchanged, signifying that embrittlement does little to change the mobility, ease of dislocation generation, or hydrogen carrying capability of dislocations. Therefore, hydrogen enhanced plasticity or inhibited dislocation motion in the presence of hydrogen can be ruled out in B2 ordered FA-129.

CONCLUSIONS

The Zr-containing Fe_3Al alloy shows better resistance to fatigue crack growth than does FA-129. The crack growth rate of B2 ordered FA-129 can be expressed as a superposition of purely mechanical fatigue and a corrosion-fatigue interaction term (5). There is a significant rate effect in the corrosion-fatigue contribution to crack growth of iron-aluminides. Dislocation-assisted diffusion is responsible for transport of hydrogen atoms into the bulk of the material for B2 ordered FA-129, and this process is the rate limiting step in hydrogen embrittlement during crack growth.

ACKNOWLEDGEMENTS

The authors are grateful to the DOE Fossil Energy Program for providing financial support under Martin Marietta Energy Systems Subcontract Number 19X-SF521C. The authors also are grateful for helpful discussions with Dr. V. K. Sikka of ORNL and to Dr. Sikka for providing test alloys.

REFERENCES

1. C.T. Liu, H.E. Lee and C.G. McKamey, Scripta Met. 23, 1989, p. 875.

2. C. G. McKamey, J. H. DeVan, P. F. Tortorelli and V. K. Sikka, J. Mat. Res. 6, 1991, p. 1779.

3. A. Castagna, Ph.D. Thesis, Rensselaer Polytechnic Inst., 1994.

4. A. Castagna and N. S. Stoloff, Mater. and Design 14, 1993, p. 73.

5. A. J. McEvily and R. P. Wei, in Corrosion-Fatigue: Chemistry, Mechanics and Microstructure, O. F. Devereux, A. J. McEvily, R. W. Staehle, Eds., (NACE, Houston, 1972), NACE-2, p. 381.

6. J. K. Tien and R. J. Richards, Scripta Metall. 9, 1975, p. 1097.

7. A. Castagna and N. S. Stoloff, Mat. Sci. & Eng. A192/193, 1995 p. 399.

THE EFFECT OF GRAIN REFINEMENT ON THE ROOM-TEMPERATURE DUCTILITY OF AS-CAST Fe_3Al-BASED ALLOYS

S. Viswanathan, V. K. Andleigh, and C. G. McKamey

Oak Ridge National Laboratory
P.O. Box 2008
Oak Ridge, TN 37831-6083

ABSTRACT

Fe_3Al-based alloys exhibit poor room-temperature ductility in the as-cast condition. In this study, the effect of grain refinement of the as-cast alloy on room-temperature ductility was investigated. Small melts of Fe-28 at. % Al-5 at. % Cr were inoculated with various alloying additions and cast into a 50- × 30- × 30-mm graphite mold. The resulting ingots were examined metallographically for evidence of grain refinement, and three-point bend tests were conducted on samples to assess the effect on room-temperature ductility. Ductility was assumed to correlate with the strain corresponding to the maximum stress obtained in the bend test. The results showed that titanium was extremely effective in grain refinement, although it severely embrittled the alloy in contents exceeding 1%. Boron additions strengthened the alloy significantly, while carbon additions reduced both the strength and ductility. The best ductility was found in an alloy containing titanium, boron, and carbon. In order to verify the results of the grain refinement study, vacuum-induction melts of selected compositions were prepared and cast into a larger 25- × 150- × 100-mm graphite mold. Tensile specimens were machined from the ingots, and specimens were tested at room temperature. The results of the tensile tests agreed with the results of the grain refinement study; in addition, the addition of molybdenum was found to significantly increase room-temperature tensile ductility over that of the base alloy.

INTRODUCTION

The primary reason for the poor room-temperature ductility of Fe_3Al-based alloys is generally accepted to be environmental embrittlement due to hydrogen produced by the reaction of aluminum with water vapor present in the test atmosphere.[1] In the as-cast condition, another possible reason for the low room-temperature ductility is the large grain size (0.5 to 3 mm) of the cast material.[2] While recent studies on iron aluminides in the wrought condition have led to higher room-temperature ductility and increased high-temperature strength,[1] limited studies have been conducted on iron aluminides in the as-cast condition. The purpose of this study was to induce grain refinement of the as-cast alloy through alloying additions to the melt and study the effect on room-temperature ductility as measured by the strain corresponding to the maximum stress obtained in a three-point bend test. A base charge of Fe-28% Al-5% Cr alloy was used; as in previous studies, this ternary alloy exhibited the highest tensile ductility of several alloys tested.[2]

DISCUSSION OF CURRENT ACTIVITIES

Grain Refinement Study

As part of a study on wrought alloys, a large number of cast alloy samples with a variety of alloying additions had been produced in the form of 450-g chill-cast ingots.[3] Samples were obtained close to the hot-top sections of these ingots; were polished and then swab-etched using a solution of 25 mL acetic acid, 15 mL nitric acid, 15 mL hydrochloric acid, and 5 mL water; and finally, were examined under an optical microscope. In this preliminary screening, only samples containing titanium and boron showed evidence of grain refinement; samples containing other additions (including Ce, Hf, Mg, Mn, Mo, Nb, Si, V, Y, and Zr) did not show any evidence of grain refinement. Consequently, the effects of titanium and boron were examined in detail in this study.

For the grain refinement study, approximately 10 kg of a base charge material of Fe-28% Al-5% Cr alloy was prepared by melting elemental materials in air in an induction furnace under an argon blanket, and cast into a graphite mold to produce rods of approximately 35 mm diam and 200 mm length. The rods were ground to 28 mm diam and cut to provide cylinders consisting of approximately 300 g of base charge material. These cylinders were subsequently melted in an induction furnace specially constructed for this study, alloyed with a variety of inoculants designed to promote grain refinement, and cast into a preheated graphite mold to produce 30- × 50- × 30-mm ingots. Table 1 indicates nominal compositions for the heats in the grain refinement study. A mold preheat temperature of 400°C was used throughout the study. Although the pouring temperature of the metal was not measured, it is estimated that it was in the range of 1500 to 1600°C since the liquidus temperature of Fe_3Al-based alloys is approximately 1470°C. Also, although an argon blanket was used during melting, an oxide layer formed on the melt surface, and a preheated graphite rod was quickly inserted into the melt prior to pouring to break up the surface oxide layer and allow a smooth pour. Figure 1 illustrates the graphite mold used in the study.

Table 1. Nominal compositions of cast ingots in grain refinement study

Heat No.	Composition (at. %)					
	Fe	Al	Cr	Ti	C	B
GR-07	Balance	28.0	5.0			
GR-09	Balance	28.0	5.0	1.0	0.1	
GR-10	Balance	28.0	5.0	1.0	0.1	0.12
GR-11	Balance	28.0	5.0	2.0		
GR-12	Balance	28.0	5.0	1.0	0.1	0.52
GR-19	Balance	28.0	5.0	1.5		
GR-20	Balance	28.0	5.0			0.12
GR-21	Balance	28.0	5.0			0.52
GR-26	Balance	28.0	5.0			
GR-27	Balance	28.0	5.0	1.0	0.1	0.02
GR-28	Balance	28.0	5.0			0.02
GR-30	Balance	28.0	5.0		0.1	
GR-34	Balance	28.0	5.0	1.0		0.02
GR-36	Balance	28.0	5.0	1.5		0.02

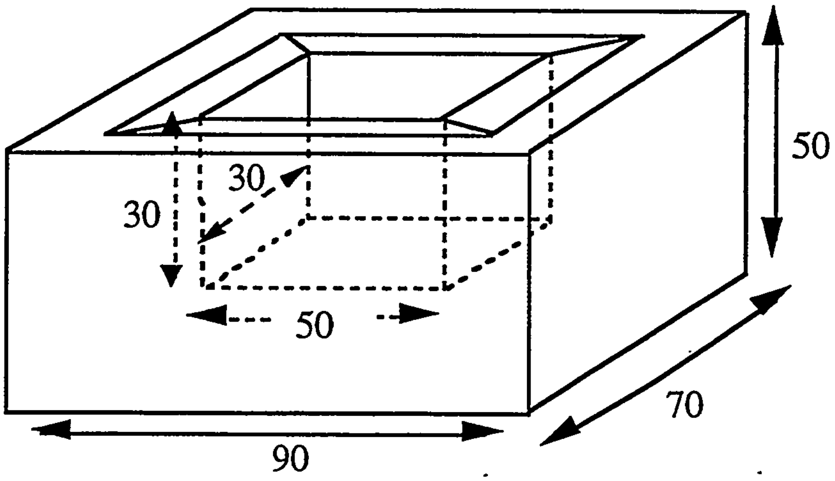

Fig. 1. Graphite mold used in grain refinement study (dimensions in mm).

Ingots were sectioned to obtain metallography and bend test specimens. Metallography specimens were polished, swab-etched, and examined under an optical microscope; ingot compositions were subsequently checked by energy dispersive spectroscopy (EDS). In cases where there was evidence of grain refinement, vertical sections were macroetched to reveal ingot macrostructure. Two bars of 4- × 4-mm cross section and 40 mm length were electrodischarge machined from locations toward the bottom of the ingot. After machining, bar edges were ground lightly on 600-grit silicon carbide paper, and the bars were electropolished in a solution of 7 parts methanol and 1 part sulfuric acid at 7.5 V for about 100 s. Two bend test specimens of 20 mm length were typically obtained from each bar. Specimens were ultrasonically cleaned for 3 min and washed in acetone before testing. A gage length of 10 mm was used in the three-point bend test configuration. The stress and strain were calculated from the equations:

$$\sigma = 3PL/2wt^2 \tag{1}$$

and

$$\varepsilon = 6ty/L^2 \ , \tag{2}$$

where σ = stress, ε = strain, P = load, y = displacement, L = gage length, w = specimen width, and t = specimen thickness.

Results of Grain Refinement Study

Figure 2 illustrates the results of the grain refinement study. As shown in Fig. 2(*a*), the base charge material produced an ingot consisting entirely of columnar grains. The addition of 1% Ti, 0.1% C, and 0.12% B produced some grain refinement in the center of the ingot, although a columnar zone is seen along the edge of the ingot [see Fig. 2(*b*)]. The addition of 0.52% B provided a marginal increase in grain refinement in the center of the ingot [see Fig. 2(*c*)], while the addition of 2% Ti provided extensive grain refinement over the entire ingot [see Fig. 2(*d*)]. Additions of titanium at levels less than 1% did not produce grain refinement, and additions of other alloying elements at levels up to 2% also did not have an effect. It must be noted that because of the high-thermal gradients expected in the solidifying metal due to the use of a small graphite mold, preferentially giving rise to columnar grains, this test provides a very severe test of grain refinement efficacy.

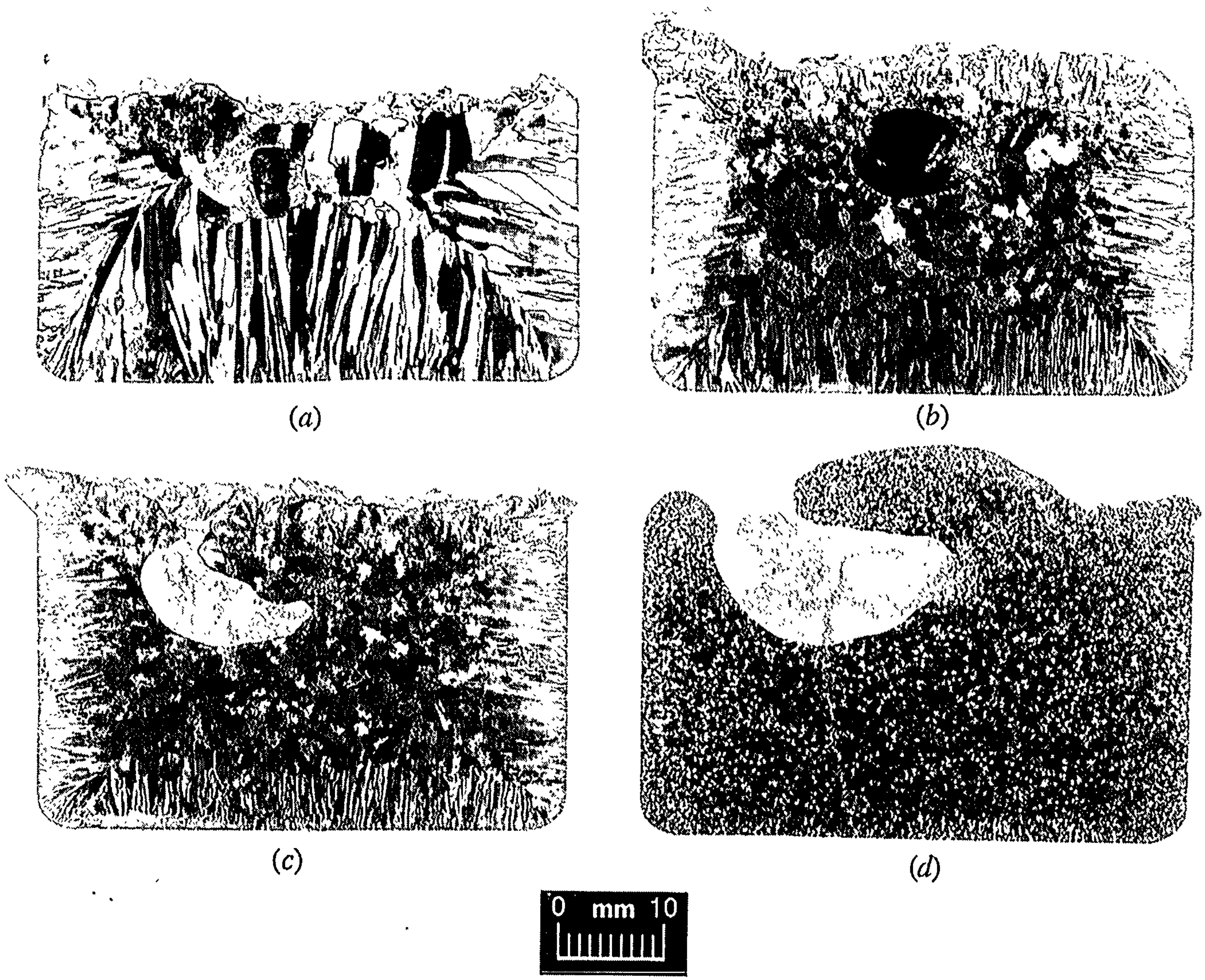

Fig. 2. Photographs of macroetched sections of ingots from grain refinement study: (*a*) base charge, (*b*) 1% Ti-0.12% B-0.1% C, (*c*) 1% Ti-0.51% B-0.1% C, and (*d*) 2% Ti.

Figure 3 shows the results of the three-point bend tests. Figure 3(*a*) shows the maximum stress values obtained, and Fig. 3(*b*) shows the strains corresponding to the maximum stress. For each case, the values obtained may be compared to that obtained for the base charge of Fe-28% Al-5% Cr alloy. The trends obtained for maximum stress and strain are similar and indicate that the addition of titanium or carbon alone serves to embrittle the material, lowering both the stress and strain values obtained. The addition of both titanium and carbon produced the lowest values of stress and strain at failure. The addition of boron improved both the maximum stress and the strain obtained, although ductility was somewhat affected as boron was increased. The effect of boron on the strength of the alloy may also be the reason that boron decreases the weldability of iron-aluminide alloys. Interestingly, the effects of boron and carbon seemed to offset each other with respect to the maximum stress obtained; carbon-containing alloys seemed to require more boron to produce the same strength levels as alloys containing no carbon. Boron also had a strong effect on the maximum strain obtained, inasmuch as the presence of any boron in the alloy provided moderate ductility at least equal to the base charge material, even in the presence of carbon. The maximum ductility was obtained in an alloy containing 1% Ti, 0.1% C, and 0.52% B, although this value was almost identical to that obtained for the alloy containing 0.02% boron alone.

The results of the study clearly establish the grain refinement propensity of titanium and the effect of boron on ductility, although titanium also serves to embrittle the material. In general, the addition of alloying elements other than boron invariably served to decrease both the maximum stress and the maximum strain obtained, indicating that for as-cast Fe_3Al-based alloys, the addition of alloying elements designed to serve as inoculants is likely to have a negative effect on ductility, even when grain refinement is obtained.

Scale-up Study

In order to verify the results of the grain refinement study, a vacuum-induction melt of the 1% Ti, 0.1% C, and 0.52% B alloy that exhibited the maximum ductility in the grain refinement study was prepared and cast into a 25- × 150- × 100-mm graphite mold. Tensile specimens were machined from the ingot, and specimens were tested at room temperature. The results were compared with that for the base ternary alloy obtained previously.[2] In addition, the effect of molybdenum additions to the base ternary alloy was also investigated. Table 2 indicates nominal compositions for the heats in the scale-up study. Figure 4 illustrates the graphite mold used in the scale-up study.

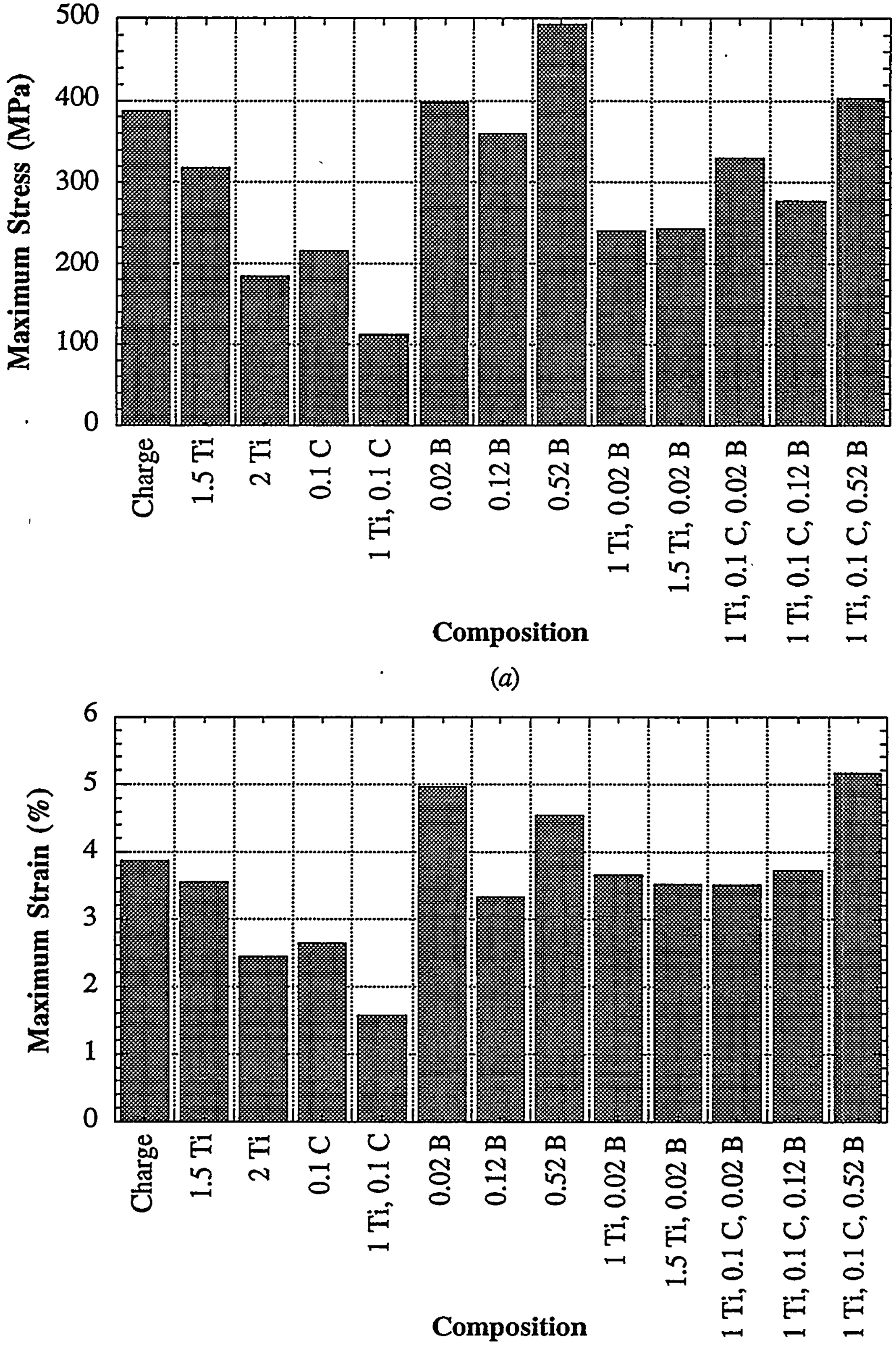

(*a*)

(*b*)

Fig. 3. Results of three-point bend tests: (*a*) maximum stress and (*b*) maximum strain.

Table 2. Nominal compositions of cast ingots in scale-up study

Heat No.	Composition (at. %)						
	Fe	Al	Cr	Mo	Ti	C	B
16097	Balance	28.0	5.0		1.0	0.1	0.52
15897	Balance	28.0	5.0	0.02			
16094	Balance	28.0	5.0	0.05			
16095	Balance	28.0	5.0	0.1			
16096	Balance	28.0	5.0	0.25			

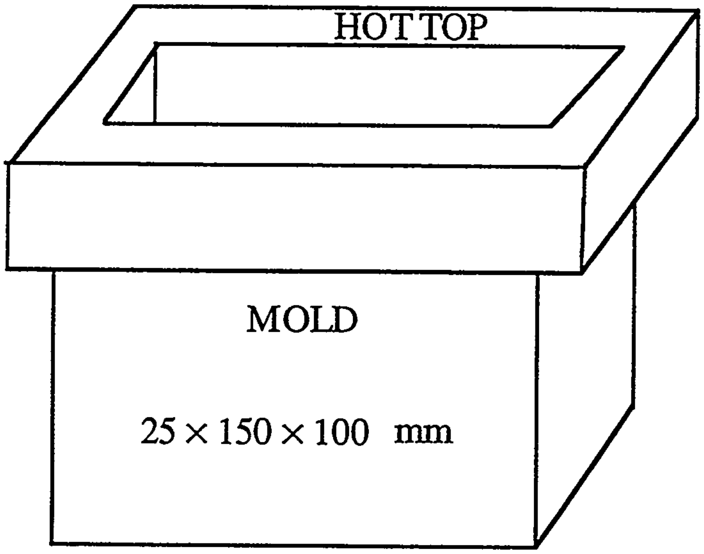

Fig. 4. Graphite mold used in scale-up study (dimensions in mm).

Figure 5 shows the results of room-temperature tensile tests for specimens in the scale-up study. Figure 5(*a*) indicates the effects of alloying on the yield and tensile strength, while Fig. 5(*b*) shows the effect on tensile elongation. Alloying had almost no effect on the yield strength, while tensile strength increased from 250 to 300 MPa. It is likely that yield strength is dominated by the large grain size of the as-cast material and, consequently, is not greatly affected by alloying. The 1%Ti, 0.1% C, and 0.52% B alloy that exhibited the maximum ductility in the grain refinement study did not exhibit increased ductility in the scale-up study. However, equally significant, there was no drop in ductility as might have been expected due to the addition of titanium and carbon. Interestingly, the

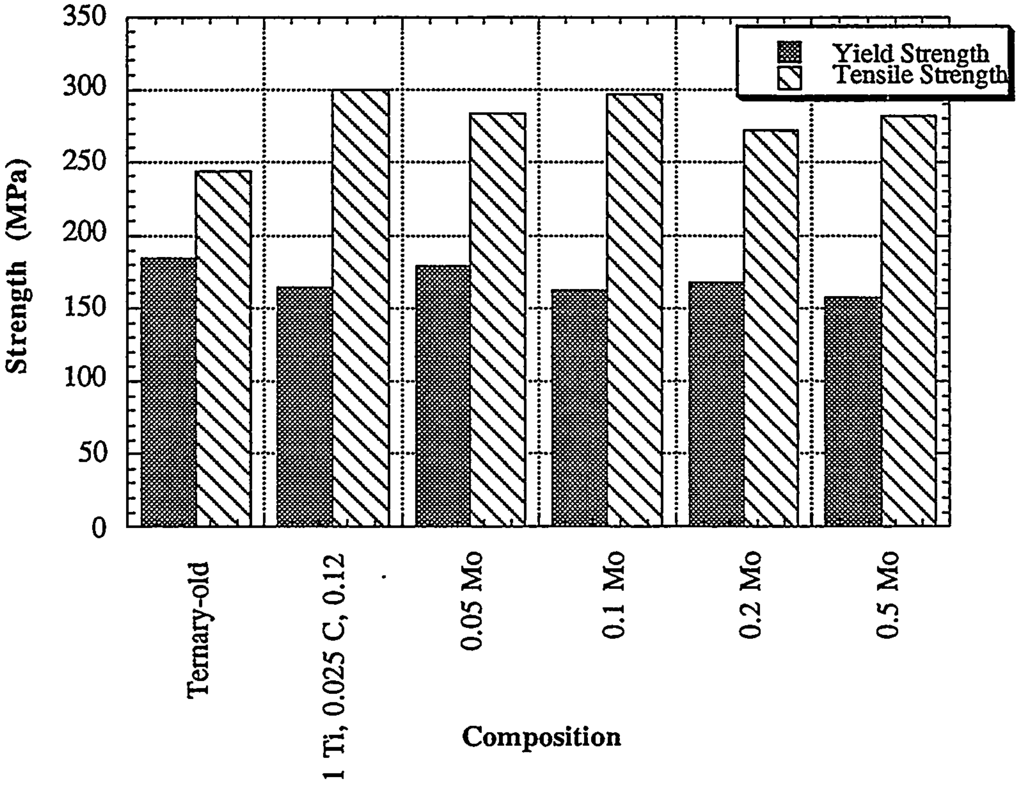

(*a*)

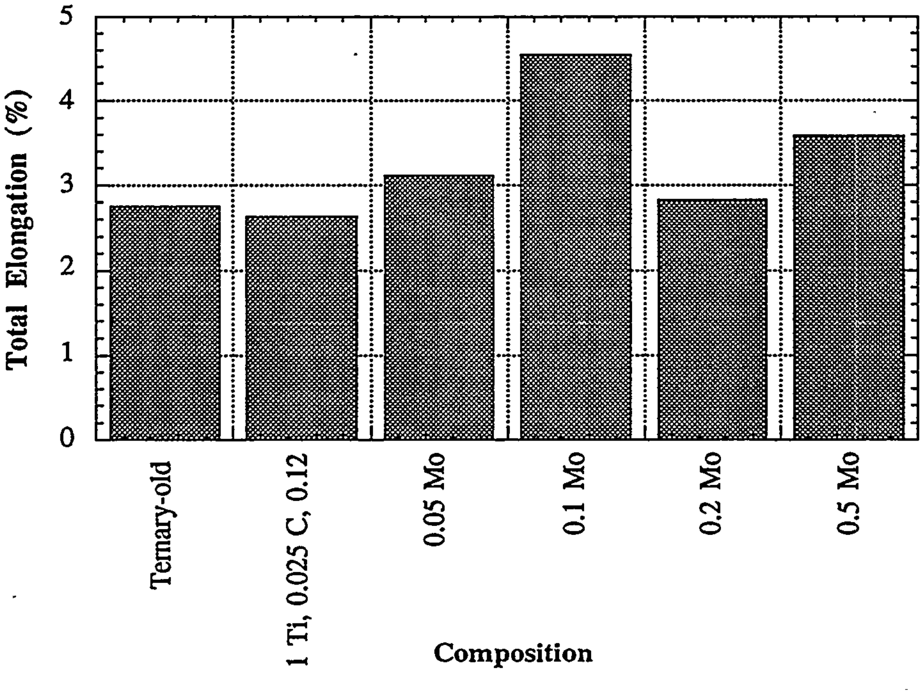

(*b*)

Fig. 5. Results of tensile tests for scale-up study: (*a*) yield strength and ultimate tensile strength and (*b*) total elongation.

addition of molybdenum produced a significant increase in room-temperature ductility over the base alloy, at a level of 0.1%. Additions less than or greater than 0.1% did not seem to change the ductility significantly, although marginal increases may be noted at the 0.05 and 0.5% levels. The reason for the increase in room-temperature ductility on the addition of molybdenum is under investigation, although there is some indication that the molybdenum may serve to tie up the carbon and prevent it from segregating to the grain boundaries, where it can cause embrittlement. The 4.5% tensile elongation obtained at a level of 0.1% molybdenum is the highest recorded in any as-cast Fe_3Al-based alloy cast in the same size and type of ingot mold as that used in this study.

ACKNOWLEDGMENTS

The authors wish to thank J. D. Vought for melting and casting the base charge material; B. G. Whitson and K. M. Byrd for the construction of the melting apparatus; G. W. Garner, E. C. Hatfield, and C. R. Howell for their assistance with the grain refinement experiments; the staff of the Metallography Department for their assistance; C. A. Carmichael for help with bend tests; B. G. Gieseke and G. M. Goodwin for reviewing the paper; K. Spence for editing; H. S. Payne and the Science and Engineering Research Semester (SERS) Program, U.S. Department of Energy, for supporting one of the authors (V. K. Andleigh) from September to December 1993; and M. L. Atchley for final preparation of the manuscript.

Research for this work was sponsored by the U.S. Department of Energy, Office of Fossil Energy, Advanced Research and Technology Development Materials Program, [DOE/FE AA 15 10 10 0, Work Breakdown Structure Element ORNL-2(H)] under contract DE-AC05-84OR21400 with Lockheed Martin Eenrgy Systems.

REFERENCES

1. C. T. Liu, in *High Temperature Ordered Intermetallics V*, eds., I. Baker, J. D. Whittenberger, R. Darolia, and M. H. Yoo (Mater. Res. Soc. Symp. Proc. 288, Pittsburgh, PA, 1993) p. 3.

2. S. Viswanathan, C. G. McKamey, P. J. Maziasz, and V. K. Sikka, in *Processing, Properties, and Applications of Iron Aluminides*, eds. J. H. Schneibel and M. A. Crimp (The Minerals, Metals, and Materials Society, Warrendale, PA, 1994) pp. 159-169.

3. C. G. McKamey, C. T. Liu, S. A. David, J. A. Horton, D. H. Pierce, and J. J. Campbell, *Development of Iron Aluminides for Coal Conversion Systems*, ORNL/TM-10793, Martin Marietta Energy Systems, Inc., Oak Ridge Natl. Lab., 1988.

WELDABILITY OF POLYCRYSTALLINE ALUMINIDES

A. A. Fasching*, G. R. Edwards*, R. P. Burt*, and S. A. David#

Center for Welding and Joining Research
Department of Metallurgical and Materials Engineering
Colorado School of Mines
Golden, CO 80401

#Metals and Ceramic Division
Oak Ridge National Laboratory
Materials Joining Group
Oak Ridge, TN 37831

ABSTRACT

Slow strain rate tensile tests were conducted in varying water vapor atmospheres on weldments refined by magnetic arc oscillation with average fusion zone grain sizes ranging between 115 and 530μm. Fracture strength and percent strain to fracture were measured for each fusion zone microstructure. The fracture strength data followed Hall-Petch behavior, and water vapor significantly reduced fracture strength. The finer grain size fusion zones were found to be less susceptible to hydrogen cracking and more tolerant of high hydrogen concentrations than coarse fusion zone grain structures. Microstructural refinement via arc oscillation was also found to be suitable only for well-controlled fabrication environments.

INTRODUCTION

Iron aluminide alloy FA-129 is susceptible to cold cracking during gas-tungsten arc (GTA) welding and previous work has shown that iron aluminides are susceptible to environmental embrittlement when tensile tested in the presence of water vapor[1,2]. To further investigate hydrogen cold cracking in iron aluminides and, specifically, to study the effect of fusion zone grain size on cracking susceptibility, welds were produced using magnetic arc oscillation to refine the fusion zone grain structures. Weldments with average fusion zone grain sizes ranging between 115 and 530μm were slow strain rate tensile tested in varying water vapor atmospheres. The results of the investigation are presented within this paper.

EXPERIMENTAL PROCEDURE

An experiment was developed to test the resilience of the refined fusion zone microstructures to hydrogen embrittlement in water vapor atmospheres. Alloy FA-129 samples were welded in pure argon, then slow strain rate tensile tested in argon containing varying concentrations of water vapor. The tests were strain controlled at a rate of 2.78×10^{-6}/s. Four different weldments were produced using different welding and oscillation parameters, shown in Table 1. The different heat inputs and oscillation parameters produced four unique microstructures for evaluation. The microstructure of the welds differed significantly from that of the base material; consequently, all of the applied strain concentrated within the fusion and heat affected zones, and fracture occurred within the same region.

Table 1 Welding Parameters Used to Produce Fusion Zones of Differing Grain Sizes

Microstructure Type	Current (amps)	Arc Gap (inches)	Heat Input (J/mm)	Oscillation Frequency (Hz)	Oscillation Amplitude Setting	Oscillation Orientation Relative to Welding Direction
A	38	0.060	80.9	–	–	–
B	31	0.060	73.3	–	–	–
C	31	0.060	73.3	10.0	250 (0.8mm)	90 degrees
D	31	0.060	73.3	10.0	250 (0.8mm)	45 degrees

Alloy FA-129 samples were tensile tested in a plexiglas environmental chamber designed specifically for the MTS system. The moisture probe was located directly between the grips in the back of the chamber. For all tests, the chamber was purged with Grade 5 argon until the moisture reading was less than 200 ppm. Argon was continually passed through the system during testing and a measurement was recorded both before and after testing. For tests conducted in moisture, the chamber was purged and then water was bubbled through distilled water using an ultra-slow flow rate meter. Once again the atmosphere was allowed to equilibrate prior to testing.

RESULTS

The unoscillated microstructures produced are shown in Figures 1a and 1b, and the transversely oscillated fusion zone microstructures are shown in Figures 1c and 1d. The welds of the unoscillated Microstructure A, shown in Figure 1a, consisted of large columnar grains. The second unoscillated microstructure (Microstructure B), shown in Figure 1b, also exhibited a columnar grain

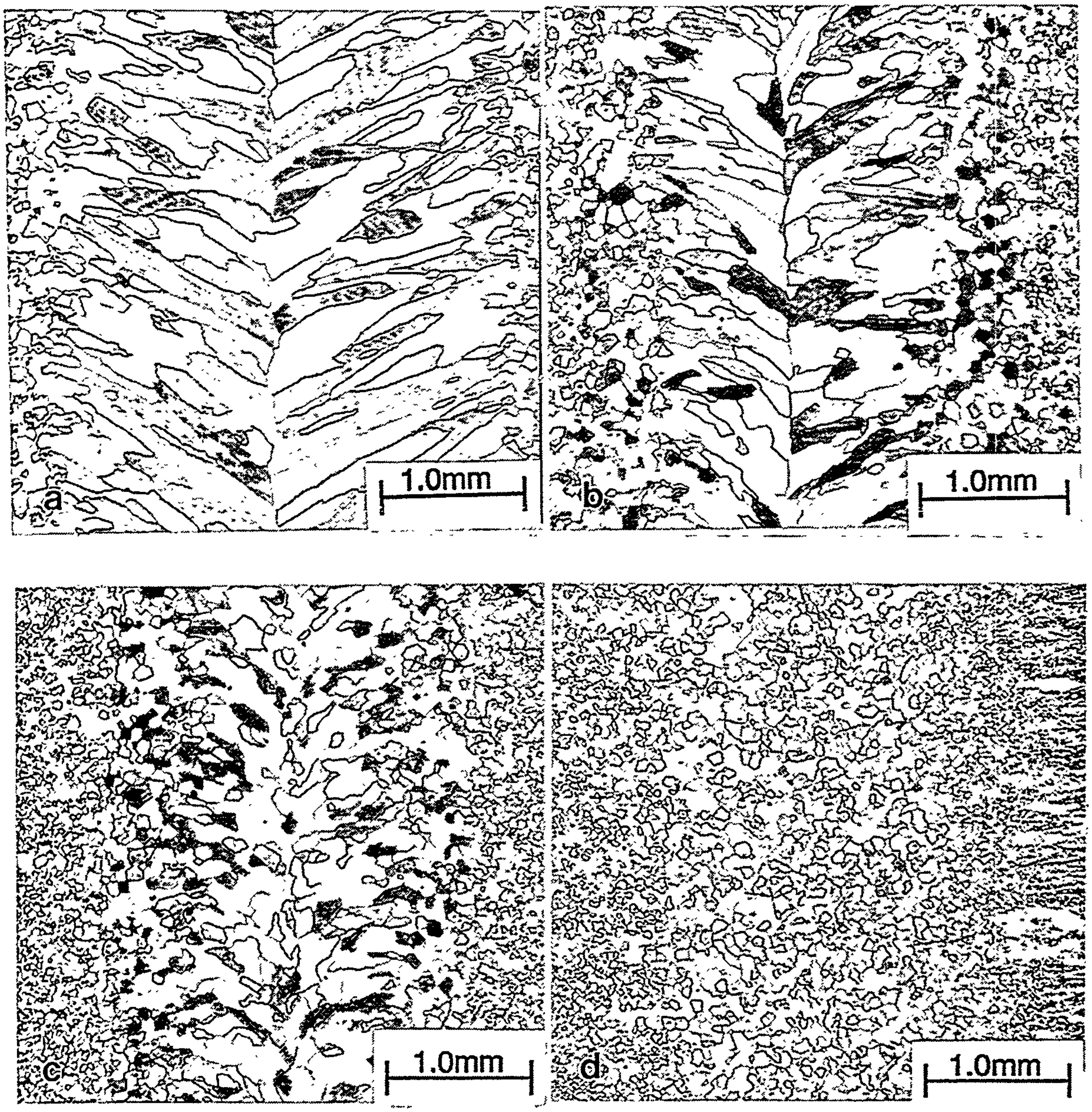

Fig. 1. Microstructures used for weldments used in slow strain rate testing. a) Microstructure A (H.I.=81 J/mm), b) Microstructure B (H.I.=73 J/mm), c) Microstructure C (90° at Freq.=10 Hz, Amp.=0.8mm), and d) Microstructure D (45° at Freq.=10 Hz, Amp.=0.8mm).

structure and a well defined centerline. In this lower heat input weld, however, the grains were not as large as grains in the higher heat input weld. The transversely oscillated fusion zone (Microstructure C), Figure 1c, looked similar to the unoscillated fusion zone (Microstructure B) in Figure 1d; however, in this microstructure there was no clear centerline. The grains in this microstructure were still elongated. Finally, the fusion zone created by oscillating the arc at 45 degrees to the welding direction (Microstructure D) resulted in a nearly equiaxed, fine-grained fusion zone (Figure 1d). Also, no clear centerline or fusion line was apparent in this weldment.

Fusion zone grain size measurements were made using a Leco image analyzer system. The results of the grain size measurements are shown in Table 2. The average grain size and aspect ratio of each microstructure are reported as well. As shown in Figure 1, the weld with the highest heat input contained the largest grains and the largest aspect ratio (Figure 1a). Oscillating the arc at a 45-degree angle to the welding direction produced the smallest grains with the smallest aspect ratio (Figure 1d).

Table 2 Grain Dimensions of FA-129 Fusion Zones

Microstructure	average length (l), μm	average width (w), μm	average thickness (t), μm	average grain size, μm	aspect ratio (l/w)
A	1,250	168	176	530	7.4
B	637	141	109	300	4.5
C	300	123	94	172	2.4
D	139	107	100	115	1.3

Slow strain rate tensile test were conducted on welds of all four microstructures in both pure argon and argon containing four water vapor levels. Load at fracture and strain at fracture were recorded for each sample. Welds of Microstructure C broke at the fusion line. The fracture surfaces were either transgranular cleavage or a mixed mode of intergranular and transgranular cleavage.

Fracture strength versus moisture content was plotted for welds representing each fusion zone grain size, as shown in Figure 2. A linear regression was performed on the data for each grain size. The correlation coefficient (R) is shown and describes the accuracy of the fit. (An R value equal to one designates a perfect fit.) The slope of the line for the coarsest (530 μm) fusion zone is slightly steeper than that for the most refined (115 μm) fusion zone. The data for the two intermediate grain sizes plot nearly on top of one another. Percent strain at fracture versus the moisture content in the

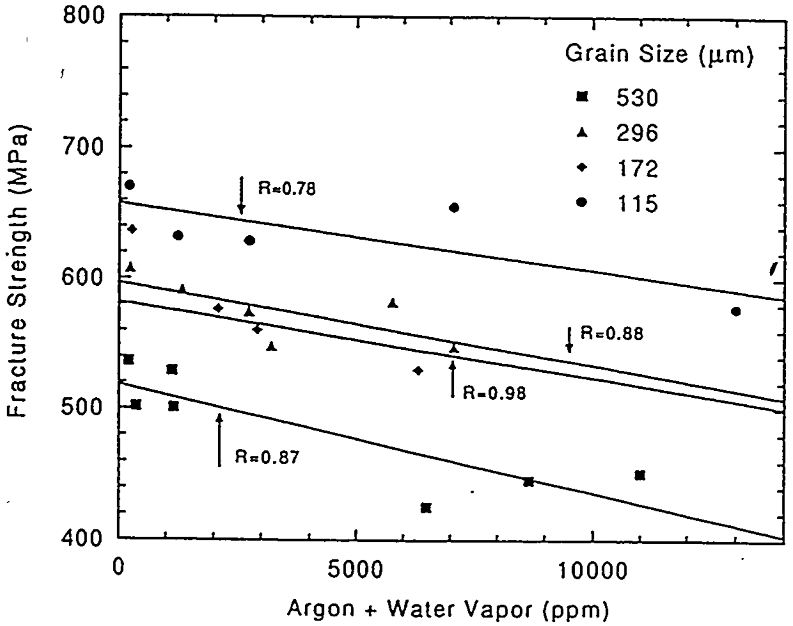

Fig. 2. Fracture strength versus water vapor content in the atmosphere showing the effect of fusion zone grain size on the mechanical properties of the weldment.

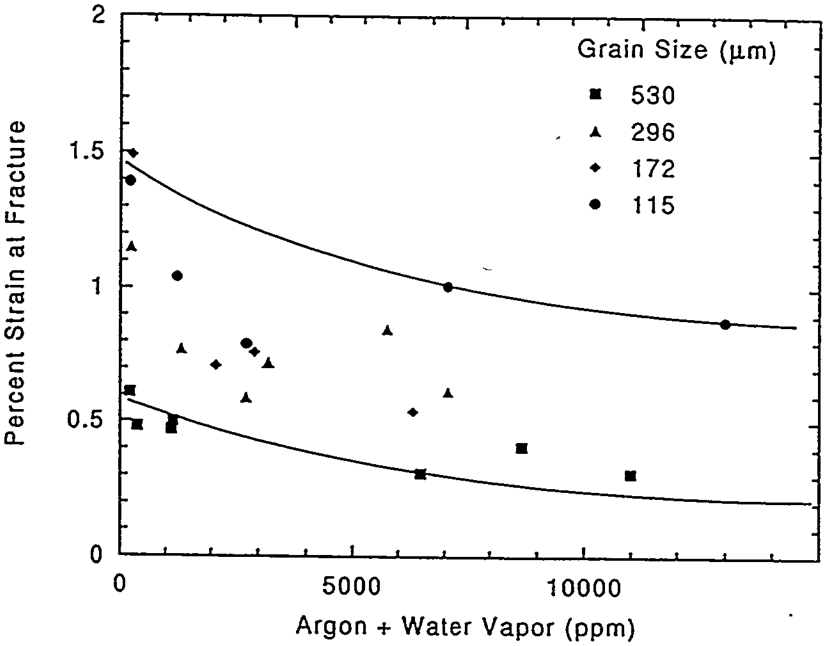

Fig. 3. Percent elongation at fracture for weldments of different fusion zone grain size tested in atmospheres of varying levels of water vapor.

atmosphere was also plotted for each of the fusion zone grain sizes as shown in Figure 3. These data, while not as well defined as the fracture strength data, exhibited the same basic trends. The most refined fusion zone (115 μm) exhibited the highest percent elongation at fracture and the coarsest fusion zone (530 μm) showed the least elongation at fracture.

Figure 4 is a Hall-Petch style plot where each range of the water vapor levels tested is shown. Since testing occurred over a range of water vapor concentrations, points were read from the linear regression fits of the data in Figure 3 at the specific levels plotted. Again a linear regression was conducted on each of these data and the slope of each line was determined. Again the correlation coefficient (R) is shown for each line. The slopes of the lines in Figure 4 correspond to the k_F value in the Hall-Petch equation. The k_F value was plotted as a function of water vapor concentration, as indicated in Figure 5. The data fit a square root function showing $k_F = 70 + 0.25M^{1/2}$ (MPa mm$^{1/2}$), where M is the water vapor concentration in parts per million. The σ_o term is also a function of water vapor, where $\sigma_o = 472 - 1.5M^{1/2}$ (MPa). The plot of σ_o versus water vapor concentration is also shown in Figure 5.

DISCUSSION

Iron aluminides are embrittled when tested in water vapor atmospheres at strain rates slower than 10^{-3} /s (ref.3). A slow strain rate test (10^{-8}/s) was developed to evaluate the hydrogen embrittlement of alloy FA-129 weldments. The slowest reasonable strain rate was selected to maximize the time for hydrogen to diffuse. Slow strain rate tensile testing revealed that welds containing fine-grained fusion zones resisted hydrogen embrittlement in the presence of water vapor significantly better than welds of coarse-grained fusion zones. Microstructure D, the smallest and most equiaxed fusion zone, exhibited the highest fracture strength and the most ductility at fracture. The trends were very clear for the fracture strength data, and a first order polynomial equation was fit to these data. The values of the correlation coefficient (R) for each fusion zone grain structure are shown in Figure 2. These values ranged from 0.7 to 0.99. Variations in moisture level over the duration of the test and normal experimental error can account for some of the scatter seen in the fracture data. However, the linear regression fits accurately describe the trend of these data.

Using points from the linear fits in Figure 2, the fracture strength was plotted as a function of the inverse square root of fusion zone grain size, as shown in Figure 4, for four water vapor levels. Again, a first order polynomial equation was fit to the data for each water vapor concentration, and the correlation coefficient (R) is shown. The data for the coarsest fusion zone, Microstructure A, fall below the linear regression line. Microstructure A had a very large aspect ratio and an obvious

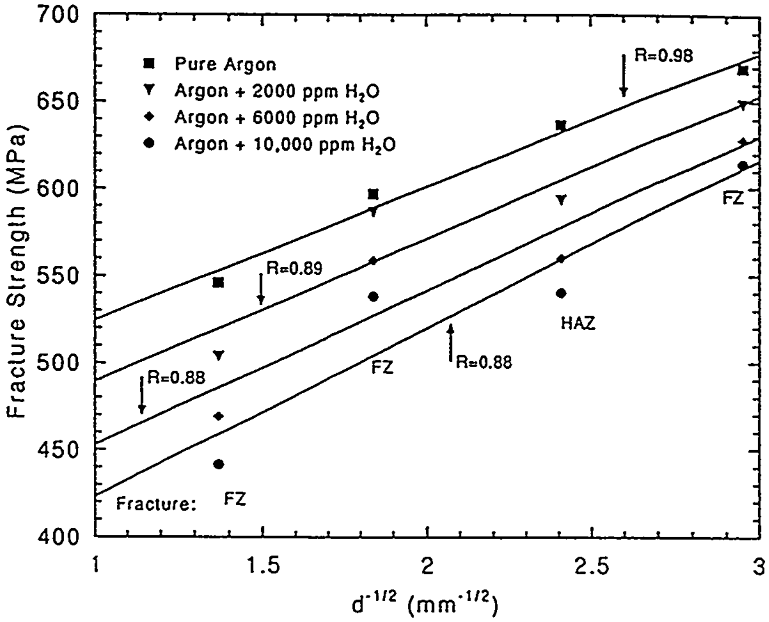

Fig. 4. Hall-Petch plot for iron aluminide alloy FA-129 weldments tested in varying water vapor atmospheres.

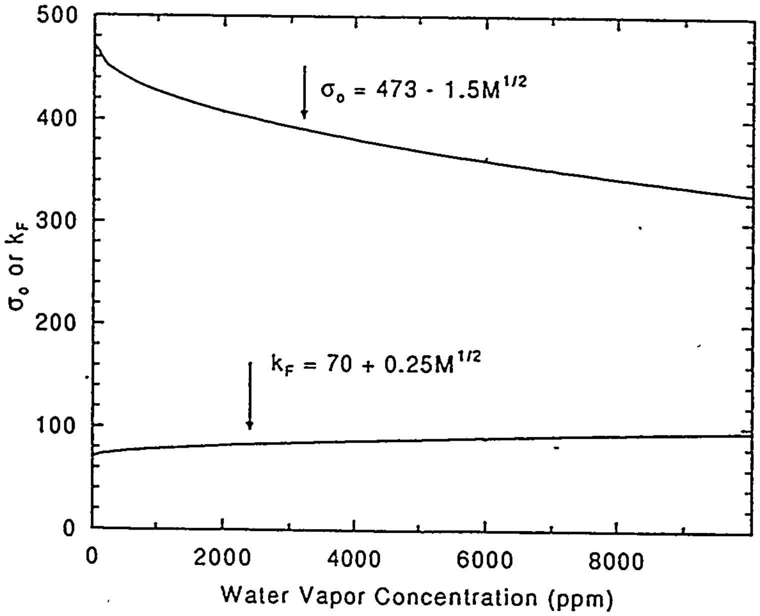

Fig. 5. k_F and σ_o as a function of water vapor concentration for aluminide alloy FA-129 weldments.

centerline. The effect of the directional grains and the centerline was lessened by averaging of the grain size in three directions. Hence, the linear regression predicts a higher fracture strength for Microstructure A (530 μm) than was measured, as shown on Figure 4. The data points of Microstructure C (172 μm) also fall below the linear regression line. In this case, failure occurred in the heat affected zone causing the measured fracture strength to be less than that of the actual weldment.

The slopes of these lines, shown in Figure 4, slightly increased as water vapor concentration increased, indicating that k_F is a function of water vapor concentration. The slope varied from 77 in pure argon to 97 MPa $mm^{1/2}$ in argon containing 10,000 ppm water vapor. This change in slope is small and the experimental scatter of the data could account for the difference.

The y-intercept decreased significantly as water vapor concentration increased, indicating that σ_o, the flow stress, was a strong function of water vapor concentration. The flow stress ranged from 448 MPa in pure argon to 327 MPa in argon containing 10,000 ppm water vapor; thus, a 30 percent decrease in flow stress occurred over the range of water vapor concentrations tested. Figure 5 shows that σ_o was a much stronger function of water vapor concentration than k_F.

These results and other results beyond the scope of this paper show that arc oscillation requires tight control of the welding process[4]. Optimal refinement parameters are sensitive to welding water vapor concentration, material composition, and heat input[4]. Magnetic arc oscillation was shown to be an effective method for refining fusion zone grain structures in iron aluminide alloy FA-129; however, it was found to be best suited for well-controlled fabrication environments. Other techniques such as inoculation should be investigated to refine the fusion zone grain structures in field situations where precise parameter control is not available.

CONCLUSIONS

1. Arc oscillation was shown to be an effective method for refining fusion zone microstructures in iron aluminide alloy FA-129 by changing the thermal gradients in the weld pool and affecting the competitive growth process.
2. Slow strain rate tensile tests showed fine-grained iron aluminide fusion zones to be less susceptible to hydrogen cracking and more tolerant of high hydrogen concentrations than coarse fusion zone grain structures. The fracture strength data was found to obey the Hall-Petch relationship.
3. Microstructural refinement by arc oscillation is suitable for well-controlled fabrication environments. Optimal refinement parameters were sensitive to numerous processing variables including welding water vapor concentration, material composition, and heat input.

4. Fusion zone inoculation or another method of fusion zone grain refinement should be considered to refine weldments produced in field fabrication situations.

CURRENT AND FUTURE WORK

Work now centers on using weld pool inoculation to refine the fusion zone. The study will follow the same format as the arc oscillation study. The method will first be tested and optimized by welding in a pure argon environment. Slow strain rate tensile tests will then be performed in atmospheres of varying water concentrations on welds refined in pure argon to determine the effect of grain size on hydrogen embrittlement. Finally, successful refinement of the fusion zone by inoculation while welding in environments of varying water vapor concentration will be attempted.

Powdered titanium and niobium carbide have been selected as the inoculants for the study (based on compatible physical properties and availability). The inoculant is added to the weld by machining a groove in the base plate, which is then filled with the powder and covered with an iron aluminide protective cap. The GTA welds are made using the same experimental equipment used in previous work.

Preliminary welds made by inoculating the fusion zone have shown significant fusion zone refinement. Figure 6 shows the fusion zone microstructure of an FA-129 iron aluminide weld inoculated with titanium powder (99.5%, -325 mesh). The heat input was 142 J/mm and the average grain size was 65μm. It has not yet been determined if the titanium reacted with the base plate or environment; however, particles were visible in the weldment microstructure and account for approximately 2.5 volume percent of the fusion zone (Figure 7). Further analysis will be done to identify these particles as well as to characterize the reproducibility and cracking susceptibility of weldments prepared by this method.

REFERENCES

1. C.T. Liu, C.G. McKamey, and E.H. Lee, Scripta Metall., 24 (1990) p. 385-390.

2. S.A. David, T.Zacharia, and R.W. Reed, Proceedings of the Fourth Annual Conference on Fossil Fuel Materials, ORNL/FMP-90/1 (U.S. Dept. of Energy, Oak Ridge, TN, August 1990), p. 207.

3. N.S. Stoloff, D.J. Duquette, "Moisture and Hydrogen-Induced Embrittlement of Iron Aluminides", Journal of Metals, December 1993.

4. A.A. Fasching "Grain Refinement and Hydrogen Embrittlement in Iron Aluminide Alloy FA-129 Weldments", Thesis #4686, Colorado School of Mines, Golden, CO, May 1995.

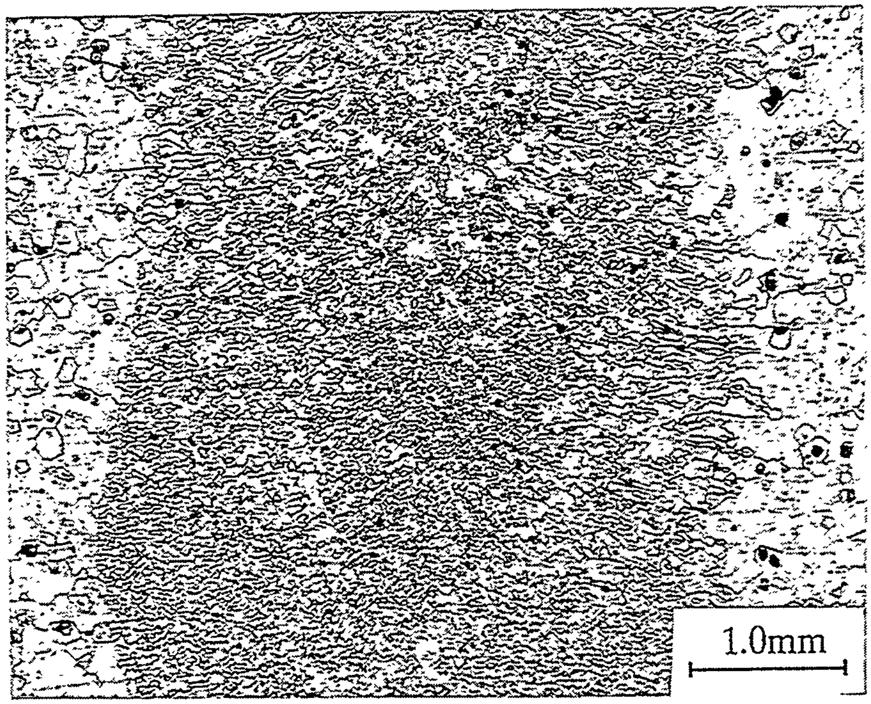

Fig. 6. Refined microstructure of titanium-inoculated FA-129 iron aluminide weld.

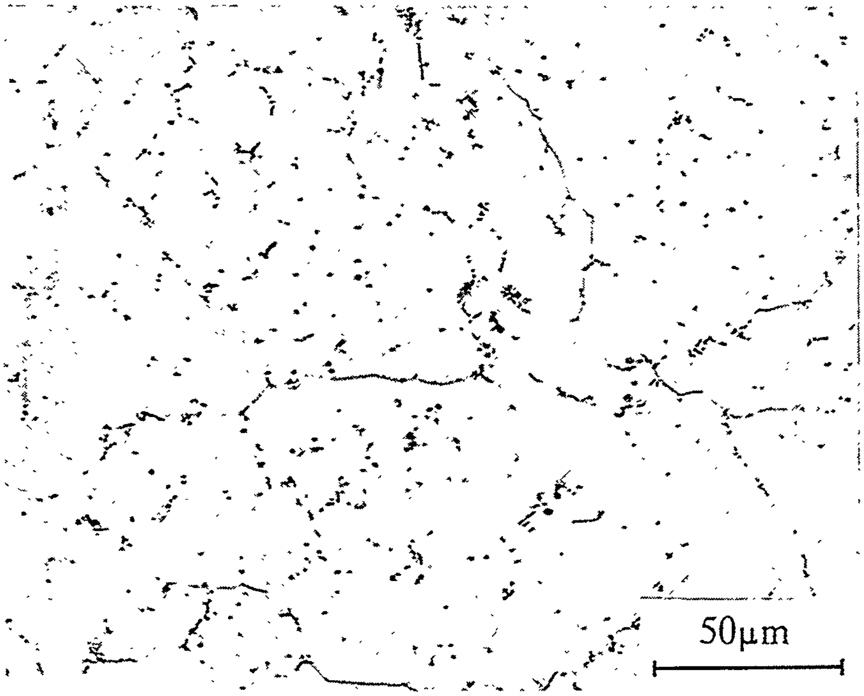

Fig. 7. Unidentified particles in titanium-inoculated FA-129 iron aluminide fusion zone.

ELECTRO-SPARK DEPOSITED COATINGS FOR PROTECTION OF MATERIALS

R.N. Johnson

Battelle Pacific Northwest Laboratory
P.O. Box 999, K3-59
Richland, WA 99352

ABSTRACT

Electro-Spark Deposition (ESD) is a micro-welding process that uses short duration, high-current electrical pulses to deposit or alloy a consumable electrode material onto a metallic substrate. The coating is fused (metallurgically bonded) to the substrate with such a low total heat input that the bulk substrate material remains at or near ambient temperature. Rapid solidification of the deposit typically results in an extremely fine-grained deposit that may be amorphous for some materials. Nearly any electrically conductive metal, alloy or cermet can be applied to metallic substrates.

The ESD process allows multi-layer coatings to be built-up using different materials to create graded structures or surface compositions that would be difficult to achieve by other means. A series of iron-aluminide coatings based on Fe_3Al and FeAl in combination with refractory metal diffusion-barrier coatings and supplementary additions of other elements are in corrosion testing at ANL. The most recent FeAl coatings are showing a factor of three better corrosion performance than the best previous coatings.

Technology transfer activities are a significant portion of the ESD program effort. Notable successes now include the start-up of a new business to commercialize the ESD technology, major new applications in gas turbine engines and steam turbine blade coatings, and in military, medical, metal-working, and recreational equipment applications.

INTRODUCTION

The objective of this program is to develop advanced materials coatings capable of operating in fossil energy environments beyond current materials limits, and to provide improvements in materials performance, durability and cost effectiveness for both new and existing power systems. Ultimately, new materials performance limits can enable new systems concepts.

A corollary objective is to further advance the Electro-Spark Deposition (ESD) technology and equipment, and to develop broad commercial applications through technology transfer activities.

Just as high-performance jet engines would not be possible today without protective coatings, so also does the next generation of high efficiency energy systems depend on protective coatings to survive the necessarily higher temperatures and more corrosive environments. The ESD coating process has been identified as one of the principal enabling technologies for such future systems. One of the reasons for this is that the exceptional structure produced in these metallurgically-bonded coatings makes them virtually immune to damage or spalling under severe service conditions and temperatures that destroy most other coatings. Additional attractions are that the process is portable (allowing coatings or surface treatments to be performed in the field), environmentally benign (creates no noxious wastes, fumes, or effluents), and highly cost-effective.

The Fossil Energy program currently funds the only research being conducted in the U.S. on this unique process. This program not only develops advanced coatings for fossil energy applications, but also contributes to improvements in understanding the basic phenomena occurring in the complex process parameters and surface effects and their relation to the quality, reproducibility, and rate of coating. The advances so far achieved are resulting in increased capabilities, reduced costs, and wider technology transfer opportunities.

BACKGROUND

Electro-spark deposition is a pulsed-arc micro-welding process that uses short-duration, high current electrical pulses to weld a consumable electrode material to a metallic substrate. The short duration of the electrical pulse allows an extremely rapid solidification of the deposited material and results in an extremely fine-grained, homogenous coating that may be amorphous for some materials. The microstructures produced by ESD can provide exceptional corrosion-resistance and wear-resistance for many materials.

The ESD process is one of the few methods available by which a fused, metallurgically-bonded coating can be applied with such a low total heat input that the bulk substrate material remains at or near ambient temperatures. This eliminates thermal distortions or changes in metallurgical structure of the substrate. Since the coating is metallurgically bonded, it is inherently more resistant to damage and spalling than the mechanically-bonded coatings produced by most other low-heat-input processes such as detonation gun, plasma spray, electro-chemical plating, etc. Nearly any electrically-conductive metal, alloy or cermet can be applied by ESD to metallic substrates.

Further background information on the ESD process is provided in References 1 and 2.

DISCUSSION OF PRIOR ACTIVITIES

Data collected so far indicate that ESD coatings tend to show lower corrosion rates in most environments than the same material would in either bulk form or as a coating applied by other processes. For example, ESD-applied coatings of chromium carbide-15% nickel exhibit significantly lower corrosion rates in aqueous and liquid metal environments than similar detonation-gun applied coatings.[3] The superior performance of the former is attributed to the extremely fine-grained, nearly amorphous structure inherent to the ESD coatings compared to the larger-grained, more heterogeneous detonation-gun coatings.

In tests at Argonne National Laboratory (ANL), this same ESD coating (chromium carbide-15% nickel) showed four times better sulfidation resistance than Type 310 stainless steel at 875°C.[4] Normally, this composition would not be expected to perform that well because of the strong susceptibility of a nickel matrix to sulfidation attack. Again, the fine grain structure is believed to be a major factor in the corrosion resistance. This observation is in agreement with other Fossil Energy Materials Program work that indicates one mechanism of improving lifetimes of protective oxide films and scales is to maintain as fine a grain structure as possible.[5] Further improvement in corrosion resistance of the chromium carbide coating was achieved by alloying aluminum into the surface by further ESD treatment.

One of the most significant advances in ESD coatings for use in sulfidation environments has been the successful development of Fe_3Al as a coating material. Oak Ridge National Laboratory (ORNL) has demonstrated the exceptional corrosion properties of Fe_3Al in bulk form, but alloying the Fe_3Al to achieve acceptable mechanical properties while maintaining optimum corrosion performance appears to be a challenge. As one alternative approach, ORNL supplied electrode materials to us for use in ESD coating development. (Using Fe_3Al as a coating material allows the selection of the substrates material for optimum mechanical properties and economy while retaining the corrosion resistance offered by the coating.) The coating results to date have been outstanding. The ESD parameters have been developed to the point that consistent, defect free coating over 100 μm thick can be applied relatively rapidly with good transfer efficiency. The Fe_3Al appears to produce some of the best and most economical coatings of all the materials evaluated for ESD application.

Further coating development is proving that the corrosion performance of the Fe_3Al coating can be significantly enhanced by the use of multi-layer ESD coating techniques. Sulfidation corrosion tests at ANL [6,7], for example, showed the beneficial effects of applying a Nb-1Zr diffusion barrier coating. The corrosion rate of an ESD coating of Fe_3Al was reduced by a factor of 2 in tests at 500°C when an intermediate ESD coating of Nb-1Zr was first applied to the steel, when compared to the same Fe_3Al coating applied directly to the steel.

Analyses of the Fe_3Al coatings with and without the Nb-1Zr diffusion barrier coating led to the conclusion that one of the principal reasons for the improved corrosion performance of the Fe_3Al coating over the Nb-1Zr layer was the higher aluminum content of the coating surface.[8] Scanning

Electron Microprobe (SEM) analyses showed that the intermediate diffusion barrier reduced the dilution of substrate elements into the coating weld zone and resulted in about 50% more aluminum in the surface of the coating (15% vs 9.5%).

After attempting unsuccessfully to alloy aluminum into the Fe_3Al surface by ESD treatments without generating surface cracks,[9] we obtained rods of FeAl from ORNL. This material proved to be nearly ideal for further increasing the aluminum content of the ESD coatings.

DISCUSSION OF CURRENT ACTIVITIES

Improved Iron Aluminide Coatings

We have now produced FeAl coatings as thick as 100 μm deposited on Type 316 stainless steel and on Alloy 800 with none of the cracking defects that were observed when aluminum electrodes were used.

Seven groups of test specimens incorporating FeAl in the coating were prepared for corrosion testing at ANL. Most are still in test, but results to date show that the already-attractive corrosion performance of the best previous Fe_3Al coatings is improved by about a factor of 3 when FeAl is applied directly to the Type 316 stainless steel substrates. Figure 1 shows comparison of the Fe_3Al, FeAl, and bare 316 SS weight changes in coal gasification atmospheres at 650°C.[2,10]

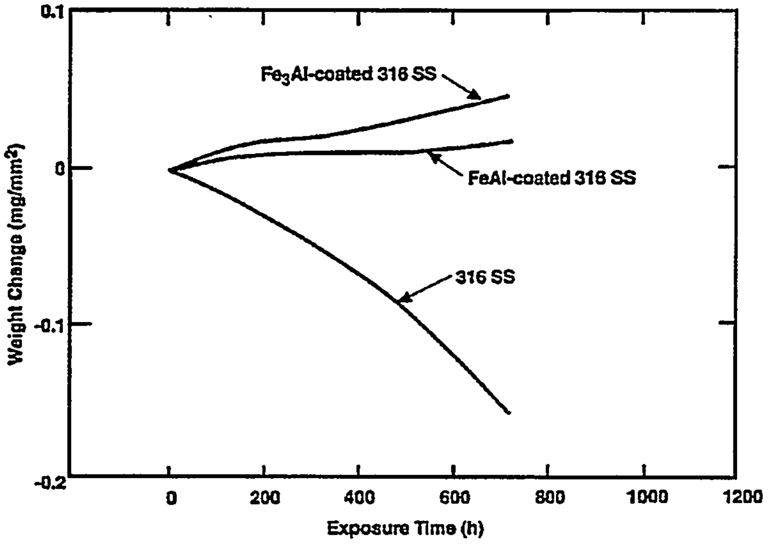

Figure 1.Corrosion of ESD Coatings in coal gasification atmospheres at 650°C.[2,10]

The remaining ESD coating candidates still in test at ANL consist of various combinations of Fe_3Al, FeAl, Nb, and Mo, applied to Type 316 stainless steel substrates. The Nb and Mo represent refractory metal diffusion barriers applied between the stainless steel substrate and the iron aluminde coating to inhibit the diffusion of nickel to the surface and the diffusion of sulfur or oxygen to the substrate, both of which are mechanisms of corrosion failure. The application of the diffusion barrier also reduces the weld dilution effects during the coating process and results in the surface composition of the coating more nearly approaching the composition of the electrodes used.

Test specimens of the advanced coatings were delivered to Argonne National Laboratory for corrosion testing in fossil energy environments. The success of using FeAl as a coating material now opens the potential for further improving the performance of Fe_3Al alloys. The Fe_3Al alloys so far can provide better mechanical properties in structural applications than FeAl, while an FeAl coating could improve the corrosion performance in applications where the higher aluminum content is desirable. It is possible such treatments could also improve the resistance of Fe_3Al to hydrogen embrittlement (described by McKamey and Liu[11]). Plate or sheet substrates of Fe_3Al have been requested from ORNL for further exploration of these potential improvements.

Technology Transfer Activities

A major manufacturer of heavy equipment (rail cars, ships, etc.) performed field evaluations of ESD hardsurfaced weld-wire feed-rollers, and reported a minimum of 5X increase in service life. Use of ESD is now saving over $100,000 per year for this application alone. Other applications are now being evaluated.

Consultations and test specimens of Electro-Spark Deposited (ESD) coatings were provided to Westinghouse Steam Turbine Division in Orlando, FL. Corrosion tests to date in wet steam containing NaCL and NaOH on coated U-bend specimens show that our recommended ESD coatings of Hastelloy C-22^{TM} provides outstanding prevention of chloride and caustic stress corrosion cracking. The next phase of longer term (1 yr) materials tests are in progress to qualify the ESD coatings for large steam turbine applications. No other coating process has been found that is capable of economically providing the required surface treatment to some of the difficult geometries involved.

A presentation was given to Air Force Air Logistics Center personnel at Randolf AFB on the potential uses of Electro-Spark Deposited coatings to replace chromium plating as a hard surfacing on aircraft components. The Air Force is phasing out chromium plating in many applications and is searching for more environmentally benign coating technologies. Until now, the best candidate replacements have been various forms of thermal spray coatings, but these are proving to be inadequate in several applications, due to delamination failures. (ESD coatings in similar conditions are virtually immune to such failures.) Further discussions with the Air Force are in progress.

Visits and consultations on the Electro-Spark Deposition process were provided to a major manufacturer of gas turbine engines. The manufacturer is now successfully using the ESD process for several applications, including modification of aluminide diffusion coatings, recovery of out-of-tolerance parts, and hard surfacing of critical turbine blade wear locations. This the second, but largest, successful application of the ESD technology in the gas turbine field so far.

A new commercial application for Electro-Spark Deposited coatings is resulting from consultation and work provided to a small Seattle-based fabricator as part of our technology transfer activities. ESD coatings of titanium carbide provided a required increase in gripping force in special collets where all other coatings and materials failed. There now appears to be a significant market for these and similar collets.

Other technology transfer activities included:

- Consultations were provided to a diffusion coating manufacturer on possible uses of ESD-applied FeAL to protect welds on previously aluminized components. (Follow-on tests are in progress.)
- Control rod drive rollers were coated for tests at Bettis Atomic Power Laboratory.

REFERENCES

1. R. N. Johnson, "Principles and Applications of Electro-Spark Deposition," Surface Modification Technologies, T.S. Sudarshan and D.G. Bhat, eds., The Metallurgical Society, January 1988, pp. 189-213.

2. R. N. Johnson, "Electro-Spark Deposited Coatings for High Temperature Wear and Corrosion Applications." presented at Symposium on High Temperature Coatings I (HTC-I '94), TMS, Rosemount, IL, October 1994 (to be published in the Proceedings).

3. R. N. Johnson, "Coatings for Fast Breeder Reactors," in Metallurgical Coatings, Elsevier Sequoia, S.A. , New York, 1984, pp. 31-47.

4. K. Natesan and R. N. Johnson, "Corrosion Resistance of Chromium Carbide Coatings in Oxygen-Sulfur Environments," Surface and Coatings Technology, Vol. 33, 1987, pp. 341-351.

5. I. G. Wright and J. A. Colwell, "A Review of the Effects of Micro-Alloying Constituents on the Formation and Breakdown of Protective Oxide Scales on High Temperature Alloys at Temperatures Below 700°C," ORNL/Sub/86-57444/01, September 1989.

6. K. Natesan and R. N. Johnson, "Development of Coatings with Improved Corrosion Resistance in Sulfur-Containing Environments," presented at the International Conference on

Metallurgical Coatings, San Diego, April 1990, published in Surface and Coatings Technology, Vol. 3/44, 1990, pp. 821-835.

7. R. N. Johnson, "Electro-Spark Deposited Coatings for Protection of Materials in Sulfidizing Environments," Proceedings of the Fourth Annual Conference on Fossil Energy Materials, ORNL/FMP-90/1, August 1990, pp. 321-329.

8. R. N. Johnson, "Electro-Spark Deposited Coatings for Protection of Materials in Sulfidizing Atmospheres," Proceedings of the Fifth Annual Conference on Fossil Energy Materials, ORNL/FMP-91/1, September 1991, pp. 281-288.

9. R. N. Johnson, "Electro-Spark Deposited Coatings for Fossil Energy Environments," in Proceedings of the Seventh Annual Conference on Fossil Energy Materials, ORNL/FMP-93/1, July 1993, pp. 289-295.

10. K. Natesan and W. D. Cho, "High Temperature Corrosion of Iron Aluminides," in Proceedings of the Eighth Annual Conference on Fossil Energy Materials, ORNL/FMP-94/1, May 1994.

11. C. G. McKamey and C. T. Liu, "Environmental Embrittlement of Iron Aluminides in Moisture-Containing Atmospheres," in Proceedings of the Environmental Effects on Advanced Materials, NACE Conference, June 1991.